

TUNING THE STRUCTURE AND FUNCTIONALITY OF METAL-ORGANIC
FRAMEWORKS VIA LINKER DESIGN

A Dissertation

by

YINGMU ZHANG

Submitted to the Office of Graduate and Professional Studies of
Texas A&M University
in partial fulfillment of the requirements for the degree of

DOCTOR OF PHILOSOPHY

Chair of Committee,	Hong-Cai Zhou
Committee Members,	Marcetta Y. Darensbourg
	Christian B. Hilty
	Hong Liang
Head of Department,	Simon W. North

August 2019

Major Subject: Chemistry

Copyright 2019 Yingmu Zhang

ABSTRACT

Metal-organic frameworks (MOFs) are a fascinating class of porous materials that have shown great promise in numerous applications. As one of the building components, organic linkers play an important role in dictating MOF synthesis. The geometry and connectivity of a linker determine the MOF structure, while linkers with desired functional groups lead to the application-orientated MOFs. In this dissertation, we will focus on MOF synthesis via linker design, discussing building MOFs with unique properties for targeted applications, especially for heterogeneous catalysis and chemo-sensing.

MOFs prove to be an ideal platform to bear catalytic-active sites for heterogeneous catalysis. These active sites can be directly functionalized onto the organic linkers. In one of my projects, through topology-guided synthesis, a terpyridine-containing mesoporous MOF was successfully constructed, adopting a β -cristobalite-type structure. The MOF incorporates well-arranged terpyridine coordination sites for facile post-synthetic metalation, which can be effectively applied as a general scaffold for the preparation of noble-metal-free catalysts.

MOFs have also been enacted in solar-energy conversion for photochemical synthesis by means of converting molecular oxygen to reactive oxygen species (ROS). However, visible-light responsive MOFs for oxygen activation remains scarce. To achieve this goal, we synthesized two visible-light responsive MOFs, namely, PCN-822(M) (M= Zr, Hf), which are constructed from a 4,5,9,10-(k-region) substituted pyrene-based ligand. With a broad-band adsorption from 225 nm to 650 nm, these MOFs can be applied as efficient ROS generators under visible-light excitation, while the hafnium-based MOF, PCN-822(Hf), can promote the oxidation of amines to imines by synergistic photoinduced energy and charge transfer to active molecular oxygen.

Functionalization with π -conjugated fluorescent moieties on the linkers, MOFs can serve as efficient luminescent sensors for molecular recognition. A new luminescent mesoporous MOF, PCN-604, was synthesized from a pyridyl-based linker. Due to the extra open metal site on the pyridyl group, PCN-604 shows a fast fluorescence-quenching response towards trace amounts of Fe^{3+} ions. Moreover, this material has exceptional stability in water, enabling performance in aqueous systems.

The photoluminescent properties of an organic linker can also be tuned by the MOF structure. A novel metal-organic framework, PCN-811, was constructed by an AIEE-featured triphenylene-based hexatopic linker. The rigidifying effect of the framework enhances the absolute quantum yield of the linker 4-fold in comparison with that of free-state linker. Moreover, with its electron-rich triphenylene core, PCN-811 exhibits an record-high sensing capability towards electron-deficient 2,4,6-trinitrophenol (TNP) in aqueous media.

DEDICATION

To my beloved family and relatives for their continual support

To all my friends who helped me during my study in the U.S.

ACKNOWLEDGEMENTS

I would first like to express my appreciation to my research advisor, Dr. Hong-Cai Zhou for his guidance, patience and encouragement throughout the past five years. I would also like to thank my committee members, Dr. Marcetta Darensbourg, Dr. Christian Hilty, Dr. Hong (Helen) Liang, as well as my ex-committee member, Dr. Kim Dunbar, for providing valuable suggestions and supports in my research. Thanks also go to our department members, especially Ms. Sandy Horton, Ms. Lizzie West and Ms. Carrie Frederiksen for offering generous help during my time at Texas A&M University.

I would like to acknowledge the Zhou group members from the past and present. Special thanks to my mentor Dr. Qiang Zhang, who trained me and imparted his knowledge of metal-organic framework to me without reservation. I am also grateful to Dr. Jun-sheng Qin, Dr. Jiandong Pang, Dr. Shuai Yuan, Dr. Bao Li, Dr. Peng Zhang, Dr. Yu Fang and Dr. Chengfeng Zhu for their professional suggestions and insightful discussions. My thanks are also extended to Dr. Mingbao Feng, Dr. Xuan Wang, Mr. Xinyu Yang, Mr. Jialuo Li, Mr. Kirchon Angelo, Mr. Greg Day for their valuable collaboration and help in my research.

My friends also deserve acknowledgement, especially my best friends, Dr. Qiulin Wu and Ms. Di Sun, and my four-year roommate, Ms. Zhuotong Liu, for their precious friendship and companionship during my graduate period.

Finally, I want to express my greatest gratitude to my parents and my fiancé for their encouragement, support and endless love.

CONTRIBUTORS AND FUNDING SOURCES

Contributors

This work was supervised by a dissertation committee consisting of Professor Hong-Cai Zhou [advisor], Professor Dr. Marcetta Y. Darensbourg, Professor Christian B. Hilty of the Department of Chemistry [Home Department] and Professor Dr. Hong Liang of the Department of Mechanical Engineering [Outside Department].

The Electron Paramagnetic Resonance (EPR) measurement in Chapter III was conducted in part by Mingbao Feng of Department of Environmental and Occupational Health, School of Public Health, Texas A&M University.

The Cyclic Voltammetry (CV) tests in Chapter III was conducted by Haomiao Xie of Department of Chemistry, Texas A&M University.

All other work conducted for the dissertation was completed by the student independently.

Funding Sources

This work was supported by Center for Gas Separations Relevant to Clean Energy Technologies, an Energy Frontier Research Center (EFRC) funded by U.S. Department of Energy (DOE), Office of Science, Office of Basic Energy Sciences under award no. DE-SC0001015, by a Robert A. Welch Chair in Chemistry under award no. A-0030, by U.S. Department of Energy, Office of Fossil Energy, National Energy Technology Laboratory under award no. DE-FE0026472, by the NPRP award NPRP9-377-1-080 from the Qatar National Research Fund.

Its contents are solely the responsibility of the authors and do not necessarily represent the official views of the funding offices.

NOMENCLATURE

BET	Brunauer-Emmett-Teller
CCDC	Cambridge Crystallographic Data Center
COF	Covalent Organic Framework
DEF	<i>N,N</i> -Diethyl Formamide
DFT	Density Functional Theory
DMF	<i>N,N</i> -Dimethyl Formamide
EPR	Electron Paramagnetic Resonance
FRET	Fluorescence Resonance Energy Transfer
KTDA	kinetically Tuned Dimensional Augmentation
MOFs	Metal-organic Frameworks
NMR	Nuclear Magnetic Resonance
PCN	Porous Coordination Network
PET	Photoinduced Electron Transfer
PSM	Post-synthetic Metalation
PXRD	Powder X-Ray Diffraction
SBU	Secondary Building Units
TGA	Thermogravimetric analysis
XRD	X-Ray Diffraction

TABLE OF CONTENTS

	Page
ABSTRACT	ii
DEDICATION.....	iv
ACKNOWLEDGEMENTS	v
CONTRIBUTORS AND FUNDING SOURCES	vi
NOMENCLATURE	vii
TABLE OF CONTENTS.....	viii
LIST OF FIGURES	xi
LIST OF TABLES.....	xviii
CHAPTER I INTRODUCTION TO METAL-ORGANIC FRAMEWORKS FOR HETEROGEOUS CATALYSIS AND CHEMO-SENSING	1
1.1 Introduction to Metal-Organic Frameworks (MOFs)	1
1.1.1 Development of MOFs	2
1.1.2 Rational Design of MOF.....	5
1.2 MOF-Based Heterogeneous Catalyst.....	16
1.2.1 Introduction of MOF-Based Catalysts.....	16
1.2.2 Transition-Metal Complexes on Linkers	17
1.2.3 Summary	27
1.3 MOF-Based Luminescent Sensors.....	28
1.3.1 Origins of Luminescence in MOF-Based Sensors	29
1.3.2 Detecting Mechanism of MOF-Based Sensors	30
1.3.3 Virtues of MOFs as Sensors.....	31
1.3.4 Chemical Sensing	32
1.3.5 Summary	35
CHAPTER II A NNN-PINCER-BASED MOF SCAFFOLD FOR PREPARATION OF NOBLE-METAL-FREE CATALYST	37
2.1 Introduction.....	37
2.2 Experimental Section	39
2.2.1 Materials and Instrumentation.....	39
2.2.2 Ligand Synthesis	40

2.2.3 Synthesis of PCN-308.....	43
2.2.4 Activation of PCN-308	43
2.2.5 Post-Synthetic Metalation (PSM) of PCN-308.....	44
2.2.6. Investigation of Catalytic Performance	44
2.3 Results and Discussion.....	47
2.3.1 Topology Design and Structural Description of PCN-308.....	47
2.3.2 Porosity of PCN-308	49
2.3.3 Chemical and Thermal Stability Analysis of PCN-308.....	49
2.3.4 Post-synthetic Metalation of PCN-308.....	53
2.3.5 Catalytic Performance of Metalated PCN-308	60
2.4 Conclusion.....	69
CHAPTER III PYRENE-BASED MOFS AS VISIBLE-LIGHT HARVESTING ROS GENERATORS.....	70
3.1 Introduction.....	70
3.2 Experimental Section	72
3.2.1 Materials and Instrumentation.....	72
3.2.2 Ligand Synthesis	73
3.2.3 Synthesis of PCN-822.....	77
3.2.4 Single Crystal X-ray Crystallography	77
3.2.5 Procedure of photooxidation of 1,5-Dihydroxynaphthalene (DHN).....	78
3.2.6 Procedure for Oxidation of Various Amines	78
3.2.7 Electronic Properties.....	78
3.3 Results and Discussion.....	79
3.3.1 Ligand Design and Structural Description of PCN-822	79
3.3.2 Chemical and Thermal Stability.....	84
3.3.3 Photophysical Properties.....	87
3.3.4 Photooxidation of 1,5-Dihydroxynaphthalene (DHN)	89
3.3.5 Oxidation of Various Amines	93
3.3.6 Mechanisms.....	99
3.4 Conclusion.....	103
CHAPTER IV DIRECT SYNTHESIS OF FUNCTIONALIZED PCN-333 VIA LINKER DESIGN.....	104
4.1 Introduction.....	104
4.2 Experimental Section	106
4.2.1 Materials and Instrumentation.....	106
4.2.2 Ligand Synthesis	107
4.2.3 Synthesis of PCN-604.....	109
4.2.4 Activation of PCN-604	109
4.2.5 Fluorescence Quenching and Titration Experiments.....	110
4.3 Results and Discussion.....	110
4.3.1 Topology Design and Structural Description of PCN-604.....	110
4.3.2 Porosity Characterization of PCN-604	112

4.3.3 Stability Characterization.....	113
4.3.4 Luminescence Properties	116
4.3.5 Sensing Measurements	118
4.3.6 Sensing Mechanism.....	122
4.4 Conclusion.....	126
CHAPTER V AGGREGATION TO THE BEST: A 9-CONNECTED ZIRCONIUM MOF WITH TRIPHENYLENE-BASED HEXATOPIC LINKER.....	127
5.1 Introduction.....	127
5.2 Experimental Section	129
5.2.1 Materials and Instrumentation.....	129
5.2.2 Synthesis of Linker.....	130
5.2.3 Synthesis of PCN-811.....	132
5.2.4 Rotation Electron Diffraction (RED) and PXRD refinement	133
5.2.5 N ₂ Sorption Isotherm	134
5.3 Results and Discussion.....	134
5.3.1 Structural Description of PCN-811	134
5.3.2 Chemical and Thermal Stability Analysis of PCN-811	135
5.3.3 Photophysical Properties of PCN-811	138
5.3.4 Detection of Selected Explosives	140
5.3.5 Mechanism	144
5.4 Conclusion.....	145
CHAPTER VI CONCLUSIONS.....	147
REFERENCES	150

LIST OF FIGURES

	Page
Figure I-1. The graphic illustration of (a) MOF-5 and (b) HKUST-1. C, gray; O, red; and N, blue. The yellow ball represents the porosities. Reprinted with permission from Ref. 20. Copyright © 2016 Elsevier Inc.	2
Figure I-2. (a) The computationally designed trimeric building block chelated by three carboxylic functions. (b) BDC ligand, which lies one the edges of (c) STH. (d) Ball-and-stick representation of unit cell of the structure. (e) Schematic 3D representation of the MTN zeotype architecture (the vertices represent the centers of each STH) with the medium (in green, with 20 tetrahedra) and large (in red with 28 tetrahedra) cages delimited by the vertex sharing of the STH. Chromium octahedra, oxygen, fluorine and carbon atoms are in green, red, and blue, respectively. Reprinted with permission from Ref. 7. Copyright @ 2005, American Association for the Advancement of Science.	3
Figure I-3. (a) One unit cell of copper drawn to scale with: (b) Zr-MOF with BDC as linker, UiO-66, (c) Zr-MOF with 4,4' - biphenyl-dicarboxylate (BPDC) as linker, UiO-67, (d) Zr-MOF with terphenyl dicarboxylate (TPDC) as linker, UiO-68. Zirconium, oxygen, carbon, and hydrogen atoms are red, blue, gray, and white, respectively. Reprinted with permission from Ref. 8. Copyright © 2008, American Chemical Society.	4
Figure I-4. Structure illustrations of PCN-332 and PCN-333. (a) Ligands used in PCN-332 and PCN-333. (b) Three different cages in PCN-332 and PCN- 333. (c) Simplification of PCN-332 and PCN-333 into MTN topology. Reprinted with permission from Ref. 25. Copyright © 2015, Springer Nature.	6
Figure I-5. (a) Structure of PCN-333 with three different cages. (b) Structure of PCN-262, a direct synthesis product from OH-BTB. Reprinted with permission from Ref. 27. Copyright © 2015, American Chemical Society.	7
Figure I-6. (a) Topology prediction framework for designing tetratopic ligand-based Zr MOF. (b) The graphic representations of selective topologies. Reprinted with permission from Ref. 28. Copyright © 2016, American Chemical Society.	9
Figure I-7. Some representative ditopic carboxylate linkers and illustration of formation of extended IRMOF networks by replacing acetate with rigid dicarboxylates. Zn (turquoise polyhedra); O (red); C (black). Reprinted with permission from Ref. 34. Copyright 2014 © Royal Society of Chemistry.	10
Figure I-8. Chemical structures of organic linkers used in the synthesis of IRMOF-74s. Perspective views of a single one-dimensional channel with 98 Å pore aperture	

shown for IRMOF-74-XI. Mg (turquoise), O (red), C (black). Reprinted with permission from Ref. 35. Copyright 2014 © Royal Society of Chemistry.....	11
Figure I-9. Graphic synthetic scheme of PCN-228, 229 and 230. Reprinted with permission from Ref. 36. Copyright © 2014, American Chemical Society.	12
Figure I-10. Synthesis of MOF-1001, a non-interpenetrating cubic structure isoreticular to MOF-5; crown ethers are placed throughout the whole framework. Color scheme: Zn (turquoise polyhedra); O (red); C (black); macrocyclic polyethers (red). Reprinted with permission from Ref. 38. Copyright 2014 © Royal Society of Chemistry.	14
Figure I-11. Schematic illustration of grafting various functional groups onto the pore walls of the MOF via the click reaction between azide and alkyne groups. Reprinted with permission from Ref. 39. Copyright © 2012, American Chemical Society.....	15
Figure I-12. Synthesis of UiO-66-PdTCAT. Reprinted with permission from Ref. 41. Copyright © 2015, American Chemical Society.....	16
Figure I-13. (a) (b) Assembly of D _{3d} and D _{4h} nodes into (4,6)-connected she topological network. (c) Chemical structures of Et-TCPP(Fe), Br-TCPP(Fe), Cl-TCPP(Fe), and F-TCPP(Fe) linkers. Reprinted with permission from Ref.56. Copyright 2017 @ American Chemical Society.....	18
Figure I-14. Synthesis of Doped UiO-67. Reprinted with permission from Ref. 60. Copyright 2011@ American Chemical Society.....	19
Figure I-15. (a) Synthesis of the pincer ligand. (b) Framework structure. Linker disorder has been omitted for clarity. (c) View of a portion of the framework showing ovoidal pores. Blue octahedra represent [Zr ₆ O ₄ (OH) ₄] ¹²⁺ building units. Reprinted with permission from Ref. 65. Copyright 2016 @ American Chemical Society.....	21
Figure I-16. (a) Preparation of the Cationic Center in PCN-223(Fe); (b) hDA Reaction Catalyzed by PCN-223(Fe). Reprinted with permission from Ref. 69. Copyright © 2014, American Chemical Society.	22
Figure I-17. (a) Schematic structures of the MOF-CoCl ₂ precatalysts. (b, c) Idealized structures of bpyv-MOF-CoCl ₂ and mBPP-MOFCoCl ₂ . Reprinted with permission from Ref. 74. Copyright © 2016, American Chemical Society.	23
Figure I-18. (a) Structural model showing the octahedral cage of NacNac-functionalized MOF. (b) PXRD patterns of various ion-metalated MOF samples. (c) Synthesis sequence showing NacNac installation and metalation. Reprinted with permission from Ref. 83. Copyright @ 2016, American Chemical Society.....	25
Figure I-19. Post-synthetic metalation of BINAP-MOF (1) to form 1·Ru and 1·Rh. Reprinted with permission from Ref. 85. Copyright @ 2014, American Chemical Society.....	27

Figure I-20. Representation of possible emission modes in MOFs. Inorganic SBUs, blue spheres; Organic linkers, red cylinders; Guest chromophores, yellow sphere inside. Reprinted with permission from Ref.15. Copyright © 2017, Elsevier B.V.....	30
Figure I-21. The schematic illustration for the fabrication and metal ions luminescent sensing of the two-dimensional MOF nanosheets materials. Reprinted with permission from Ref. 115. Copyright 2016 © Royal Society of Chemistry.	33
Figure I-22. Schematic representation of the mechanism for the detection of energetic heterocyclic compounds by TABD-MOFs. Reprinted with permission from Ref. 119. Copyright @ 2014, American Chemical Society.....	35
Figure II-1. ¹ H NMR spectrum of 1-(5-methylpyridin-2-yl)ethan-1-one.	41
Figure II-2. ¹ H NMR spectrum of 4-(5,5"-dimethyl-[2,2':6',2"-terpyridin]-4'-yl)benzoic acid. ...	42
Figure II-3. ¹ H NMR spectrum of H ₃ TPY.	43
Figure II-4. a) Trigonal-planar organic linker TPY and six-connected D _{3d} -symmetric Zr ₆ antiprismatic cluster. b) β-cristobalite network of PCN-308 simulated based on the reported PCN-777 structure. The yellow sphere represents the void space.....	47
Figure II-5. SEM image of powder PCN-308.	48
Figure II-6. PXRD comparison between as-synthesized PCN-308(red) and previously reported PCN-777 (black).	49
Figure II-7. N ₂ sorption isotherm for PCN-308 at 77K, 1 atm.....	50
Figure II-8. DFT pore size distribution for PCN-308 derived by N ₂ isotherm measured at 77 K, 1 atm.	51
Figure II-9. PXRD patterns reported PCN-777 (red), pristine PCN-308 (black) and PCN-308 powder after water treatment for 24 hours.	52
Figure II-10. N ₂ isotherms of pristine PCN-308 and water-treated PCN-308 at 77 K, 1 atm.	52
Figure II-11. Thermogravimetric analysis data of as-synthesized PCN-308. The decomposition temperature is around 490 °C based on calculation.	53
Figure II-12. Color changes of PCN-308 after post-synthetic metalation.	53
Figure II-13. Representative SEM image of Fe@PCN-308 powder and corresponding EDS-mapping of Zr and Fe from left to right.	54
Figure II-14. SEM-EDS analysis of Fe@PCN-308.....	55

Figure II-15. XPS spectrum of Fe@PCN-308.....	56
Figure II-16. Representative SEM image of Co@PCN-308 powder and corresponding EDS-mapping of Zr and Co from left to right.	57
Figure II-17. SEM-EDS analysis of Co@PCN-308.	57
Figure II-18. XPS spectrum of Fe@PCN-308.....	58
Figure II-19. PXRD patterns of PCN-308 after post-metalation.....	59
Figure II-20. N ₂ isotherms of PCN-308 after post-metalation.	59
Figure II-21. PXRD patterns of recycled Fe@PCN-308 (1 st run, black; 2 nd run, pink; 3 rd run, blue; 4 th run, red; 5 th run, orange.	62
Figure II-22. Recycling catalytic performance of Fe@PCN-308 in epoxidation of styrene.	62
Figure II-23. PXRD patterns of recycled Fe@PCN-308 (1 st run, green; 2 nd run blue; 3 rd run, purple.	67
Figure II-24. Recycling catalytic performance of Co@PCN-308 in borylation of benzene.....	67
Figure III-1. ¹ H NMR spectrum of H ₄ BPETB.....	76
Figure III-2. Representative structure and topology of (a) the 8-connected Zr ₆ /Hf ₆ cluster and (b) the tetratopic H ₄ BPETB that construct (c) PCN-822.	79
Figure III-3. PXRD patterns of as-synthesized PCN-822(Zr) in red, PCN-822(Hf) in orange and the simulated pattern in black.	81
Figure III-4. UV-vis. spectra of methyl orange solutions with various concentrations.....	83
Figure III-5. Calibration curve obtained based on the UV-vis spectra.	83
Figure III-6. The change of UV-vis spectra of methyl orange solution before and after loading PCN-822(Zr/Hf).	84
Figure III-7. Thermogravimetric (TG) analysis data of as-synthesized PCN-822(Zr/Hf).....	85
Figure III-8. PXRD patterns of PCN-822(Zr) after water treatment in aqueous solutions.....	86
Figure III-9. PXRD patterns of PCN-822(Hf) after water treatment in aqueous solutions.	86
Figure III-10. Solid-state UV-vis adsorption spectra of ligand and PCN-822.....	87
Figure III-11. Emission spectra of ligand and PCN-822(Zr/Hf).	87

Figure III-12. The frontier molecular orbital distribution of free organic ligand (up) and in PCN-822.....	89
Figure III-13. Confocal scanning microscopic images of a) PCN-822(Zr) and b) PCN-822(Hf).....	89
Figure III-14. Changes of UV-vis spectra for photooxidation of DHN sensitized by PCN-822(Hf).....	91
Figure III-15. Changes of UV-vis spectra for photooxidation of DHN sensitized by PCN-822(Zr).	92
Figure III-16. Changes of UV-vis spectra for photooxidation of DHN with no sensitizer.....	92
Figure III-17. Comparison of PCN-822 and ligand in juglone development.....	93
Figure III-18. PXRD patterns of recycled PCN-822 (Hf) (1st run, pink; 2nd run, violet; 3rd run, blue).	95
Figure III-19. Recycling performance of PCN-822 (Hf) in oxidation of dibenzylamine.	96
Figure III-20. Proposed mechanisms of oxidation of amines.	99
Figure III-21. EPR spectra of TEMP- ¹ O ₂ obtained with or without light irradiation.	101
Figure III-22. EPR spectra of PCN-822(Hf) obtained in the dark and under visible light irradiation.....	101
Figure III-23. Cyclic Voltammetry tests of PCN-822(Hf).....	102
Figure III-24. Tauc plot of PCN-822(Hf). The optical band gap is calculated to be 2.17 eV. ...	102
Figure IV-1. ¹ H NMR spectrum of H ₃ PTB.....	109
Figure IV-2. PXRD Patterns of PCN-604 based on simulation (red) and experiment (black)...	112
Figure IV-3. N ₂ sorption isotherm of pristine PCN-604 at 77 K, atm. Insert shows the DFT pore size distribution.....	113
Figure IV-4. PXRD patterns of simulation PCN-604 (red), pristine PCN-604 (black), samples treated with water, pH = 8 aqueous solution (purple) and pH = 3 aqueous solution (green).....	114
Figure IV-5. N ₂ uptake isotherms of PCN-604 samples after treatment of aqueous solutions with different pH values.....	115
Figure IV-6. Thermogravimetric analysis of as-synthesized PCN-604.....	115

Figure IV-7. Solid-state excitation spectrum (blue dot) and emission spectrum (blue line) of PCN-604 at room temperature.....	117
Figure IV-8. Solid-state excitation spectrum (yellow dot) and emission spectrum (yellow line) of H3PTB at room temperature.	117
Figure IV-9. Emission spectra of PCN-604 suspensions dispersed in various solvents excited at 350 nm.....	118
Figure IV-10. Fluorescence quenching of PCN-604 dispersed in aqueous solutions of fifteen different metal cations (1 mM). Excitation at 350 nm, room.....	120
Figure IV-11. Fluorescent spectra of original PCN-604 suspension solution, upon addition of 1 mL of 14 metal ions (1 mM for each) and sequent addition of Fe ³⁺ (1mM).....	121
Figure IV-12. Fluorescence spectra of PCN-604 suspension in response to different concentrations of Fe ³⁺ . Fe ³⁺ aqueous solution (1 mM) was added gradually from 20 μL to 1000 μL (20 μL each time).....	121
Figure IV-13. SV plot of PCN-604.....	122
Figure IV-14. Emission spectrum of PCN-604 aqueous suspension (red) and adsorption spectra of different metal ions solutions in the concentration of 1mM.	124
Figure V-1. ¹ H NMR spectrum of H ₆ TPHB.....	132
Figure V-2. 2D slices cut from the reconstructed 3D reciprocal lattice of PCN-811 show the (a) hk0, (b) h0l, and (c) 0kl plane. (d) Reconstructed 3D reciprocal lattice of PCN-811. Insert is the crystal from which the RED data was collected.	133
Figure V-3. Powley fit of powder X-ray diffraction for PCN-811 using space group P4 ₁ 32. The curves are simulated (red), observed (blue), and difference profiles (gray), respectively; the bars below curves indicate peak positions.	133
Figure V-4. N ₂ sorption isotherm for PCN-811 at 77K, 1 atm.	135
Figure V-5. DFT pore size distribution for PCN-811 derived by N ₂ isotherm measured at 77 K, 1 atm.....	136
Figure V-6. PXRD patterns of PCN-822 after treatment of aqueous solutions with different pH values.....	136
Figure V-7. N ₂ isotherms after treatment of aqueous solutions.	137
Figure V-8. Thermogravimetric analysis of activated PCN-811. 5.4 % weight loss at the beginning is due to the water molecules on the Zr ₆ . The decomposition temperature is around 490 °C based on calculation.....	137

Figure V-9. Photoluminescence spectra of H ₆ TPHB in the mixture of THF/water solutions with different ratio.	139
Figure V-10. Solid-state photoluminescence spectra of PCN-811 (blue) and H ₆ TPHB (yellow) upon excitation at 370 nm at room temperature.	140
Figure V-11. Luminescence quenching spectra of PCN-811 suspension towards TNP. Insert shows Stern-Volmer plots towards TNP.	142
Figure V-12. Luminescence quenching spectra of PCN-811 suspension towards 2,4-DNP.	142
Figure V-13. Luminescence quenching spectra of PCN-811 suspension towards 4-NP.	143
Figure V-14. Luminescence quenching spectra of PCN-811 towards NM.	143
Figure V-15. Comparison of Stern-Volmer plots.	144
Figure V-16. The overlap between the absorbance spectra of different explosives and the emission spectrum of PCN-811.	145

LIST OF TABLES

	Page
Table II-1. Borylation of Arenes catalyzed by the homogeneous Co-TPY and non-metalated PCN-308.....	46
Table II-2. Porosity comparison between PCN-777 and PCN-308.....	51
Table II-3. Atomic ratio of Fe@PCN-308	55
Table II-4. Atomic ratio of Co@PCN-308.....	57
Table II-5. Screening experiments of styrene epoxidation.	61
Table II-6. Summary of catalysis results of reported MOFs in epoxidation of styrene.	63
Table II-7. Epoxidation of selected olefins.	65
Table II-8. Borylation of neat arenes.	66
Table II-9. Summary of catalysis results of reported MOFs in borylation of neat arenes.....	68
Table III-1. Crystal data and structure refinements for PCN-822 (Zr).	82
Table III-2. Screening experiments of oxidation of dibenzylamine ^[a]	95
Table III-3. Comparison of aerobic dibenzylamine oxidation with selective catalysts.	97
Table III-4. Oxidation of various amines.....	98
Table IV-1. Porosity comparison between PCN-333 and PCN-604.	113
Table IV-2. Comparison of sensing performance of PCN-604 for Fe ³⁺ ion with other MOF-based materials.	125

CHAPTER I
INTRODUCTION TO METAL-ORGANIC FRAMEWORKS FOR HETEROGEOUS
CATALYSIS AND CHEMO-SENSING^{1,2}

1.1 Introduction to Metal-Organic Frameworks (MOFs)

Metal-organic frameworks (MOFs), also known as porous coordination networks (PCNs) or porous coordination polymers (PCPs), are a class of porous materials assembled from metal containing units (secondary building unites, SBUs) and organic linkers via coordination bonds.¹⁻² In MOF materials, inorganic units can be a variety of metal ions that provide a coordination environment in forms of mononuclear or multinuclear clusters; while organic linkers usually contain coordinating groups, namely, carboxylate, phosphonate, sulfonate or heterocyclic groups, which can further chelate with metal units to form the infinite one-, two-, or three-dimensional networks.³ With the hybrid inorganic-organic constructing components, MOFs integrate the superiorities of both organic and inorganic units into one single system, presenting significant and unique properties including high crystallinity, permanent porosity, large surface area, and infinite tunability. These intriguing features highlight the advantages of MOF materials over other classic porous materials such as activated carbon, silica gels, molecular sieve, zeolite and porous polymers, etc.

¹ Part of this chapter is reprinted with permission from “Synthesis of MOFs for heterogeneous catalysis via linker design” by Zhang, Y.; Yang, X.; Zhou, H.-C., *Polyhedron*, 2018, 154, 189-201. Copyright @ 2018 Elsevier Ltd.

² Part of this chapter is reprinted with permission from “Luminescent sensors based on metal-organic framework” by Zhang, Y.; Yuan, S.; Day, G.; Wang, X.; Yang, X.; Zhou, H.-C., *Coord. Chem. Rev.*, **2018**, 354, 28-45, copyright @ 2017 Elsevier B.V.

1.1.1 Development of MOFs

In 1999, two of the earliest MOFs, MOF-5 and HKUST-1 (HKUST=Hong Kong University of Science and Technology), were reported, which marks a prominent milestone in MOF history.⁴⁻⁵ The structure of the two archetypical MOFs was successfully characterized via single crystal studies and low-pressure gas sorption analysis, indicating their unprecedented high porosity and surface areas (Figure I-1).

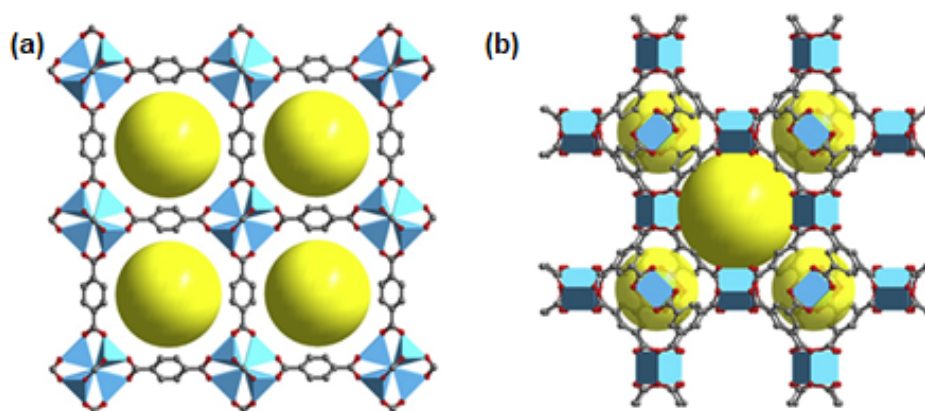


Figure I-1. The graphic illustration of (a) MOF-5 and (b) HKUST-1. C, gray; O, red; and N, blue. The yellow ball represents the porosities. Reprinted with permission from Ref. 20. Copyright © 2016 Elsevier Inc.

Since then, the MOF research has been burgeoning with an incredibly fast speed, especially in synthesizing ultra-porous MOFs. Generally, MOFs can be classified as microporous (diameter < 2 nm), mesoporous (diameter between 2-50 nm), and macroporous (diameter > 50 nm) based on the size of MOF cavity.⁶ In the early stage, most MOFs are microporous. In 2005, a mesoporous MOF, Cr-MIL-101 (MIL = Material Institute Lavoisier), was firstly reported, showing an exceptional porosity.⁷ The structure of Cr-MIL-101 can be simplified into a series of supertetrahedrons (STH) connected in a vertex-connecting manner, which are assembled from

trimeric-oxo $\text{Cr}_3(\mu_3\text{-O})$ clusters on the corner and 1,4-benzene-dicarboxylate (BDC) ligands on the face. Two types of mesoporous cavities are formed in the network with a diameter of 29 Å and 34 Å, respectively (Figure I-2). The MOF also presents record-high surface areas with an over 4100 m^2g^{-1} for Brunauer–Emmer–Teller (BET) surface area and 5900 m^2g^{-1} for Langmuir surface areas.

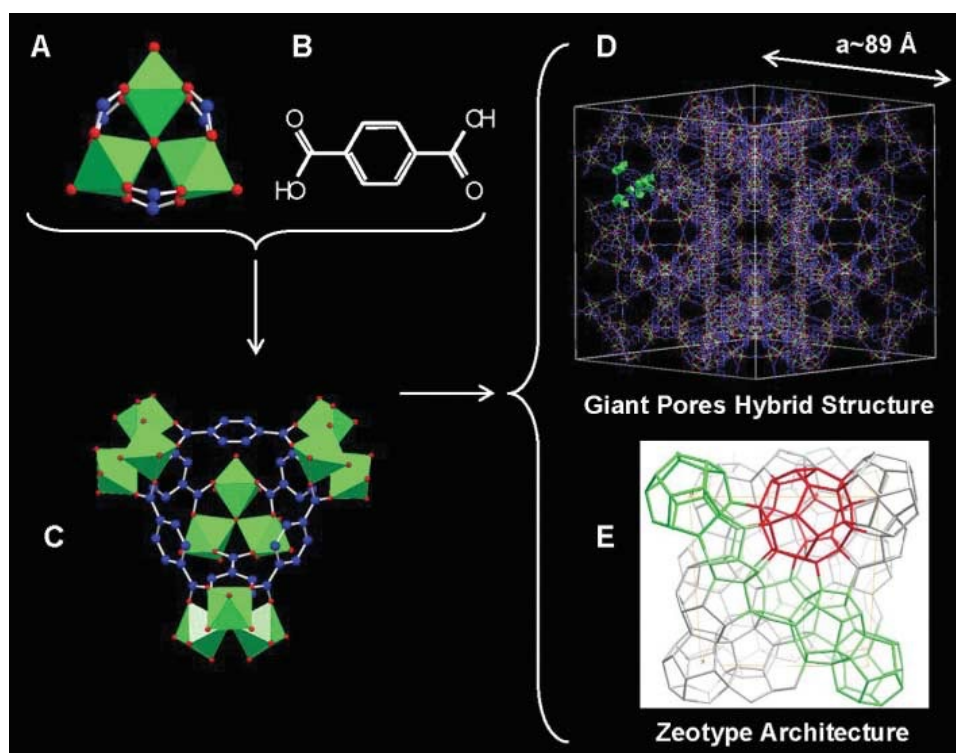


Figure I-2. (a) The computationally designed trimeric building block chelated by three carboxylic functions. (b) BDC ligand, which lies one the edges of (c) STH. (d) Ball-and-stick representation of unit cell of the structure. (e) Schematic 3D representation of the MTN zeotype architecture (the vertices represent the centers of each STH) with the medium (in green, with 20 tetrahedra) and large (in red with 28 tetrahedra) cages delimited by the vertex sharing of the STH. Chromium octahedra, oxygen, fluorine and carbon atoms are in green, red, and blue, respectively. Reprinted with permission from Ref. 7. Copyright @ 2005, American Association for the Advancement of Science.

Another researching field of MOF chemistry resides in the pursuit of stable MOF architectures. For a long time, divalent metals, such as Zn^{2+} or Cu^{2+} , were the most common-used inorganic building blocks for MOF synthesis. Given most organic ligands are functionalized with carboxylate groups, the metal-ligand bond is relatively labile, limiting the stability of MOFs under aqueous or other harsh conditions. In 2008, the appearance Zr^{4+} based MOF, UiO-66 (UiO = University of Oslo) pioneered the synthesis of stable MOFs.⁸ The MOF is built from 12-connected $Zr_6O_4(OH)_4$ metal cluster and BDC ligand. Consistent with Pearson's hard/soft acid/base (HSAB) principle, the strong coordination bond between the hard high-valent metal cluster and the hard carboxylate linker enables the MOF to remain integrate in water system.⁹ Moreover, the thermal stability reaches to 540 °C. By expanding the original one phenylene units to two or three, UiO-67 and UiO-68 could be yielded with increased surface areas and no sacrifice of chemical stability (Figure I-3).

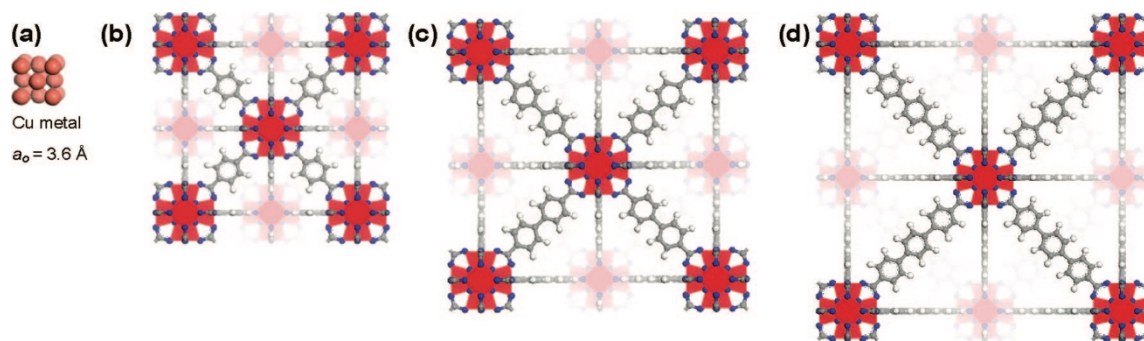


Figure I-3. (a) One unit cell of copper drawn to scale with: (b) Zr-MOF with BDC as linker, UiO-66, (c) Zr-MOF with 4,4' - biphenyl-dicarboxylate (BPDC) as linker, UiO-67, (d) Zr-MOF with terphenyl dicarboxylate (TPDC) as linker, UiO-68. Zirconium, oxygen, carbon, and hydrogen atoms are red, blue, gray, and white, respectively. Reprinted with permission from Ref. 8. Copyright © 2008, American Chemical Society.

So far, MOF chemistry has not been limited to building MOFs with unique structures, for example, flexible or multi-variant MOFs. Tremendous studies have also been focused on designing MOFs for certain applications. Numerous judiciously functionalized MOFs have been unitized in an ever-increasing scope of applications including gas storage and separation, heterogeneous catalysis, chemical sensing, biomedicine and proton conduction, etc.¹⁰⁻²⁰

1.1.2 Rational Design of MOF

One of the distinguished features of MOFs are their diversity and tunability in both structure and functionality. Theoretically, with various metal-containing units and organic linkers, inexhaustible number of MOFs could be designed and synthesized. It is ideal that one can rationalize the growth of MOFs with desirable structural or functional properties. However, the countless combination of molecular building blocks as well as synthesis conditions (temperature, solvent and substrate concentrations, etc.) deter the customization of targeted MOFs. The introduction of ‘reticular synthesis’ by Yaghi and coworkers paves the way for rational design of MOFs at molecular-level.²¹⁻²² It is proposed that on the premise of well-defined building blocks with rigid linking geometry, extended networks with predetermined structural topologies can be realized by strong bonding. In other words, the connectivity and orientation of inorganic clusters and organic linkers will dictate the assembly of a MOF matrix to a fixed topology or vice versa. According to ‘reticular synthesis’, three effective synthetic strategies including topology-guided design, isorecticular expansion and pre- / post-synthetic modification have been derived in pursuit of predictable design of MOF structures.²³ In this section, we will focus on the rational design of MOFs via ligand design based on the abovementioned three strategies. We will specify how the geometry, length, ratio and functional groups of organic linkers relate to the structure and

functionality of a MOF with given metal clusters. To narrow it down, in this chapter, MOFs composed of ditopic, tritopic or tetratopic carboxylate linkers will be mainly discussed to clarify the rational design of MOFs.

1.1.2.1 Topology-guided Design

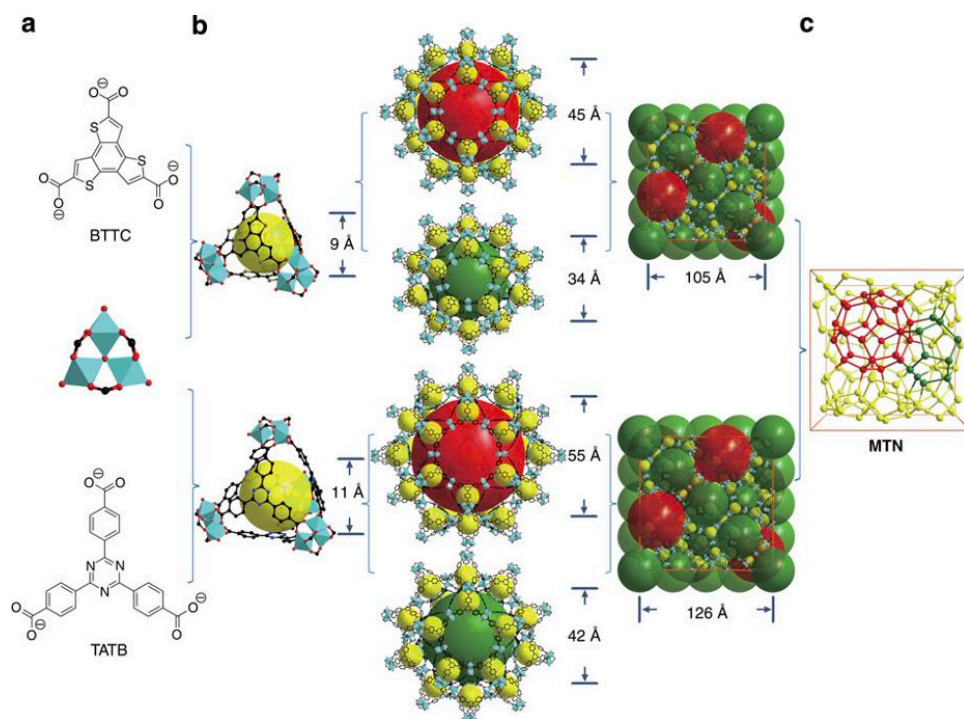


Figure I-4. Structure illustrations of PCN-332 and PCN-333. (a) Ligands used in PCN-332 and PCN-333. (b) Three different cages in PCN-332 and PCN-333. (c) Simplification of PCN-332 and PCN-333 into MTN topology. Reprinted with permission from Ref. 25. Copyright © 2015, Springer Nature.

Topology-guided design epitomizes the implementation of ‘reticular synthesis’ where a preconceived structure serves as a ‘template’ to guide the selection of molecular building blocks with desired connectivity and orientation.²⁴ Apparently, the judicious design of organic linkers is

a prerequisite for such MOF synthesis method. The geometry of linkers would determine the growth of MOFs to the targeted topology. One representative is the synthesis of mesoporous PCN-332 (PCN = Porous Coordination Network) and PCN-333 with MTN topology.²⁵ PCN-332 and PCN-333 are reticulated from previously reported MIL-100, which consists of trimetric metal clusters and tritopic linkers. In MIL-100, the organic linker, benzenetricarboxylate (BTC) has a free idealized D_{3h} symmetry as a free anion, while in the ligand symmetry is reduced to C_{3v} by a bowl-shaped bending to cover each face of the constructing supertetrahedron unit.²⁶ To meet the requirement of such topology, two ligands were selected, benzo-tris-thiophene carboxylate (BTTC) with a C_{3h} (pseudo- D_{3h} in crystallography) symmetry in PCN-322 and 4,4',4''-s-triazine-2,4,6-triyl-tribenzoate (TATB) with idealized D_{3h} symmetry in PCN-333. Finally, the targeted mesoporous MOFs were obtained with cavities large enough for enzyme encapsulation (Figure I-4).

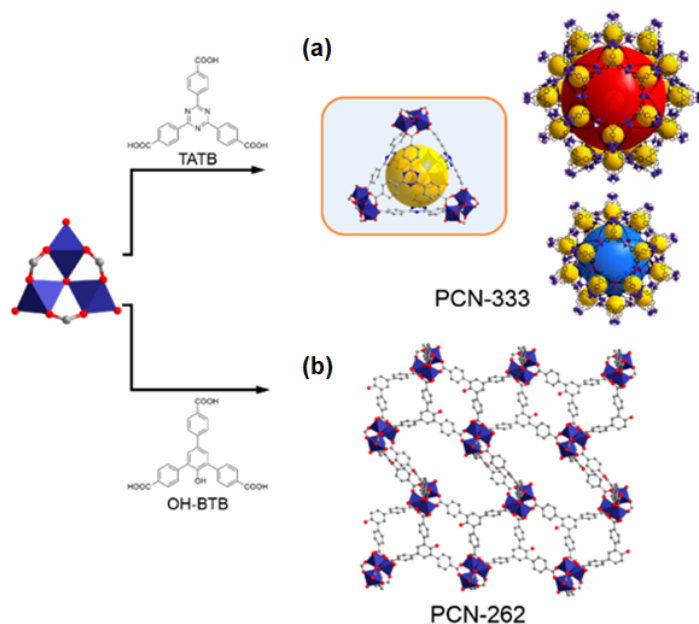


Figure I-5. (a) Structure of PCN-333 with three different cages. (b) Structure of PCN-262, a direct synthesis product from OH-BTB. Reprinted with permission from Ref. 27. Copyright © 2015, American Chemical Society.

On the other hand, failure to design ligand with D_{3h} symmetry tend to lead to MOFs with other structures, for example, PCN-260 with benzenetricarboxic acid (BTC) or PCN-262 with OH-BTB.²⁷ With the steric hindrance in the central benzene ring, the ligands have trouble in adopting the energy-unfavored coplanar D_{3h} symmetry in the solution, producing energy-dominated products even in the presence of the same inorganic building blocks (Figure I-5).

The synthesis of Zr-MOFs represents another typical example of topology-guided design, especially of the ones derived from tetratopic linkers and Zr_6 clusters. Tetratopic linkers can be categorized into tetrahedral, planar square or planar rectangular groups. It is proposed that with a fixed Zr_6 cluster, the topology of a MOF is highly dependent on the geometry of a tetratopic linker: A tetratopic linker adopting a tetrahedral shape tends to form a network with **flu** or **ith** topology, while a planar square linker will construct **ftw** MOF with 12-connected Zr_6 cluster. A tetratopic planar rectangular linker, on the other hand, will lead to the MOFs with **csq**, **sqc** and **scu** topologies (Figure I-6).²⁸⁻²⁹ It has been proved that many reported Zr-MOFs fall into the systematic topology prediction. In one case, a tetratopic porphyrin-based linker, tetrakis(4-carboxyphenyl)porphyrin (TCPP), has given rise to both **ftw** MOF, PCN-224 and **csq** MOF, PCN-222, as the linker can access both planar square and planar rectangular form via low-energy demanded linker distortion.³⁰⁻³¹ In another case, a perylene-based tetratopic linker only led to **csq** MOF, UCMC-313, because the linker only accesses a planar rectangular form.²⁸ Overall, the linker geometry has been applied as an essential selection criterion for the synthesis of Zr-MOFs in a controllable manner.

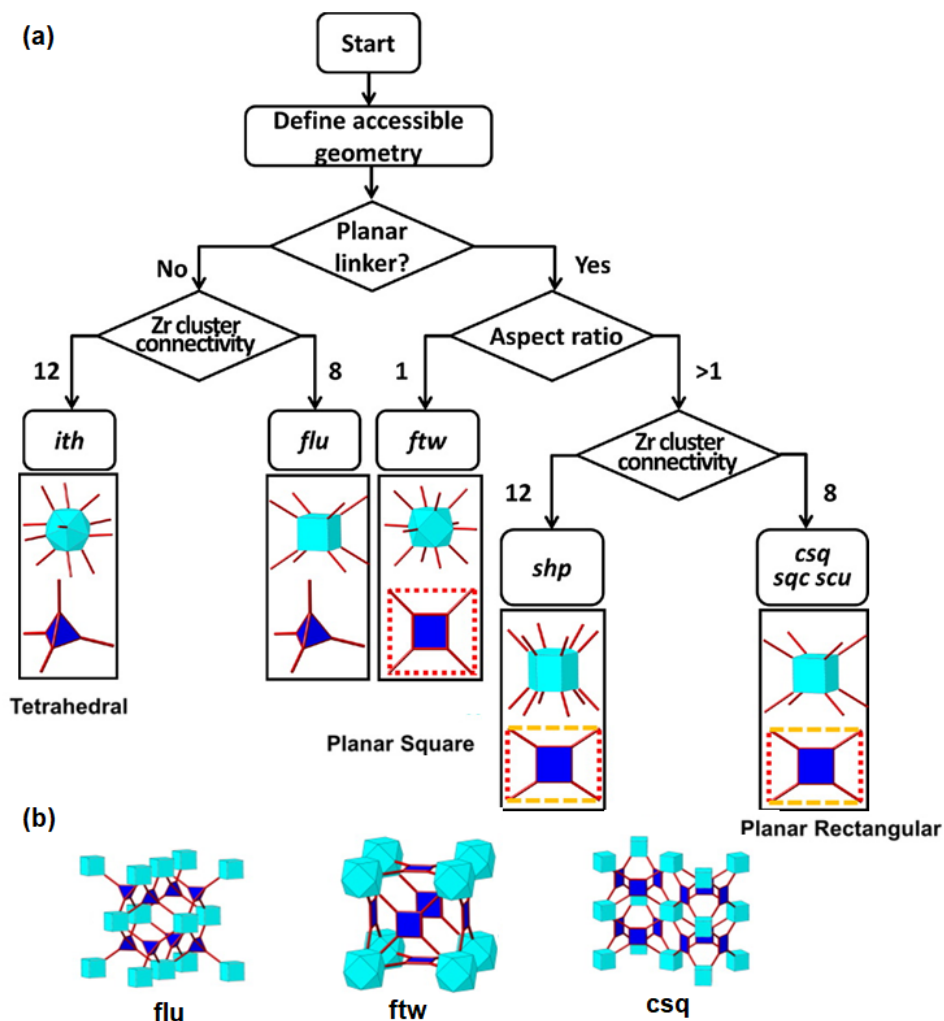


Figure I-6. (a) Topology prediction framework for designing tetratopic ligand-based Zr MOF. (b) The graphic representations of selective topologies. Reprinted with permission from Ref. 28. Copyright © 2016, American Chemical Society.

1.1.2.2 Isorecticular Expansion

Isorecticular expansion is another representative for rational design of MOFs derived from ‘reticular synthesis’. The particular method emphasizes on propagating the structure of a prototypical ‘parent MOF’ without changing the underlying topology by linker elongation. The extended networks usually present larger pore size, higher surface areas and/or tuned pore environment than the original ones.

One of the important examples are IRMOF-n series which are isorecticular to MOF-5.³²⁻³³ MOF-5 (IRMOF-1) is prepared from octahedral $Zn_4O(CO_2)_6$ clusters and H_2BDC . By replacing H_2BDC with other ditopic carboxylate linkers, isorecticular IRMOF-n could be obtained with pore size expanded from 3.8 to 28.8 Å (Figure I-7).³⁴

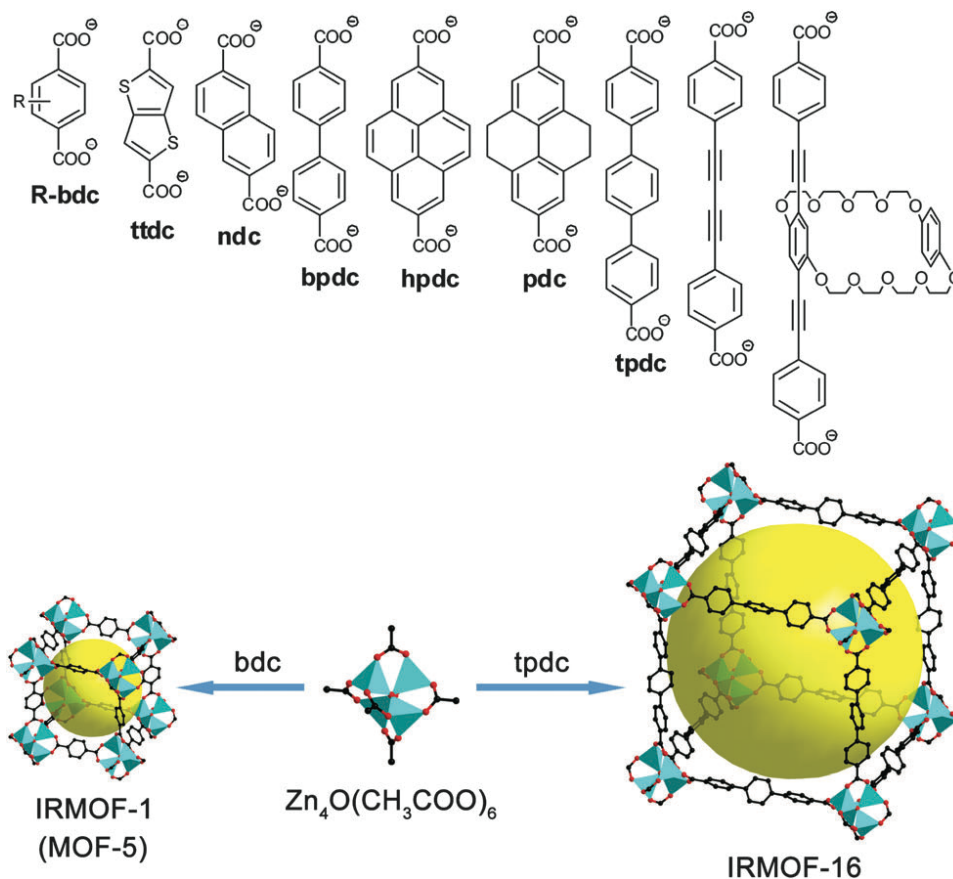


Figure I-7. Some representative ditopic carboxylate linkers and illustration of formation of extended IRMOF networks by replacing acetate with rigid dicarboxylates. Zn (turquoise polyhedra); O (red); C (black). Reprinted with permission from Ref. 34. Copyright 2014 © Royal Society of Chemistry.

Another famous example is isorecticular Mg-MOF-74 series, termed as IRMOF-74-I to IRMOF-74-XI.³⁵ MOF-74 is made from tetraanionic 2,5-dioxido-1,4-benzene-dicarboxylate

(dobdc/dhbdc/dot) and infinite inorganic rod-type SBUs where both the aryloxide and carboxylate are bonded to the metal sites to produce **bnn** parallel rod packing and one-dimensional (1-D) channels. Based on dobdc, a stepwise expansion was performed to increase the number of phenylene unit on the linker strut up to 11 units, affording MOF-74 series with the pore apertures ranging from 14 to 98 Å (Figure I-8).

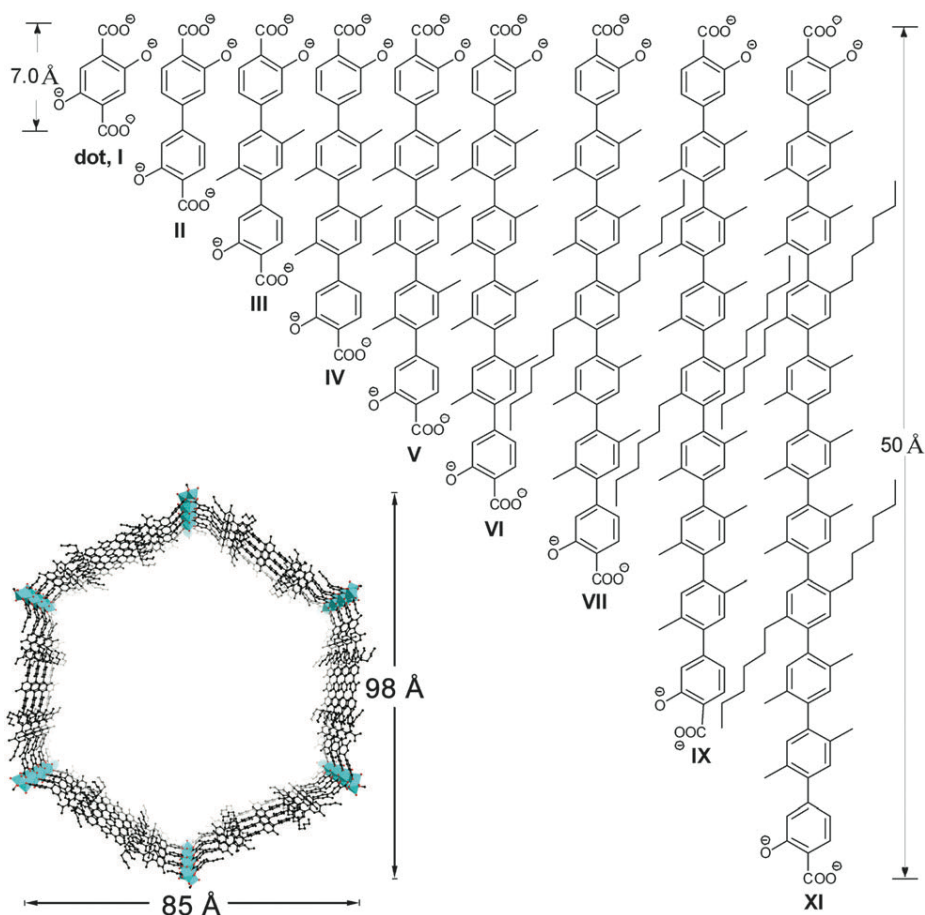


Figure I-8. Chemical structures of organic linkers used in the synthesis of IRMOF-74s. Perspective views of a single one-dimensional channel with 98 Å pore aperture shown for IRMOF-74-XI. Mg (turquoise), O (red), C (black). Reprinted with permission from Ref. 35. Copyright 2014 © Royal Society of Chemistry.

Recently, our groups reported several Zr-MOFs, PCN-228, PCN-229, and PCN-230, by using the isorecticular expansion strategy.³⁶ The MOF series were synthesized from extended porphyrinic ligands, named as H₄TCP-1, H₄TCP-2, and H₄TCP-3, which are isorecticular to PCN-224 (Figure I-9).³⁰ Extra phenyl rings and ethynyl groups were inserted into the arms of the original tetrotopic ligand, H₄TCP, not only for elongating the length of ligands, but also for adjusting the orientation of ligands to fit the templated **ftw-a** topology. Finally, the isorecticular MOFs with the same **ftw-a** topology were achieved. The pore size of these MOFs ranges from 2.5 nm to 3.8 nm and the geometric surface areas of PCN-228 to PCN-230 are calculated to be 4510, 4618 and 4455 m²g⁻¹, which are record-high among the previously reported Zr-MOFs.

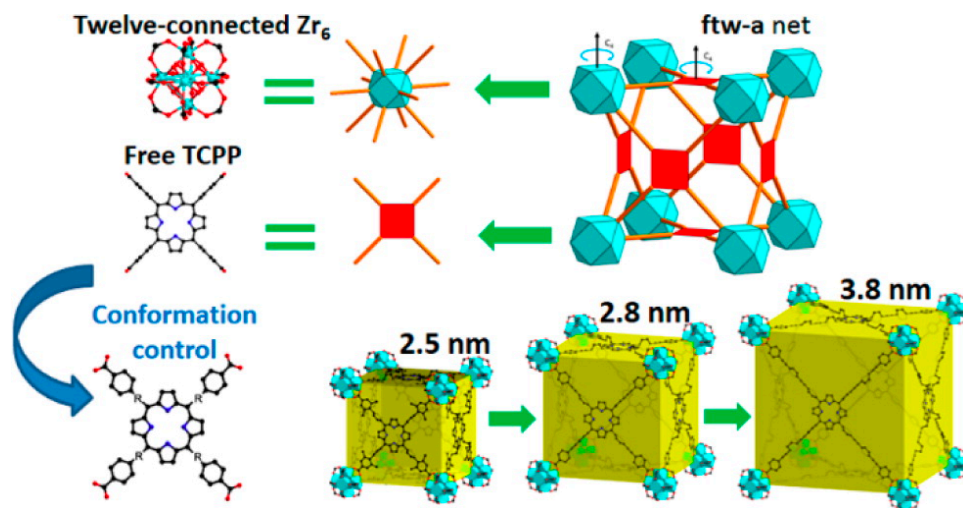


Figure I-9. Graphic synthetic scheme of PCN-228, 229 and 230. Reprinted with permission from Ref. 36. Copyright © 2014, American Chemical Society.

1.1.2.3 Pre-functionalization and Post-synthetic modification (PSM)

The rational design of MOFs is also central to incorporate diverse functionalities into the networks for specific applications, which can be effectively achieved by pre- or post- ligand modification. In pre-functionalization, once a prototype MOF is synthesized, the original ligand of the MOF would be functionalized with certain substituents with the aim of tuning the physical or chemical properties of the framework for host-guest interactions.³⁷ The decorated ligands usually preserve the length and orientation of the ‘parent’ ligand, which could yield the corresponding functionalized MOFs with unchanged topology. The pre-functionalization approach is not only suitable to embed MOFs with some simple pendant groups, such as $-\text{Br}$, $-\text{NH}_2$, $-\text{CH}_3$, $-\text{OC}_3\text{H}_7$, $-\text{OH}$, but can also be applied to anchor some complicated ones on the fragments. One example is MOF-1001, of which the organic linker is pre-incorporated with 36-membered macrocyclic polyethers. The bulky polyether groups prevent the possible interpenetration during the MOF synthesis, maintaining the crystalline primitive cubic structure of the resulted MOF. Moreover, they serve as specific binding sites for paraquat dication (PQT^{2+}) recognition (Figure I-10).³⁸

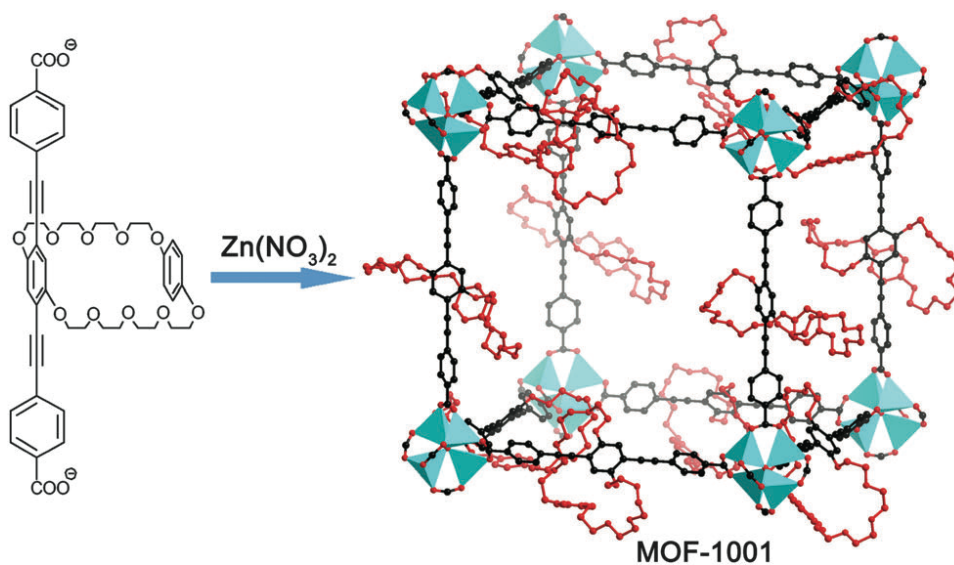


Figure I-10. Synthesis of MOF-1001, a non-interpenetrating cubic structure isoreticular to MOF-5; crown ethers are placed throughout the whole framework. Color scheme: Zn (turquoise polyhedra); O (red); C (black); macrocyclic polyethers (red). Reprinted with permission from Ref. 38. Copyright 2014 © Royal Society of Chemistry.

Similar to the pre-functionalization, functional groups can also be introduced into the frameworks via post-synthetic functionalization (PSM). PSM is defined as the chemical modification of a MOF after its formation in a heterogenous manner.^{23, 37} Compared to pre-functionalization, PSM seems to be a more feasible tool to achieve functionally diverse MOFs with topologically identical structures. The synthesis of a series of functionalized UiO-type MOFs exemplifies the viability of the strategy. Functionalized with azide groups, ligand H₂TPDC could give rise to the highly stable MOFs, PCN-58 and -59, which are isostructural to UiO-68. By facile post-synthetic click reaction with alkynes, the pore walls of the MOFs could be engineered with various triazole-contained functional groups with controllable loading rates (Figure I-11).³⁹

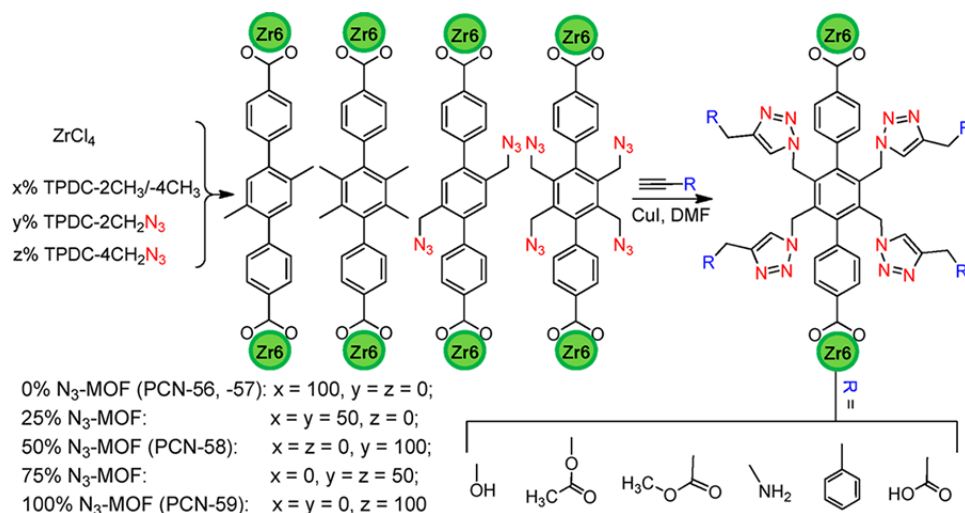


Figure I-11. Schematic illustration of grafting various functional groups onto the pore walls of the MOF via the click reaction between azide and alkyne groups. Reprinted with permission from Ref. 39. Copyright © 2012, American Chemical Society.

UiO analogues could also be post-modified with different functional metal ions via post-synthetic metallation, which often involves decorating unsaturated metal binding groups on the organic linkers. Chelators like bipyridyl, phenylpyridyl or catechol groups are commonly used to build UiO-MOFs with metal binding sites.^{34, 40} After metallated with different metal ions, these MOFs become catalytically active for various organic transformations. For example, a catechol-based MOF, UiO-66-TCAT, was synthesized with 2,3-dimercaptoterephthalic acid (TCAT- H_2BDC) as organic linker.⁴¹ The thiocatecholate (TCAT) ligand provide metal-chelating site for PSM, through which UiO-66-PdTCAT was obtained, which can catalyze regioselective functionalization of sp^2 C-H bonds (Figure I-12).

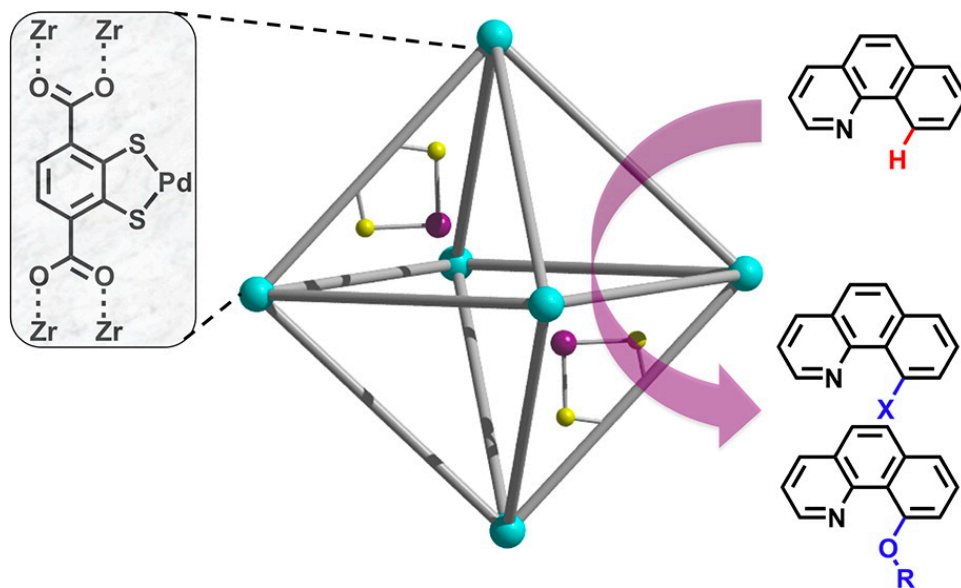


Figure I-12. Synthesis of UiO-66-PdTCAT. Reprinted with permission from Ref. 41. Copyright © 2015, American Chemical Society.

1.2 MOF-Based Heterogeneous Catalyst

1.2.1 Introduction of MOF-Based Catalysts

When it comes to the heterogeneous catalysis, MOFs have demonstrated their superior catalytic activities in various classic organic reactions, such as Friedel–Crafts reaction, Hetero–Diels–Alder reaction, cycloaddition of CO₂, cyanosilylation, isomerization, dehydration, hydrogen evolution, reduction of CO₂, and so on.^{20, 42–43} MOF-based materials are prior to other heterogeneous catalysts in the following aspects : MOFs can be easily functionalized with catalytic active sites on all components (metal clusters, organic linkers, and pores). Meanwhile, due to the structural tunability of MOFs, the chemical environment of catalytic sites can be carefully tailored, leading to chemo, regio, stereo- and/or enantio-selectivities.⁴⁴ At a molecular level, the crystalline nature of MOFs provides such opportunity to well-disperse active sites, which is favored for the mechanism study.

In comparison with homogeneous catalysts, MOFs with rigid frameworks can protect the catalytic species from aggregation or degradation, while homogeneous catalysts are likely to be deactivated if used in the same system. Moreover, with recent endeavors in improving the chemical and moisture stability of MOFs, more and more robust MOFs display excellent reusability without significant loss of crystallinity and catalytic activities.⁴⁵

As one building block of MOFs, organic linker plays an important role in the rational design of MOF-based heterogeneous catalysts.³⁴ Numerous moieties with specific catalytic activities (transition-metal complexes, organocatalysts, Brønsted acids, etc.) have been anchored on organic linkers to expand the scope of MOF-involved catalysis.⁴⁶⁻⁴⁸ In the next section, we will highlight the rational design of catalytic MOFs via linker design, focusing on creating open metal sites on the linker in pursuit of introducing various redox-active metal complexes on the networks via further PSM.

1.2.2 Transition-Metal Complexes on Linkers

1.2.2.1 Direct Incorporation of Well-defined Homogeneous Catalysts on Linkers

In fact, most of catalytic complexes could be embedded on the organic linkers of MOF networks and examples of such direct functionalization will be discussed in the following subsections.

Metalloporphyrins

Porphyrins is such a biological chemical of importance that has been widely investigated in the areas of light-harvesting, oxygen transportation and catalysis.⁴⁹⁻⁵⁰

In this case, these metalloporphyrin derivatives could also be utilized as part of MOFs specifically for biomimetic catalysis.⁵¹⁻⁵² For example, a heme-like linker, Fe-TCPP (TCPP = tetrakis(4-carboxyphenyl)porphyrin), along with $Zr_6O_8(CO_2)_8(H_2O)_8$, was used to afford a mesoporous MOF with 1D channels, namely MMPF-6⁵³, MOF-524⁵⁴, or PCN-222(Fe).⁵⁵ The Fe-metalated MOF displayed superior peroxidase activities compared to the hemoproteins, like myoglobin and horseradish peroxidase (HRP). The electronic properties of the porphyrin center of PCN-224 framework can also be fine-tuned by introducing ethyl, bromo, chloro and fluoro groups into the porphyrin rings, which can consequently change the chemical environment of the catalytic center (Figure I-13).⁵⁶ The resulted MOFs, R-PCN-224(Fe) (R = Et-, Br-, Cl-, F-) have showed distinguish ability in catalyzing the oxidation of 3-methylpentane.

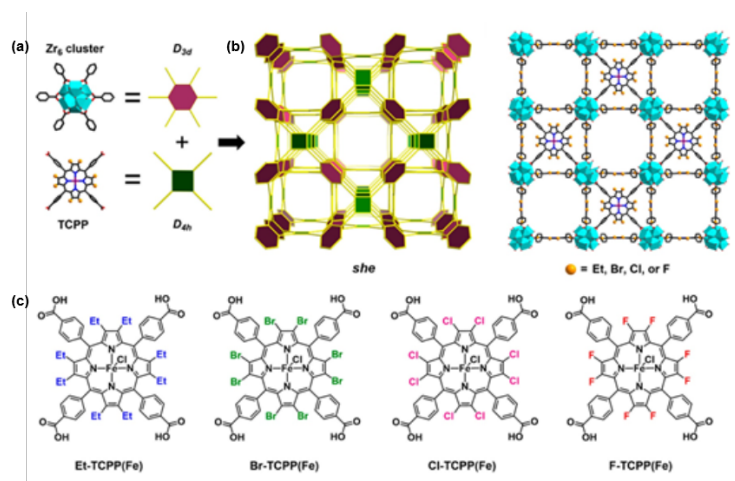


Figure I-13. (a) (b) Assembly of D_{3d} and D_{4h} nodes into (4,6)-connected she topological network. (c) Chemical structures of Et-TCPP(Fe), Br-TCPP(Fe), Cl-TCPP(Fe), and F-TCPP(Fe) linkers. Reprinted with permission from Ref.56. Copyright 2017 @ American Chemical Society.

Polypyridyl Organometallic Complexes

Solar energy, one of the most attractive and abundant renewable energy sources, meets the requirement of mankind's sustainability in the future.⁵⁷ Till now, various artificial photosynthetic molecular systems, polypyridyl organometallic complexes as an example, have been developed for solar energy harvesting.^{43, 58} Using MOFs as platforms to integrate these complexes is also extensively explored in those energy-storing catalysis, water oxidation, photocatalytic hydrogen evolution, CO₂ reduction, photocatalysis of organic reactions, to name a few.⁵⁹ Ir, Re, Ru polypyridyl complexes have been doped on the framework of UiO-67 *via* a mix-and-match strategy in pursuit of turning on the photocatalytic activities of MOF in a range of reactions, including water oxidation, photocatalytic CO₂ reduction and visible light-driven organic transformations (Figure I-14).⁶⁰

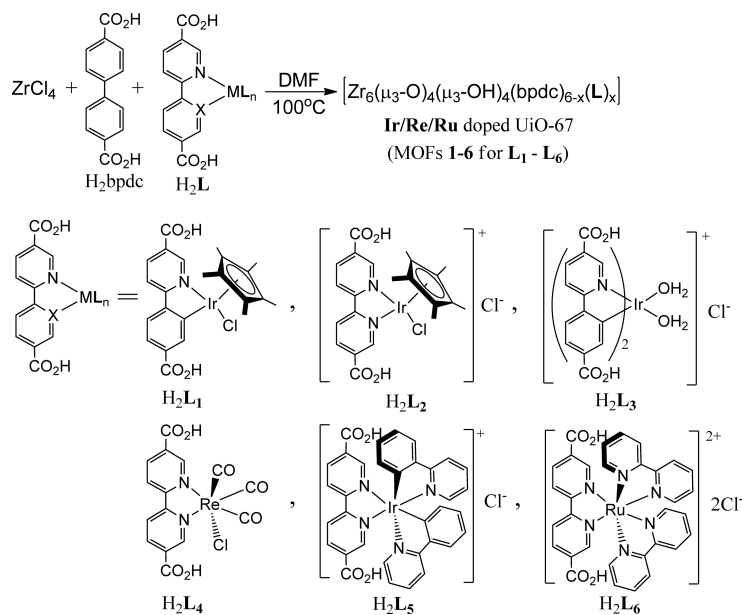


Figure I-14. Synthesis of Doped UiO-67. Reprinted with permission from Ref. 60. Copyright 2011@ American Chemical Society.

N-heterocyclic Carbene Metal Complexes

N-heterocyclic carbene (NHC) transition-metal complexes are another class of advanced catalysts in organic synthesis. Their catalytic activities can be tuned by functionalizing the imidazole sidechain with different substituents.⁶¹ An Ir-NHC metallo linker with alcohol donor group on the imidazole can endow MOFs with the catalytic activity for the isomerization of allylic alcohols.⁶² The alcohol groups on the linker interact with the reactants *via* hydrogen bonding, ultimately enhancing the catalytic performance.⁶³ Pd N-heterocyclic bis-carbene (NHDC) dicarboxylate ligand can construct a new MOF isorecticular to UiO-67. The presence of Pd-NHDC linkers make the MOF capable to catalyze the Heck cross coupling reactions, as well as the intermolecular benzyne-alkene insertion.⁶⁴

Other Transition-Metal Complexes

Besides metalloporphyrin, polypyridyl, and N-heterocyclic motifs, other organometallic complexes can also be incorporated into MOFs for heterogeneous catalysis. For instant, palladium aryl diphosphinite (POCOP) pincer linker was adopted in a Zr-based MOF to catalyze the transfer hydrogenation reactions (Figure I-15).⁶⁵ In the presence of formic acid, the MOF exhibits moderate competency to convert benzaldehyde to benzyl alcohol. Additionally, biomimetic [Fe₂S₂] catalytic sites can also be anchored in MOF-based photocatalysts for hydrogen generation.⁶⁶⁻⁶⁷ The catalytic efficiency is highly dependent on the distance between the reactive center [Fe₂S₂] and photosensitizer, since a close vicinity will facilitate the electron transfer in the process.

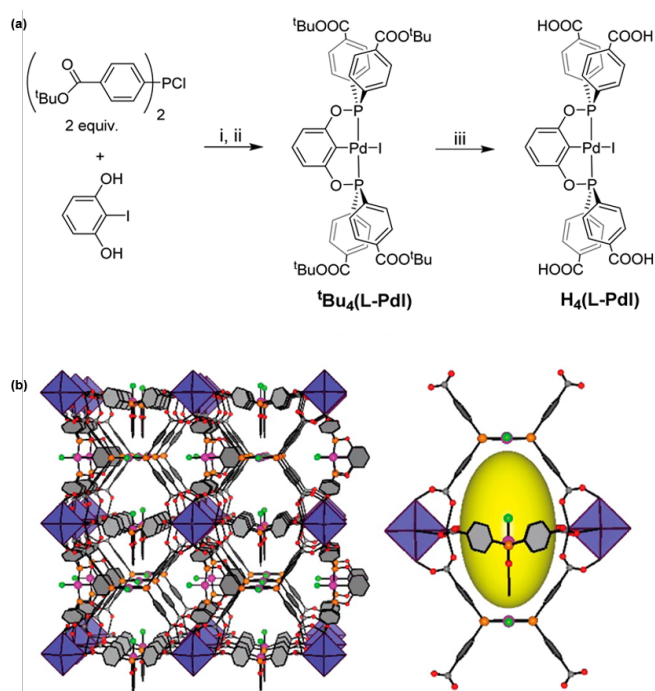


Figure I-15. (a) Synthesis of the pincer ligand. (b) Framework structure. Linker disorder has been omitted for clarity. (c) View of a portion of the framework showing ovoidal pores. Blue octahedra represent $[Zr_6O_4(OH)_4]^{12+}$ building units. Reprinted with permission from Ref. 65. Copyright 2016 @ American Chemical Society.

1.2.2.2 Creating Open Metal Sites on Linkers

Open Porphyrin-Based Chelating Sites

Many MOFs containing metal-free porphyrins have been prepared, and their catalytic activities can be turned on through post-synthetic metalation of the porphyrin center. By introducing Zn^{2+} in the porphyrin center, an aluminum-MOF could generate hydrogen upon the illumination with visible light in the aqueous EDTA/colloidal Pt solution (EDTA = ethylenediaminetetracetic acid).⁶⁸ In the same way, the cationic PCN-233(Fe) was obtained, which turned out to be an excellent recyclable catalyst for hetero-Diels-Alder reaction (Figure I-16).⁶⁹ A Cd^{2+} -incorporated porous 4-fold interpenetrated porphyrinic MOF was also reported and the MOF

can trigger the cyanosilylation of aldehydes with trimethylsilyl cyanide (TMSCN) and Knoevenagel condensation reactions of aldehydes with malononitrile.⁷⁰

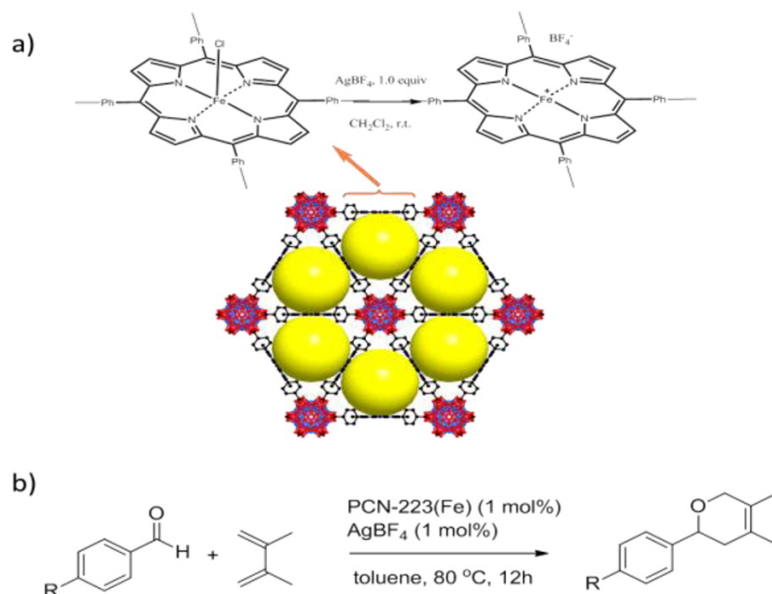


Figure I-16. (a) Preparation of the Cationic Center in PCN-223(Fe); (b) hDA Reaction Catalyzed by PCN-223(Fe). Reprinted with permission from Ref. 69. Copyright © 2014, American Chemical Society.

Bipyridyl Chelating Sites

The bipyridyl moiety in MOFs could also chelate to metals and produce isolated single-site catalysts *via* post-synthetic metalation. In one study, several bipyridine-contained MOFs were synthesized through both direct synthesis and post-synthetic exchange methods, which are isostructural to UiO-67. The modified MOF can readily form complexes with PdCl₂ and the metallated MOFs turns out to be an efficient and reusable catalyst for Suzuki-Miyaura cross-coupling reaction.⁷¹ In another study, UiO-67-Ru(bpy)₃ was afforded to catalyze the aerobic oxidation of arylboronic acids under near UV and visible light.⁷² The two N atoms of the bipyridyl

units can also complex with Cu^{2+} to form a square-planar geometry with another two Br atoms. The resulted MOFs could selectively catalyze oxidation of cyclooctene.⁷³ Furthermore, a series of single-site solid catalysts were afforded by modifying bipyridyl-derived UiO-type MOFs with Co^{2+} (Figure I-17).⁷⁴⁻⁷⁵ These MOFs could be used for catalyzing borylation of arenes, silylation, dehydrogenation with improved activities compared to their corresponding Co-bpy-based homogeneous counterparts.

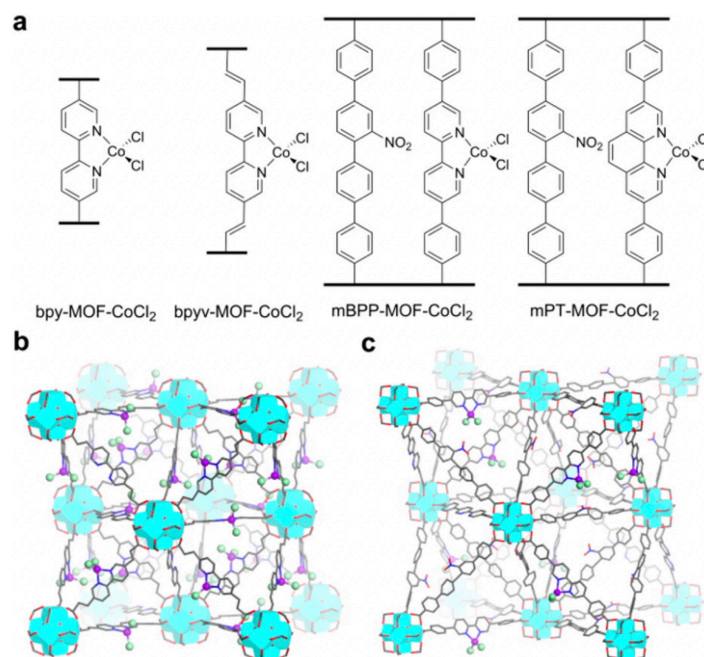


Figure I-17. (a) Schematic structures of the MOF-CoCl₂ precatalysts. (b, c) Idealized structures of bpyv-MOF-CoCl₂ and mBPP-MOF-CoCl₂. Reprinted with permission from Ref. 74. Copyright © 2016, American Chemical Society.

Amino Groups

Amino groups on the MOF struts can also bind to metals. An aluminum-based MOF, assigned as Al-ATA MOF, was prepared from $\text{AlO}_4(\text{OH})_2$ clusters linked by 2-aminoterephalate (ATA).⁷⁶ The amino groups can coordinate with Ni^{2+} cations, forming an active site for hydrogen

production; while the MOF itself is a photocatalyst for oxygen generation. As a result, the Ni²⁺-coordinated MOF demonstrated efficiency when catalyzing the water splitting reaction under UV/Vis light illumination.

On the other hand, the amino group can be easily modified with other organic functional groups in preparation of MOF-supported organometallic catalysts. Several NNN-pincer-contained MOFs were obtained through post-synthetic condensation reactions between the 2-aminoterephthalate linkers with various aminopyridinealdehyde derivatives.^{40, 77-78} Followed by the post-metalation, the resultant (NNN)-M-Zr-MOFs (M = Rh, Ir) put the acid, basic and hydrogenation active sites together, leading to a multifunctional catalytic system for one-pot cascade condensation-hydrogenation reactions with high stability and reusability. Amino-functionalized MOFs can also be post-synthetically modified with salicylaldehyde in the sake of creating salicylaldimine (sal)-based metal chelating sites. A molybdenum sal-organometallic complex was then successfully decorated on the struts of UiO-66, and UiO-67, respectively.⁷⁹⁻⁸⁰ Those modified MOFs turned out to be reusable catalysts for the epoxidation of olefins with *tert*-butyl hydroperoxide (TBHP) or H₂O₂ as the oxidant. Changing the metals to FeCl₂ and CoCl₂ followed by treatment with NaBEt₃H could lead to MOF-based catalysts for alkene hydrogenation.⁸¹ Additionally, the amino-functionalized MOF skeleton can also react with mercaptoacetic acid to form a pyrazolate moiety, which could be subsequently treated with an aqueous solution of AgNO₃ to afford an Ag(I)-anchored MOF. The modified MOF exhibited substantial resistance to alkaline originated from the strong metal-pyrazolate coordination bonds. As it showed strong interactions with CO₂, this MOF was capable to catalyze the cyclic CO₂ carboxylation of propargylic amines without losing its crystallinity under ambient conditions.⁸²

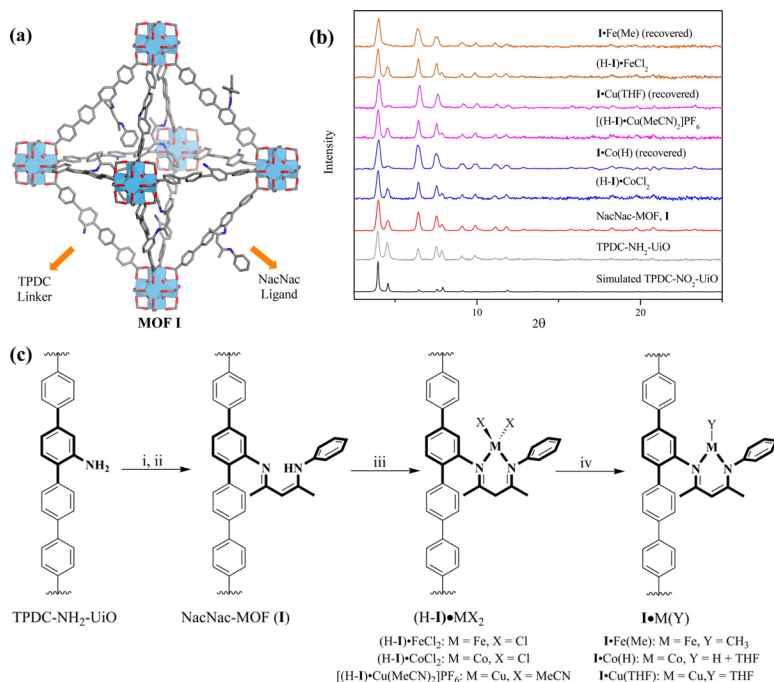


Figure I-18. (a) Structural model showing the octahedral cage of NacNac-functionalized MOF. (b) PXRD patterns of various ion-metalated MOF samples. (c) Synthesis sequence showing NacNac installation and metalation. Reprinted with permission from Ref. 83. Copyright @ 2016, American Chemical Society.

Besides, amino-functionalized MOF can serve as a starting platform for the installation of β -diketiminato (NacNac), a well-studied bidentate ligand as N, N-chelating center. The reported NacNac-M-MOFs (M=Fe, Cu, Co) was constructed through the solvothermal reaction of 2''-amino-[1,1':4',1'':4'',1''':4''',1''':4''']-tetraphenyl-]-4,4''''-dicarboxylic acid (H₂TPDC-NH₂) and ZrCl₄, treatment of alkylated enaminone and addition of different metal salts (Figure I-18).⁸³ The elongated TPDC-NH₂ linker was selected to ensure the accessibility of channels. In comparison with the homogenous catalyst in the catalysis of sp³ C-H amination and alkene hydrogenation, all of the MOF-based catalysts were more active thanks to the isolated active sites.

Other Chelating Sites

Catechol is another common chelator in coordination chemistry. An catalytic mono(catecholate) metal complex was prepared by including the catechol moiety in UiO-66.⁸⁴ Post-metalation of the catechol parts gave rise to Fe-monocatecholato and Cr-monocatecholato MOFs, and the latter turned out to be an active and efficient catalyst for oxidation of alcohols to ketones even with low metal loadings (0.5-1 mol %). Similarly, BINAP (BINAP = 2,2'-bis(diphenyl-phosphino)-1,1'-binaphthyl) -derived dicarboxylate linker was also introduced into the network to construct a chiral MOF (Figure I-19).⁸⁵ As BINAP is usually utilized to chelate late transition metal for asymmetric catalysts, the BINAP-based MOF was able to catalyze asymmetric hydrogenation of substituted alkene and carbonyl compounds, addition of arylboronic acids and AlMe₃ to α , β -unsaturated ketones after metalation with Ru.⁸⁶ The Ru-BINAP-based MOF not only presents three times activity comparing to the homogeneous one but also produces aryl addition products with an *ee* more than 99%. The BINAP linker could also form complex with Rh, which is active for the asymmetric reductive cyclization, Alder-ene cycloisomerization as well as asymmetric Pauson–Khand-type reactions.⁸⁷

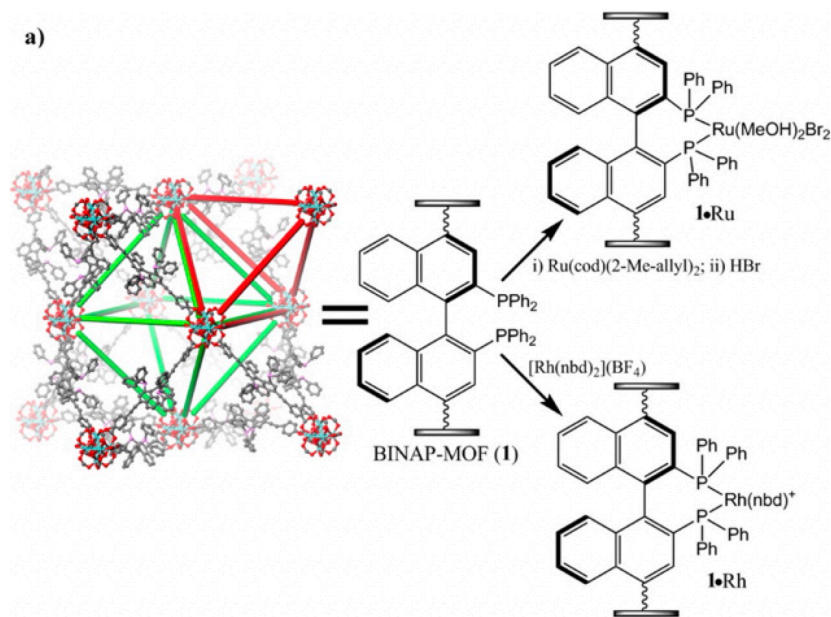


Figure I-19. Post-synthetic metalation of BINAP-MOF (1) to form $1 \cdot \text{Ru}$ and $1 \cdot \text{Rh}$. Reprinted with permission from Ref. 85. Copyright @ 2014, American Chemical Society.

1.2.3 Summary

The modifications on the organic struts of MOFs with specific catalytic moieties provide an accessible and efficient method to introduce new catalytic capabilities into MOFs. The homogeneous organometallic catalysts could be unitized as part of building blocks of MOFs. They can not only be directly anchored on the linkers to build MOF struts, but can also be derived from the open metal chelating sites preinstalled on the organic linkers through post-synthetic metalation. The functionalized MOFs inherit the catalytic capabilities from the organometallic species, meanwhile, there are also cases where MOF-based catalysts demonstrated enhanced catalytic efficiency compared to that of the homogeneous analogues. The rigidity of the frameworks prevents the active sites from undesired aggregation or decomposition. Moreover, the diverse and

tunable structures of MOFs may improve the selectivity, which might not be observed in the homogeneous systems.

1.3 MOF-Based Luminescent Sensors

Luminescent materials have long held a strong fascination for scientists and lay people alike. They are those materials that release energy in terms of, other than thermal radiation, light upon excitation by outside stimulus, such as X-rays, electron beams, UV light, or even mechanical phenomenon.⁸⁸⁻⁸⁹ The key to spark luminescence of the materials, hence, is to block non-radiative pathways, which is often involved with building rigid scaffolding to prevent molecular vibrations through material architecture.⁹⁰ Recently, luminescent materials have gained much attention for their use as chemical sensing agents or in the realm of biomedical science.⁹¹ The main advantage of luminescent materials over other transduction ones is that they can quickly and easily give a colorimetric response to stimuli. Additionally, luminescent materials can be used in conjunction with spectrophotometers, allowing the identification of the sensed material based on the characteristic absorption and emission shifts.⁹²

As a viable luminescent sensor, several requirements need to be satisfied. Firstly, the material needs to respond to an analyte in a given area. The capability of trapping analyte molecules to a desired local concentration would contribute to high sensitivity. Secondly, an excellent sensor should be insensitive towards possible undesired luminescent quenching, which could be induced by testing environments. Moreover, chemical and physical stability are also required so that efficient testing can be performed in extreme environments.

Among numerous reported luminescent materials, luminescent MOFs (LMOFs) recently bloom out as potential chemical sensors due to their easily induced luminescence, diverse

advantages in structural and functional components, and various detecting mechanisms.

1.3.1 Origins of Luminescence in MOF-Based Sensors

With the inherent hybrid nature, luminescence of MOFs can arise from either organic linkers or metal ions. Linker-centered luminescence is the most common one, which includes three subtypes: linker emission, ligand-to-metal charge transfer (LMCT) and metal-to-ligand charge transfer (MLCT).⁹³ In general, linker emission, as its name, stems from fluorescent linkers with aromatic or π -conjugated moieties on the backbones. LMCT is often seen in MOFs composed of transition-metal ions in d^{10} configuration, such as in Zn(II)⁹⁴ and Cd(II),⁹⁵⁻⁹⁶ which contains core-like orbitals. Similarly, MLCT occurs in d^{10} transition metal based MOFs such as Cu(I)⁹⁷⁻⁹⁸ and Ag(I)⁹⁹ -MOFs where the d electrons of the Cu (I) and Ag (I) ions are localized in the valence orbitals, making MLCT possible. Metal-centered luminescence, on the other hand, often occurs in MOFs with lanthanide ions, where they are used as secondary building units (SBUs) or doped within the pores. Lanthanides are sensitized by organic chromophores via antenna effects, emitting characteristic sharp and strong luminescence.¹⁰⁰ Besides the framework based-luminescence, luminescence can also originate from chromophores trapped within the non-emissive MOF pores or bound to the surface of the networks (Figure I-20).

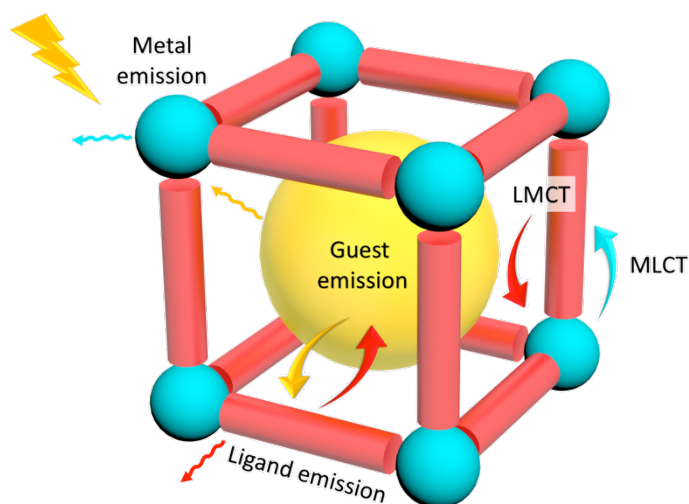


Figure I-20. Representation of possible emission modes in MOFs. Inorganic SBUs, blue spheres; Organic linkers, red cylinders; Guest chromophores, yellow sphere inside. Reprinted with permission from Ref.15. Copyright © 2017, Elsevier B.V.

1.3.2 Detecting Mechanism of MOF-Based Sensors

By taking advantage of MOFs porosity, selective detection of analytes can be realized via size exclusion. The apertures of the MOFs serve as a sifter to allow specific molecules to come inside, which will further change the luminescence of the host.¹⁰¹⁻¹⁰² Another mechanism is decorating extra metal open sites like Lewis basic/acidic sites on the organic linkers in pursuit of preferentially interacting with target molecules, especially ionic species.¹⁰³ In MOF system, the most common analyte-sensor interaction is host-guest electron transfer. Since the energy level of lowest unoccupied molecular orbitals (LUMOs) for most analytes generally lies below the LUMOs or conduction bands (CBs) for MOFs, the electron transfer from MOFs to guest molecules is highly possible.¹⁰⁴ Energy transfer between host and guest is also crucial in MOF-based sensing, which is highly dependent on the degree of overlap between the absorption of the analytes and emission

of the sensors.¹⁰⁵ Generally, energy transfer works synergistically with electron transfer mechanism, leading to the change of fluorescence.

1.3.3 Virtues of MOFs as Sensors

LMOFs stand out as a unique type of sensors compare to other traditional luminescent sensors. As other reviews have demonstrated, the porous nature of MOFs can adsorb and pre-concentrate the analytes, increasing the possibility of host-guest interactions and further improving the sensitivity of those sensors.^{101, 106} Selectivity can be realized by tuning the pore size and apertures of MOFs. On the one hand, microporous MOFs can block the access to the oversized molecules, which is known as molecular sieving. On the other hand, some mesoporous MOFs enable the uptake and detection of large molecules, bio-pollutants as an example.

Another merit of MOF-based sensors, compared to other amorphous materials, is their well-defined crystalline structures, which allows the investigation of sensing mechanisms of the frameworks at molecular level.¹⁰⁷⁻¹⁰⁸

LMOFs also distinguish themselves from other organic luminescent materials by their ease of functionalization. Functionalized MOFs can be prepared from easy-synthesized building blocks via either pre- or post-synthetic modification.²² In terms of MOF-based sensors, luminescence can be fine-tuned in various ways within MOFs. With similar structures, the emission characteristics of MOFs can be simply varied by changing the conjugation degree of a linker.¹⁰⁶ Variations in luminescence can also be generated by altering the orientation and connectivity between the SBUs and organic units.¹⁰⁹ For guest-induced luminescence, emission can be precisely adjusted by the amount of captured fluorophores.¹¹⁰⁻¹¹¹ In other cases where luminescence rises from the metal ions, lanthanide-based MOFs typically, the emission can be tuned by utilizing the mixtures of

lanthanide ions in different ratios.¹¹²

1.3.4 Chemical Sensing

A chemical sensor, as it is defined, is a self-contained analytical device that can provide information about the chemical composition of its environment.⁹³ LMOF-based chemosensors usually show a guest-dependent solvatochromism or vaporchromism in optical signals, providing a more direct and convenient method. The detection procedure can be simplified to either soaking the powdered materials into analyte-containing solutions or exposing the materials to the vapors or pure gases and afterwards, investigating the change in luminescence. The simplicity of the analyte-exposure approach highlights the sensing feasibility of MOFs over other high-cost sensing techniques, such as gas chromatography (GC), GC-MS as well as other techniques that require large scale equipment.

1.3.4.1 Cations Sensing

Iron plays an indispensable role in biological systems, most significantly as an oxygen carrier in the blood stream. Either excessive or deficient levels of iron can break cellular homeostasis, leading to disorder.¹¹³ Hence, many LMOFs are being utilized to detect Fe^{3+} and Fe^{2+} . The detection of Fe^{3+} can be achieved by a chiral lanthanide-based MOF, $[\text{Tb}(\text{BPTC}-2)] \cdot (\text{Me}_2\text{NH}_2) \cdot (\text{solvents})_x$ ($\text{H}_4\text{BPTC}-2$ = biphenyl-3,3',5,5'-tetracarboxylic acid) reported by Bu and coworkers.¹¹⁴ Fe^{3+} ions invoke a strong quenching effect on the emission intensity by interacting with the chiral helical channels of the MOF material. Another case is a 2D MOF nanosheet, NTU-9-NS (NTU = Nanyang Technological University), $[\text{Ti}_2(\text{HDOBDC})_2(\text{H}_2\text{DOBDC})]$ (H_2DOBDC , 2,5-dihydroxyterephthalic acid), which display

excellent capability to probe Fe^{3+} with high sensitivity and fast response.¹¹⁵ The nanosheet greatly extends the surface areas of the MOF structure, making the active sites more accessible to Fe^{3+} than those in bulk-size MOFs. As a result, the sensing efficiency was greatly improved (Figure I-21).

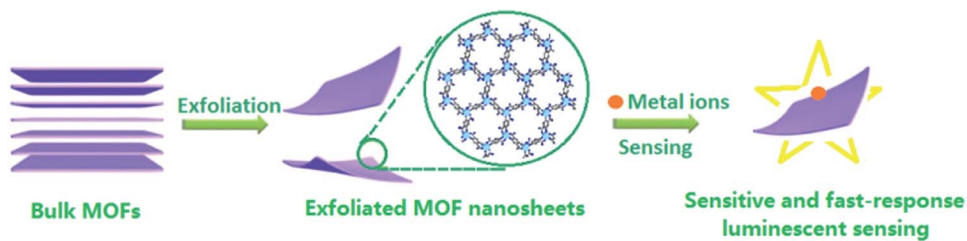


Figure I-21. The schematic illustration for the fabrication and metal ions luminescent sensing of the two-dimensional MOF nanosheets materials. Reprinted with permission from Ref. 115. Copyright 2016 © Royal Society of Chemistry.

1.3.4.2 Sensing for Explosives and Organic Energetic Compounds

The detection of explosives via MOF-based sensors is usually performed in a ‘turn-off’ manner, where the fluorescence of MOFs can be quenched by the analytes via photoinduced electron or energy transfer. The higher-energy CBs of most LMOFs make it possible for the electron transfer from the HOMOs of the MOFs to the LUMOs of an electron-deficient analytes.¹⁰⁴ The existence of long-distance energy transfer is demonstrated by the overlap between the emission spectra of the MOF sensors and the absorption spectra of the analytes.¹¹⁶⁻¹¹⁷ Electrostatic interactions also play an important role in sensing explosives, which are often seen in detecting nitrophenol-based explosives like 2,4,6-trinitrophenol (TNP). Functional groups, such as pendant Lewis basic amines¹¹⁸ or amides,¹⁰⁵ are often introduced into the frameworks to selectively interact with the phenolic protons via ionic interactions.

The sensing efficiency of LMOFs towards explosives can be quantitatively characterized using quenching constant K_{sv} (M^{-1}) and detection limits. The quenching constant (K_{sv} , M^{-1}) is calculated by using the Stern–Volmer (SV) equation: $(I_0/I) = 1 + K_{sv}[Q]$, where $[Q]$ is the molar concentration of the analyte and I_0 and I are the luminescence intensities before and after addition of the analyte; K_{sv} values combined with the standard deviation (S_b) can be used to calculate the detection limit, defined as nS_b/K_{sv} .

‘Turn-on’ detection of explosives or explosive-like molecules is rare but highly desirable due to their more rapid and obvious response inherent in visible signals. A series of MOFs, termed as TABD-MOF-1, -2, and -3, demonstrated the ‘turn-on’ detection of energetic heterocyclic compounds.¹¹⁹ In the MOFs, a novel ligand, TABD-COOH (TABD-COOH = (4,4'-((Z,Z)-1,4-diphenylbuta-1,3-diene-1,4-diyl)dibenzoic acid), with aggregation-induced emission (AIE) feature is used to construct MOFs with two paramagnetic Ni^{2+} and Co^{2+} SBUs. The Ni^{2+} and Co^{2+} ions tend to quench the luminescence of the constructed TABD-MOF series via LMCT, creating a dark background. After adding the solution of 5-membered-ring energetic heterocyclic compounds to the MOF suspension, the C=N and N=N bonds in the heterocyclic rings competitively coordinate to the metal clusters, damaging the MOF structure. Consequently, the released AIE linkers form emissive aggregates in solutions and turn on the luminescence (Figure I-22).

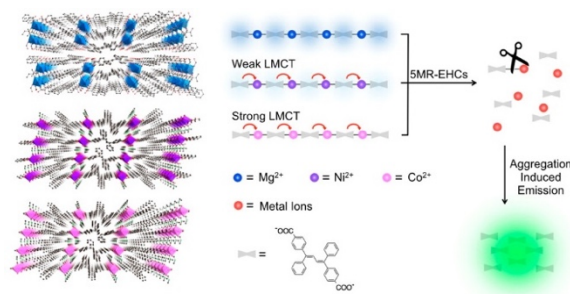


Figure I-22. Schematic representation of the mechanism for the detection of energetic heterocyclic compounds by TABD-MOFs. Reprinted with permission from Ref. 119. Copyright @ 2014, American Chemical Society.

1.3.5 Summary

Driven by the increasing research interests of scientists, the field of utilizing LMOFs as probes or chemical sensors has been developing rapidly in the last few years. Hundreds of LMOFs-based sensors have been judiciously designed and demonstrated great achievement for detecting various species, such as ions, VOCs, gases, explosives and biomaterials. In addition, some of them are excellent fluorescent thermometers, providing precise temperature information at different environments.

Probes or chemosensors that exhibit fluorescence changes in response to different analytes are more convenient than other types of sensors, as they produce optical signals that can be recognized easily either by fluorimeters or by the naked eyes. It has been well established lately that LMOFs make excellent sensors due to their inherent advantages, such as crystallinity, permanent porosity, structural and functional diversity and tunable luminescence. Various MOF-based sensors with different detecting mechanisms have been achieved through rational design. The ‘turn-off’ mechanisms are commonly used when detecting electron acceptors, where luminescence is quenched through sensor-guest electron transfer accompanied with energy

transfer. The 'turn-on' detection mode has also been studied, which generally leads to luminescent enhancement or wavelength shifts.

Despite of those LMOFs, whose sensing behaviors of have been comprehensively studied, there is always space for improvement. Though many reported MOFs show fast responses to analyte solvents, fast gas phase detection is still challenging which hinders their applications. Moreover, most reported MOF-based sensors are sensitive to a family of guests whereas selective detection of a specific species is difficult, especially when the analytes have similar chemical structures. Finally, in-depth studies on the structure-luminescence relationships as well as host-guest interactions have yet to be explored computationally in great detail.

CHAPTER II

A NNN-PINCER-BASED MOF SCAFFOLD FOR PREPARATION OF NOBLE-METAL-FREE CATALYST³

2.1 Introduction

As a burgeoning class of highly crystalline porous materials, metal-organic frameworks (MOFs) have attracted immense attention in the past two decades. The surging interest in MOFs is mainly driven by their unique properties such as permanent porosity, structural diversity, and functional tunability.^{1, 11} The exquisite assembly of a variety of inorganic metal clusters and organic linkers imparts MOFs with enormous potentials in various applications, especially in heterogeneous catalysis.^{12, 16, 20, 120-121} MOFs have turned out to be a feasible platform to accommodate catalytic active sites for organic transformations. Due to confinement effects of the framework, MOF-based heterogeneous catalysts own higher, if not, comparable activity and selectivity to homogeneous counterparts. Moreover, the stability of MOF increases the recyclability of the materials.¹²²⁻¹²³ General approaches of introducing catalytic sites into the MOF scaffolds involve guest encapsulation, covalent grafting and linker functionalization.¹²⁴⁻¹²⁷ Although the linker design approach is often synthetically more demanding, it stays an attractive method owing to the resultant high loading of uniformly distributed catalytic sites on the scaffold.

Organometallic complexes have risen to prominence in accelerating organic reactions in homogeneous catalysis these days.¹²⁸ They have also paved ways towards building catalytic active

³ Reproduced with permission from “A mesoporous NNN-pincer-based metal-organic framework scaffold for the preparation of noble-metal-free catalysts” by Zhang, Y.; Li, J.; Yang, X.; Zhang, P.; Pang, J.; Li, B.; Zhou, H. C., *Chem. Commun.*, **2019**, 55 (14), 2023-2026, copyright © 2019 Royal Society of Chemistry.

MOFs.¹²⁹ Through rational design of linker, organometallic complexes with versatile chelating ligands have been embedded on MOFs via direct assembly or post-synthetic modification (PSM).^{87, 130-133} However, there are fewer examples of MOFs constructed by pincer-containing linkers.^{65, 77-78, 134} Their ubiquity in MOFs was partially impeded by their harsh synthetic conditions in both ligand preparation and MOF synthesis. Considering their specific roles in catalysis, it remains an urgent task to introduce the pincer complexes into MOF template with the aim of expanding the scope of MOF-catalyzed transformations. Classified as a neutral NNN-type pincer ligand, terpyridine and its derivatives possess superb coordination capability, which enables them to complex with redox-active metals under relatively mild conditions. In addition, their metal complexes have been widely utilized in organometallic catalysis, biomimetic oxidation and reduction reactions, etc.¹³⁵⁻¹³⁸ To date, most terpyridine-constructed MOFs adopt interpenetrating structures, which block their catalytic behaviours due to the low diffusion efficiency of substrates.¹³⁹⁻¹⁴² Although the constraint can be released by synthesizing ultrathin 2D metal-organic layers (MOLs),¹⁴³⁻¹⁴⁴ a 3D mesoporous MOF to embody terpyridine-based moiety for heterogeneous catalysis is still highly desirable.¹⁴⁵⁻¹⁴⁷

Bearing all these in mind, we herein report a newly synthesized mesoporous MOF, namely PCN-308, adopting a β -cristobalite-type structure. The MOF incorporates well-arranged terpyridine coordination sites for facile post-synthetic metalation, which can be effectively applied as a general scaffold for the preparation of noble-metal-free catalysts. For instance, the scaffolded metal@MOF materials exhibit highly efficient catalytic activities for alkene epoxidation and arene borylation.

2.2 Experimental Section

2.2.1 Materials and Instrumentation

Materials

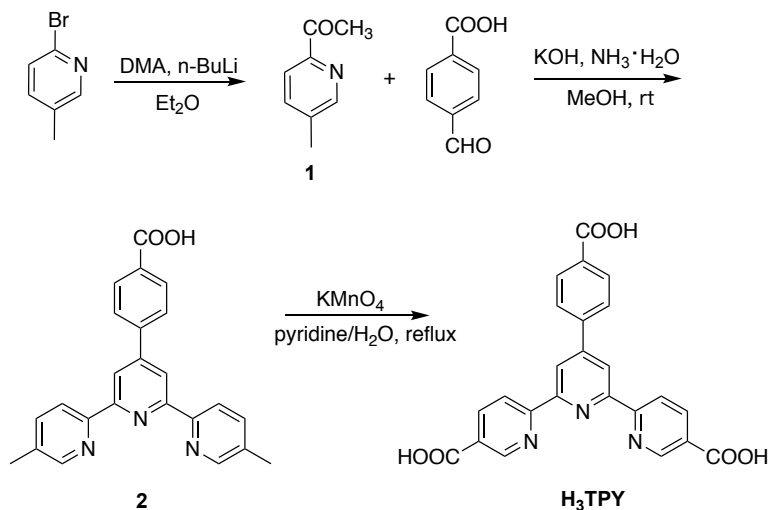
2-bromo-5-methylpyridine, 4-carboxybenzaldehyde, n-butyllithium solution, *N,N*-diethylformamide (DEF), *N,N*-dimethylformamide (DMF), $\text{ZrOCl}_2 \cdot 8\text{H}_2\text{O}$, trifluoroacetic acid, ammonium chloride, sodium hydroxide, magnesium sulfate, potassium permanganate, $\text{NH}_3 \cdot \text{H}_2\text{O}$, methanol, ethyl ether, chloroform, 2,2':6',2''-terpyridine were purchased from either VWR or Sigma Aldrich. Unless otherwise noted, all commercial chemicals were used without further purification.

Instrumentation

Synchrotron powder X-ray diffraction (PXRD) was carried out with Bruker D8-Discover diffractometer equipped with a Mo sealed tube ($\lambda = 0.72768 \text{ \AA}$) on the beamline 17-BM at the Advanced Photon Source, Argonne National Laboratory. In-house powder X-ray diffraction (PXRD) was carried out on a Bruker D8-Focus Bragg-Brentano X-ray powder diffractometer equipped with a Cu sealed tube ($\lambda = 1.54178 \text{ \AA}$) at 40 KV and 40 mA. Fourier transform infrared (FT-IR) spectra were recorded on an IR Affinity-1 instrument. Thermogravimetric analysis (TGA) were carried out on a Shimadzu TGA-50 thermogravimetric analyzer from temperature to 600 °C at a ramp rate of 5 °C /min in a flowing air atmosphere. Nuclear magnetic resonance (NMR) data were collected on a Mercury 300 spectrometer. Low pressure gas adsorption measurements were performed on an ASAP 2020 with the extra-pure quality gases. Morphology of PCN-308 powder was observed by JEOL JSM-7500F Scanning electron microscope (SEM) and energy dispersive X-ray spectroscopy (EDS) was performed on Oxford EDS system equipped with X-ray mapping and digital imaging. Inductively Coupled Plasma-Optical Emission spectroscopic (ICP-OES) data

were collected on a Thermo iCAP-6300 Spectrometer. X-ray photoelectron spectroscopy (XPS) was performed on Omicron XPS system with argue detector.

2.2.2 Ligand Synthesis



Scheme II-1. Synthesis of H₃TPY

Ligand 4'-(4-carboxyphenyl)-[2,2':6',2''-terpyridine]-5,5''-dicarboxylic acid (H₃TPY) was synthesized with modified procedure according to the previously reported literature.¹⁴⁴

Step 1. Synthesis of 1-(5-methylpyridin-2-yl)ethan-1-one (1)

In a 500 mL round-bottom flask, 2-bromo-5-methylpyridine (17.2 g, 100.0 mmol) was dissolved in 200 mL dry Et₂O. The mixture was cooled to -78 °C and n-BuLi (62 mL, 1.6 M in hexane) was added dropwise. After stirred at -78 °C for 90 mins, 10 mL dimethylacetamide (DMA) was added into the system, which was allowed to react for another 5 h at room temperature. The reaction mixture was then quenched with NH₄Cl saturated aqueous solution. The Et₂O layer

was separated and the aqueous layer was extracted with Et₂O several times. The organic parts were collected, dried with anhydrous MgSO₄ and the organic solvent was pumped out under vacuum. The obtained liquid was further purified by column chromatography (eluent: EtOAc/CH₂Cl₂ = 1/18) to afford colorless oil product (10.9 g, yield: 80.7%). ¹H NMR (300 MHz, CDCl₃) δ 8.43 (s, 1H), 7.88 (d, J = 8.0 Hz, 1H), 7.56 (m, 1H), 2.64 (s, 3H), 2.35 (s, 3H).

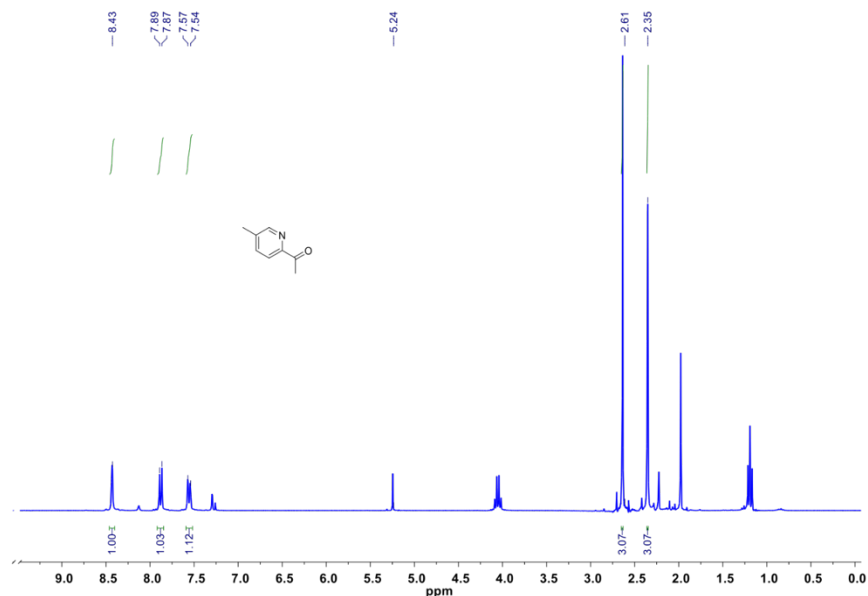


Figure II-1. ¹H NMR spectrum of 1-(5-methylpyridin-2-yl)ethan-1-one.

Step 2. Synthesis of 4-(5,5''-dimethyl-[2,2':6',2''-terpyridin]-4'-yl)benzoic acid (2)

As-synthesized 1 (5.3 g, 39.2 mmol), 4-carboxybenzaldehyde (3 g, 20.0 mmol), 100 mL MeOH, 15 % KOH aqueous solution (140 mL) and NH₃·H₂O (27 mL) were charged in a 500 mL round-bottom flask and allowed to react for three days at room temperature. White precipitate came out, which was filtered and washed with CHCl₃ several times. The obtained solid was then dissolved in a mixture of MeOH/H₂O (v/v = 1/1) followed by the addition of 1 M HCl until pH = 3. The obtained solid was formed, filtered, washed with water and dried to give white solid product

(8.2 g, yield: 55 %). $^1\text{H NMR}$ (300 MHz, DMSO) δ 8.99 (d, $J = 8.4$ Hz, 2H), 8.90 (s, 2H), 8.81 (s, 2H), 8.37 (d, $J = 8.3$ Hz, 2H), 8.19 (d, $J = 8.3$ Hz, 2H), 8.10 (d, $J = 8.4$ Hz, 2H), 2.52 (s, 6H).

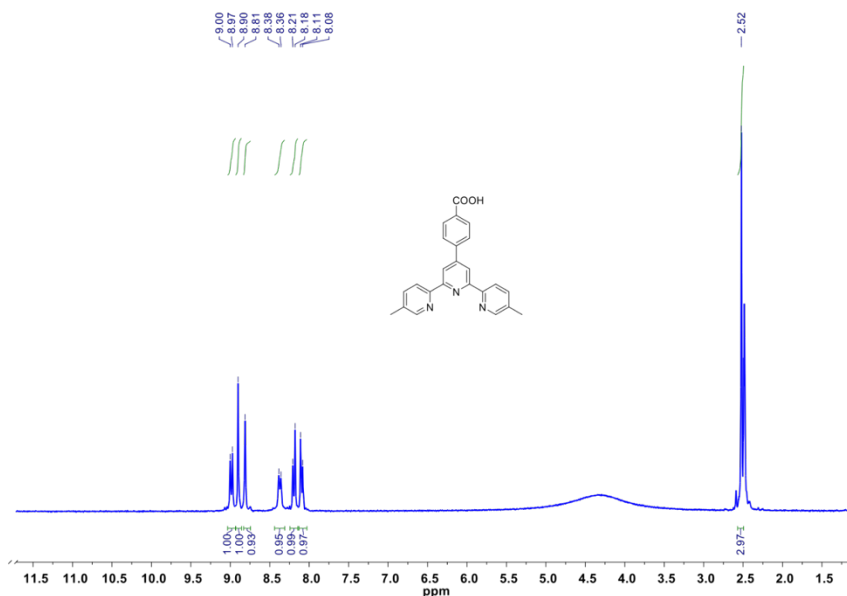


Figure II-2. $^1\text{H NMR}$ spectrum of 4-(5,5''-dimethyl-[2,2':6',2''-terpyridin]-4'-yl)benzoic acid.

Step 3. Synthesis of 4'-(4-carboxyphenyl)-[2,2':6',2''-terpyridine]-5,5''-dicarboxylic acid (H_3TPY)

In a 500 mL three-necked flask, as-synthesized **2** (2.0 g, 5.3 mmol) was added into a mixing of pyridine/ H_2O (v/v = 4/1, 250 mL). The mixture was heated up and 32 g KMnO_4 was added in portions with 8 g each time. The system was then stirred under reflux overnight. After that, the reaction was cooled down, filtered and the dark filter cake was washed with methanol several times. The obtained clear filtrates were combined and the organic solvent was removed under vacuum. The residual aqueous part was acidified with 6 M hydrochloric acid to adjust pH to 3. White precipitate was formed, filtered, washed with water several times and air-dried (2.15 g, yield:

92%). ^1H NMR (300 MHz, DMSO) δ 9.18 (s, 2H), 8.76 (s, 2H), 8.71 (d, $J = 8.3$ Hz, 2H), 8.44 (d, $J = 10.2$ Hz, 2H), 8.11 (d, $J = 8.3$ Hz, 2H), 8.01 (d, $J = 8.3$ Hz, 2H).

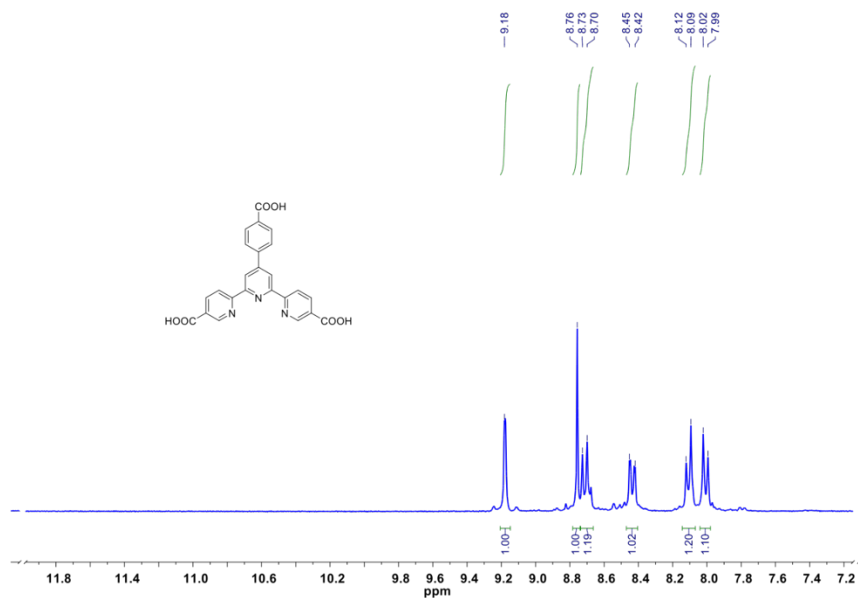


Figure II-3. ^1H NMR spectrum of H_3TPY .

2.2.3 Synthesis of PCN-308

In a 20 mL Pyrex vial, $\text{ZrOCl}_2 \cdot 8\text{H}_2\text{O}$ (200mg), H_3TPY (60mg) and 610 μL trifluoroacetic acid (TFA) were ultrasonically dissolved in 12mL of N, N-diethylformamide (DEF). The mixture was heated in a 120 $^\circ\text{C}$ oven for 12h to give white crystalline powder. Yield: 53 mg.

2.2.4 Activation of PCN-308

Prior to gas sorption, ~ 50 mg as-synthesized PCN-308 was washed with DMF two times and acetone three times. The sample was further soaked in acetone for solvent

exchange with replacement of fresh acetone three times. Afterwards, the sample was placed in the chamber and the occupied solvent was completely exchanged with liquid CO₂ for 2 hours. The temperature was then raised to 40 °C and kept under the supercritical condition for another 2 hours. After that, the CO₂ was slowly vented from the chamber within 3 hours. The activated sample was immediately tested for nitrogen adsorption without further degas activation.¹⁴⁸

2.2.5 Post-Synthetic Metalation (PSM) of PCN-308

Fe@PCN-308

~ 5 mg as-synthesized PCN-308 was exchanged with acetonitrile for three times and stocked in an acetonitrile solution of Fe(ClO₄)₂·6H₂O (~ 10 mg, 3 mL). The mixture was stirred at room temperature for three hours and then washed thoroughly with fresh acetonitrile for three times and methanol for two times before further measurements.

Co@PCN-308

~ 5 mg as-synthesized PCN-308 was exchanged with toluene for three times and stocked in a toluene solution of Co(OAc)₂ (~ 5 mg, 3 mL). The mixture was stirred at room temperature for three hours and then washed thoroughly with fresh toluene for three times and methanol for two times before further measurements.

2.2.6. Investigation of Catalytic Performance

Screening Experiments of Fe@PCN-308 in Catalyzing Styrene Epoxidation

To a 4 mL Pyrex vial was added styrene (0.2 mmol), Fe@PCN-308, solvent (2mL) and TBHP (2.0 equiv.). The mixture was stirred at room temperature. When finished, the solid part

was removed by centrifuge and 30 μL of mesitylene were added to the solvent residue as internal standard for GC-analysis to determine the corresponding yields.¹³⁵

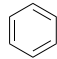
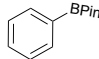
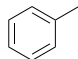
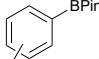
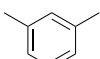
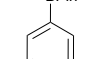
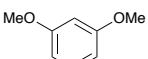
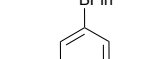
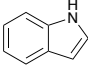
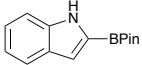
Universal Capability of Fe@PCN-308 in Catalyzing Epoxidation of Various Olefins

To a 4 mL Pyrex vial was added olefins (0.2 mmol), catalyst (1 mol%), solvent (2mL) and TBHP (2.0 equiv.) and the mixture was stirred at room temperature.

Co@PCN-308 as Catalyst for Borylation of Arenes

Arenes (5.7 mmol), B_2Pin_2 (0.38 mmol) and catalyst (5% mol) were sealed with a screw cap fitted with teflon septa in glove box. Samples were brought out of the glove box and heated for 48 h under the protection of N_2 . After six hours, caps were open to terminate the reactions. Yields were determined by GC-analysis with mesitylene as the internal standard.¹³⁶ Control Experiments were performed by using homogeneous Co-TPY and Non-metalated PCN-308 as catalysts, respectively.

Table II-1. Borylation of Arenes catalyzed by the homogeneous Co-TPY and non-metalated PCN-308.

Entry	Substrate	Product	% Yield		
			$[(\text{CO}_2\text{Me})_3\text{tpyCo}(\text{OAc})_2]$	PCN-308	Fe@PCN-308
1			36	—	—
2			30	—	—
3			25	—	—
4			12	—	—
5			10	—	—

2.3 Results and Discussion

2.3.1 Topology Design and Structural Description of PCN-308

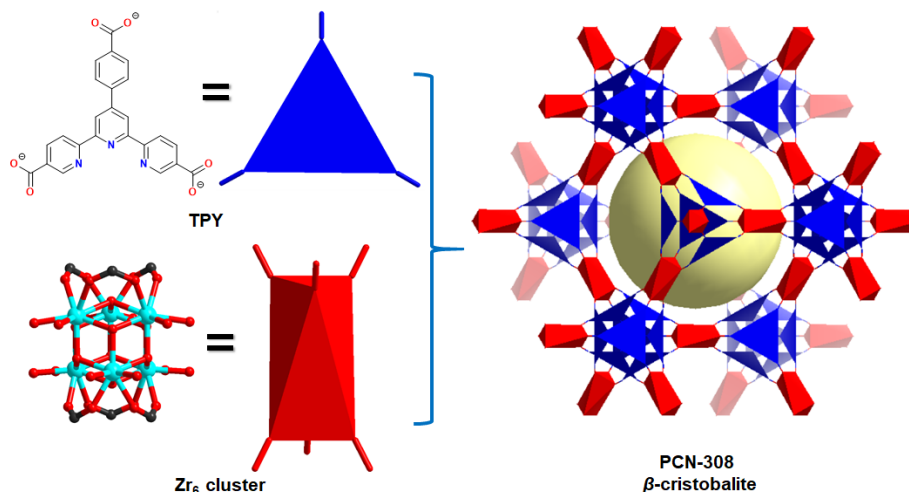


Figure II-4. a) Trigonal-planar organic linker TPY and six-connected D_{3d} -symmetric Zr_6 antiprismatic cluster. b) β -cristobalite network of PCN-308 simulated based on the reported PCN-777 structure. The yellow sphere represents the void space.

PCN-308 is built from zirconium clusters and terpyridine-based tritopic ligand, 4'-(4-carboxyphenyl)-[2,2':6',2''-terpyridine]-5,5''-dicarboxylic acid (H_3TPY) (Figure II-4). PCN-308 is isostructural to PCN-777, a β -cristobalite network that requires six-connected D_{3d} nodes and trigonal-planar linkers to form super-tetrahedra in the zeotype framework.¹⁴⁹⁻¹⁵⁰ Although the three carboxylate groups in H_3TPY cannot stay in the same plane in the ligand precursor, it is possible for them to fit into the faces of the super-tetrahedra in the β -cristobalite network, because the three nitrogen atoms on the terpyridine center can reduce the rotating steric hindrance during MOF synthesis. As a result, PCN-308 could be obtained through one-pot solvothermal reaction between $ZrOCl_2 \cdot 8H_2O$ and H_3TPY under the topological guidance, showing an octahedra morphology (Figure II-5). Powder X-ray diffraction (PXRD) patterns demonstrated the isostructural nature of PCN-308 (Figure II-6). The corresponding structural model of PCN-308 was simulated based on

the reported PCN-777 structure by Material Studio 6.0.¹⁵¹ In PCN-308, the six-connected antiprismatic Zr_6 clusters adopt a D_{3d} -symmetry, alternately connected by six carboxylates groups of organic linkers and terminal OH/ H_2O moieties. The overall structure of PCN-308 is built by the assembly of super-tetrahedra cages in a staggered configuration, which are constructed from four Zr_6 units as vertexes linked by the trigonal planer organic linkers capping the faces. Finally, a mesoporous cage is formed with a diameter of 3.5 nm.

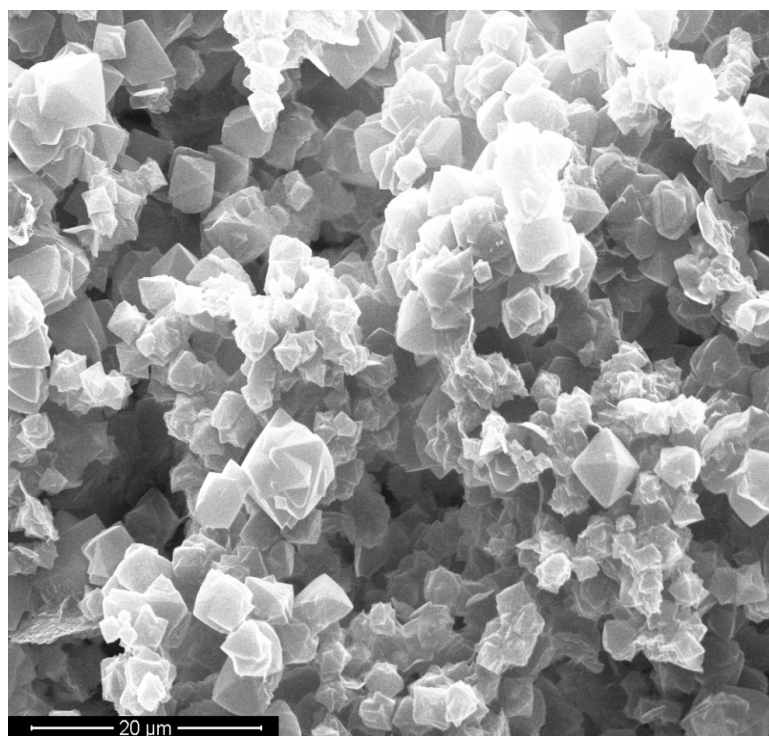


Figure II-5. SEM image of powder PCN-308.

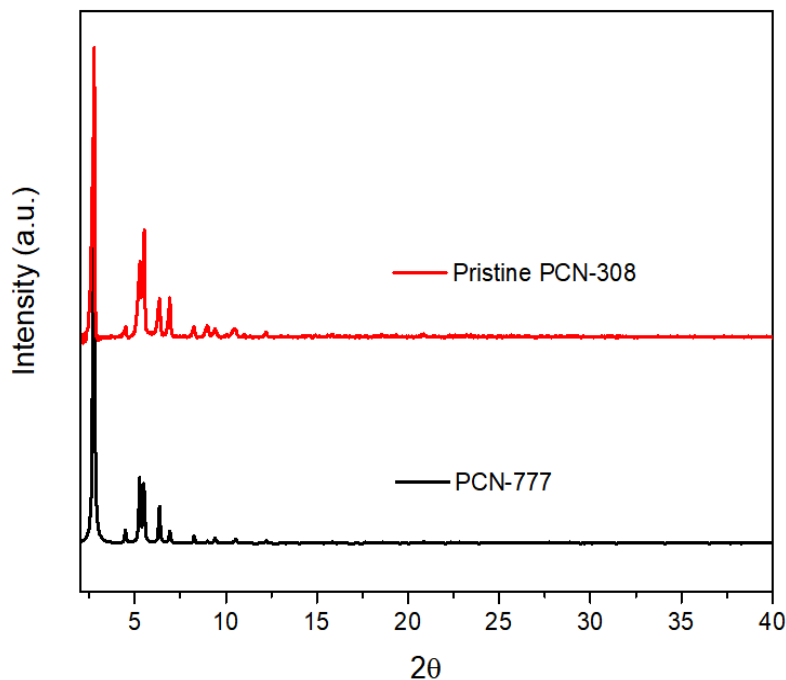


Figure II-6. PXRD comparison between as-synthesized PCN-308(red) and previously reported PCN-777 (black).

2.3.2 Porosity of PCN-308

PCN-308 was activated with supercritical CO₂ and the porosity was determined by N₂ adsorption at 77K. PCN-308 has a total N₂ uptake of 1525 cm³g⁻¹ at 1 bar. The experimental Brunauer–Emmett–Teller (BET) surface area is 1962 m²g⁻¹. A steep increase at P/P₀ = 0.4 on the adsorption branch of N₂ isotherm corresponded to the mesoporous cage of 3.5 nm in PCN-308. The pore volume is 2.85 cm³g⁻¹ (Figure II-7 & 8 and Table II-2).

2.3.3 Chemical and Thermal Stability Analysis of PCN-308

Facilitated by the strong interaction between the highly charged Zr₆ clusters and ligand carboxylates, PCN-308 maintained intact in aqueous solution. The almost unchanged PXRD

profile and N_2 isotherm of the sample after water treatment in comparison with those of the pristine PCN-308 indicated its excellent aqueous stability (Figure II-9 & 10). However, it failed to survive in more acid aqueous solutions. The moderate chemical stability might be ascribed to high hydrophilicity of the terpyridine-based backbones, which are succumbed to the attack of the proton. The thermal stability of PCN-308 was tested by thermal gravimetric analysis (TGA), showing that the decomposition temperature of PCN-308 is around 490 °C (Figure II-11).

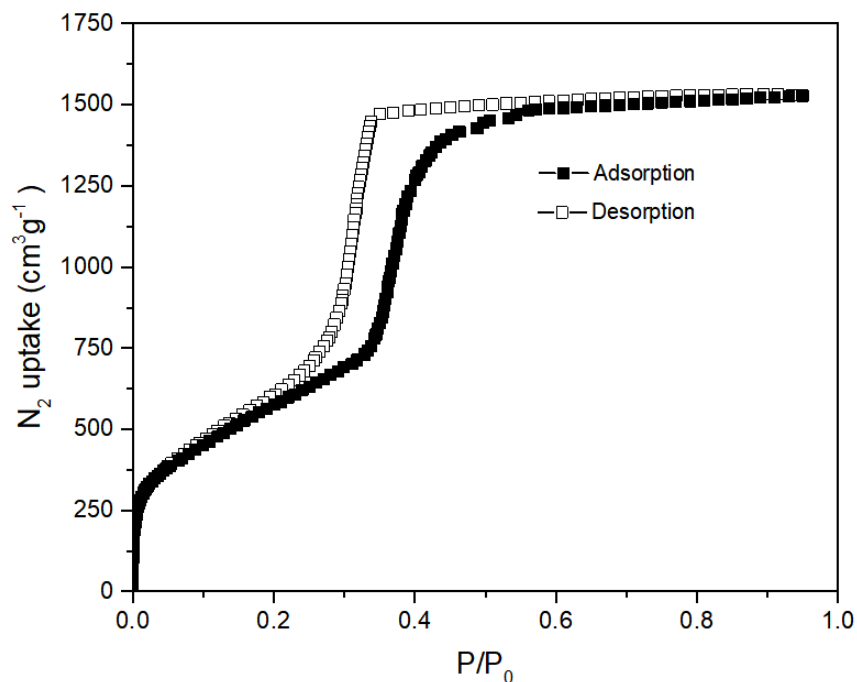


Figure II-7. N_2 sorption isotherm for PCN-308 at 77K, 1 atm.

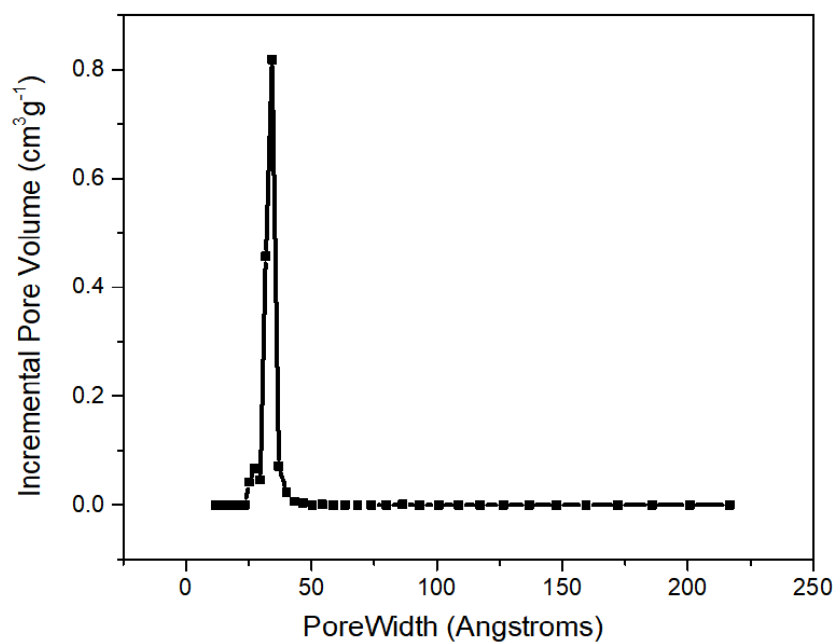


Figure II-8. DFT pore size distribution for PCN-308 derived by N₂ isotherm measured at 77 K, 1 atm.

Table II-2. Porosity comparison between PCN-777 and PCN-308

MOFs	N ₂ uptake (cm ³ g ⁻¹)	BET Surface Area (m ² g ⁻¹)	Pore Volume (cm ³ g ⁻¹)	Pore Size (nm)	Ref.
PCN-777	1450	2008	2.82	3.5	149
PCN-308	1525	1962	2.85	~3.5	This work

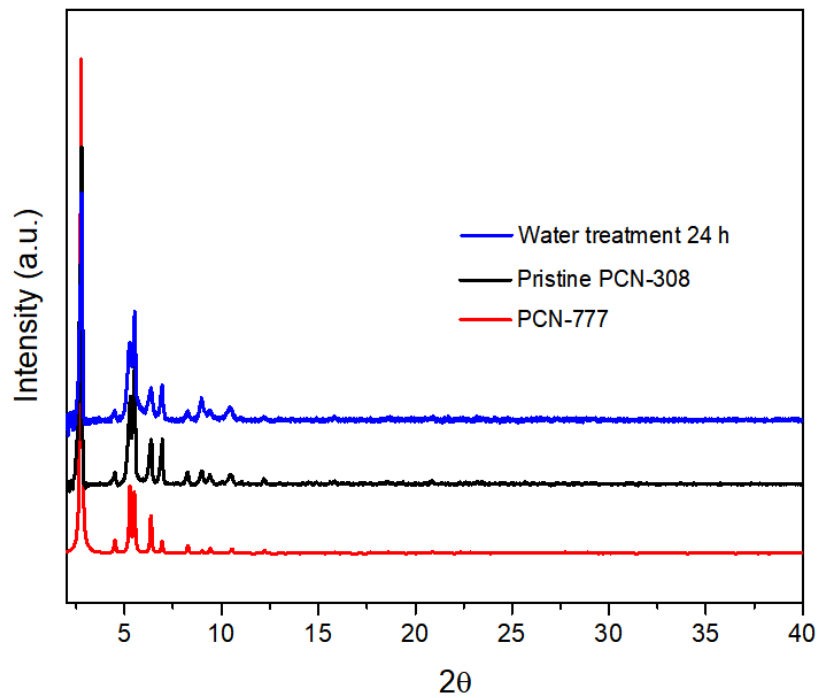


Figure II-9. PXRD patterns reported PCN-777 (red), pristine PCN-308 (black) and PCN-308 powder after water treatment for 24 hours.

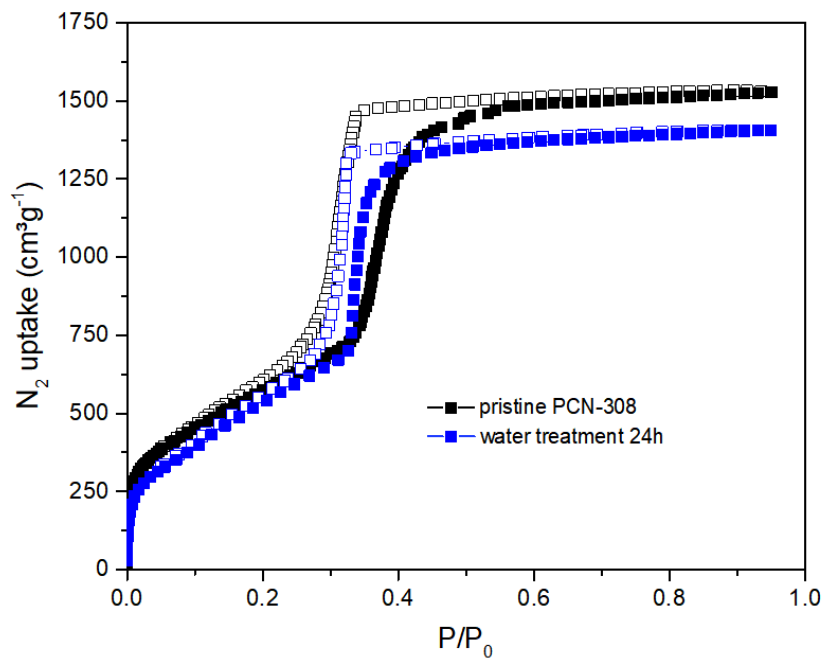


Figure II-10. N_2 isotherms of pristine PCN-308 and water-treated PCN-308 at 77 K, 1 atm.

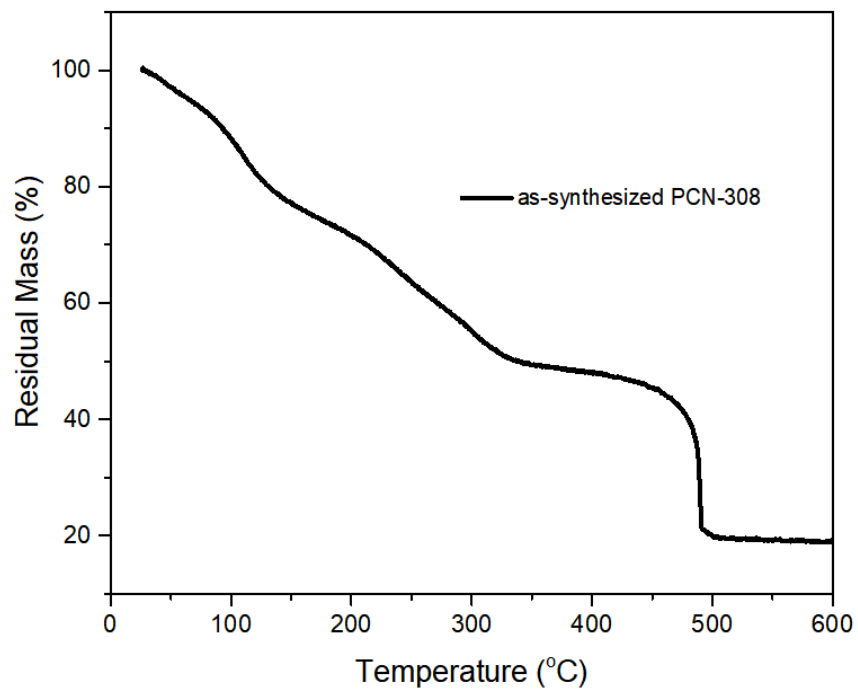


Figure II-11. Thermogravimetric analysis data of as-synthesized PCN-308. The decomposition temperature is around 490 °C based on calculation.

2.3.4 Post-synthetic Metalation of PCN-308

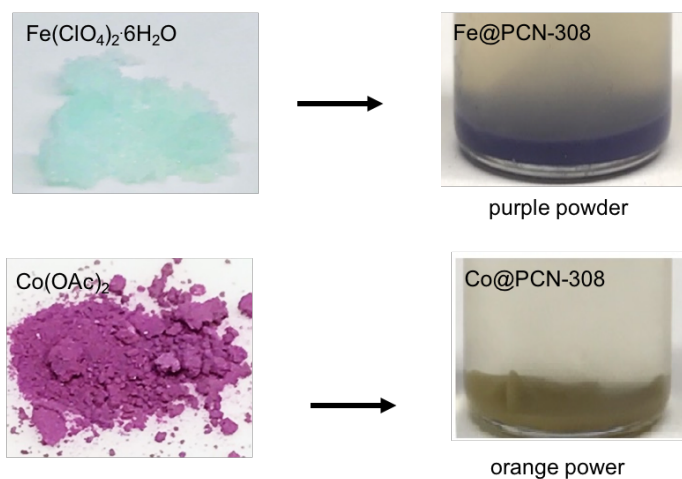


Figure II-12. Color changes of PCN-308 after post-synthetic metalation.

Fe@PCN-308 was prepared by treating the as-synthesized PCN-308 in an acetonitrile solution of $\text{Fe}(\text{ClO}_4)_2 \cdot 6\text{H}_2\text{O}$ (2.5 equiv.). After stirred at room temperature for three hours, the white powder turned to purple, demonstrating the formation of Fe-terpyridine complex. (Figure II-12). Scanning electron microscopy-energy dispersive X-ray spectroscopy (SEM-EDS) showed the even distribution of iron within the MOF and the experimental atomic ratio of Fe : Zr was 0.81 : 3 (1 : 3 in theory), giving an 81% loading of cobalt relative to the terpyridine linker (Figure II-13 & 14 and Table II-3) . The metalation yield was further tested by Inductively Coupled Plasma-Optical Emission spectrometry (ICP-OES), which showed a similar 79 % loading rate of the digested Fe@PCN-308. X-ray photoelectron spectroscopy (XPS) spectrum showed no satellite features of Fe element, indicating the low oxidation state as well as low-spin nature of Fe(II) complexing with terpyridine (Figure II-15).

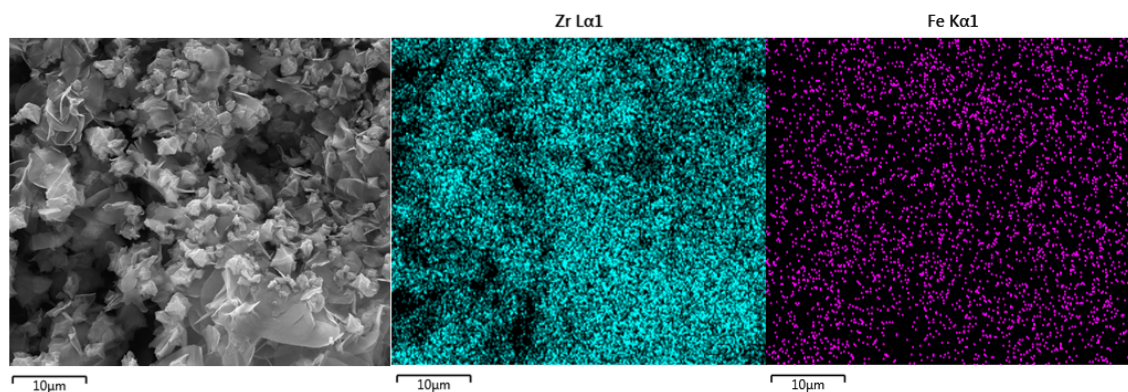


Figure II-13. Representative SEM image of Fe@PCN-308 powder and corresponding EDS-mapping of Zr and Fe from left to right.

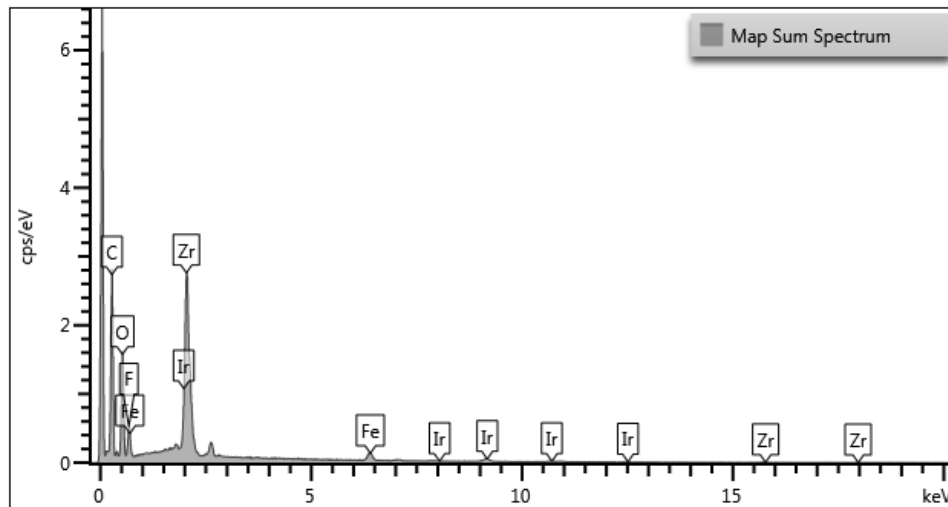


Figure II-14. SEM-EDS analysis of Fe@PCN-308.

Table II-3. Atomic ratio of Fe@PCN-308

	Trial 1	Trial 2	Trial 3
Element	Weight%	Weight%	Weight%
Fe	3.08	3.01	3.44
Zr	19.47	18.53	20.07
Average atomic Fe: Zr ratio: 0.268 : 1 (80.6%)			

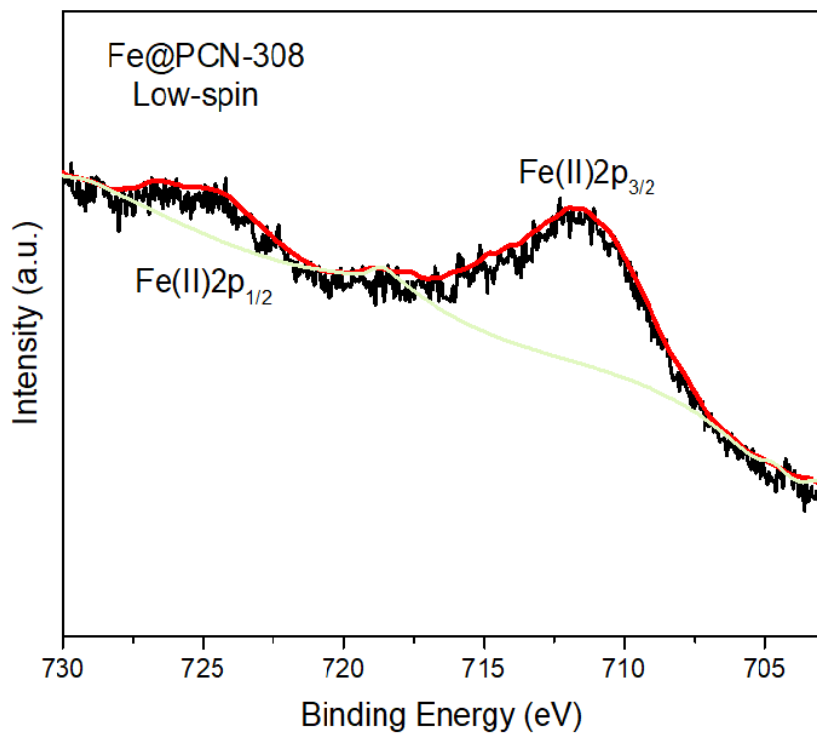


Figure II-15. XPS spectrum of Fe@PCN-308.

Similarly, post-synthetic metalation (PSM) of PCN-308 with 2.5 equiv. of $\text{Co}(\text{OAc})_2$ in toluene afforded Co@PCN-308 as orange solid (Figure II-12). SEM-EDS revealed an 82% loading rate of Co relative to linker, which also matched with the one gave by ICP-OES (84 %) (Figure II-16 & 17 and Table II-4). XPS spectrum displayed typical satellite features of Co(II) (Figure II-18).

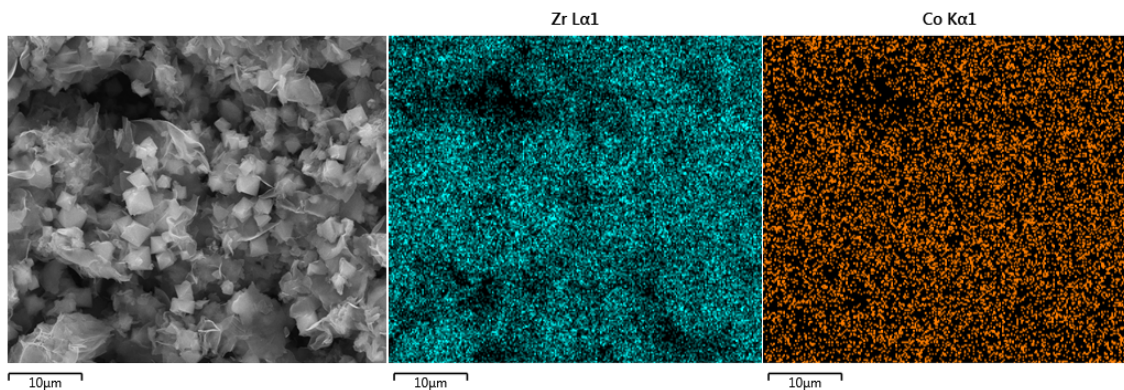


Figure II-16. Representative SEM image of Co@PCN-308 powder and corresponding EDS-mapping of Zr and Co from left to right.

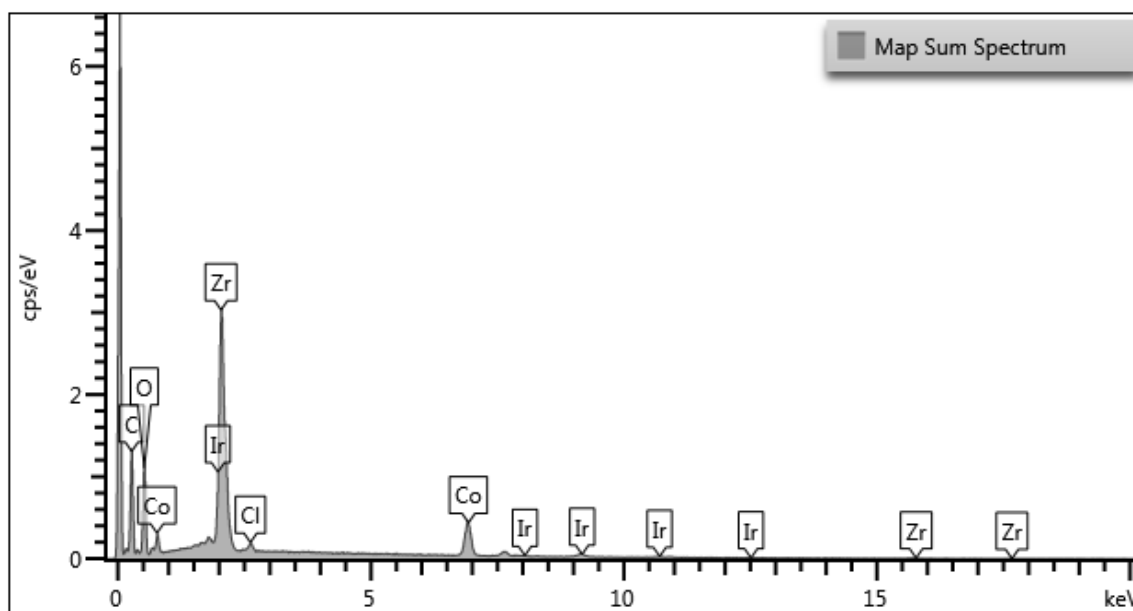


Figure II-17. SEM-EDS analysis of Co@PCN-308.

Table II-4. Atomic ratio of Co@PCN-308

	Trial 1	Trial 2	Trial 3
Element	Weight%	Weight%	Weight%
Co	4.27	4.17	4.83
Zr	23.68	23.59	25.44
Average atomic Co : Zr ratio: 0.273 : 1 (81.9 %)			

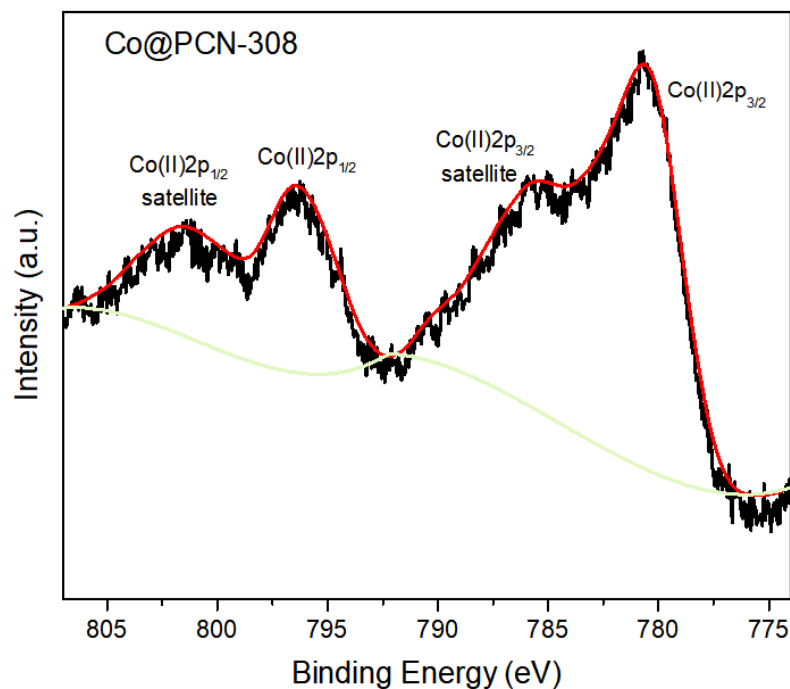


Figure II-18. XPS spectrum of Fe@PCN-308.

The structural integrity of the metalated samples were further confirmed by the PXRD analysis, where the PXRD profiles stayed almost intact compared with that of the pristine PCN-308. Moreover, owing to the presence of the coordinated metal centers and counterions, N₂ isotherm measurements also showed reasonable reductions in BET surface areas, 1244 m²g⁻¹ and 1209 m²g⁻¹ for Fe@PCN-308 and Co@PCN-308, respectively (Figure II-19 & 20).

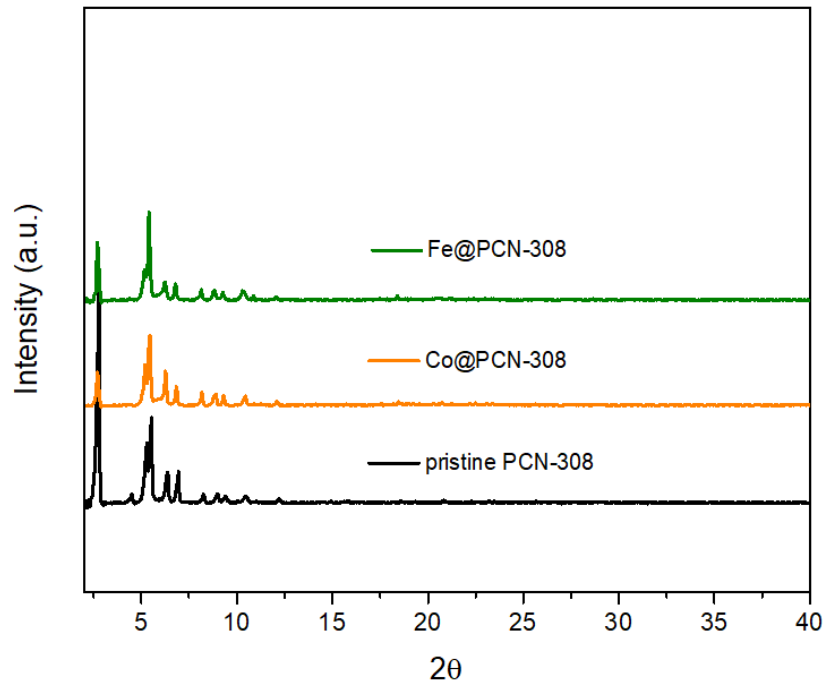


Figure II-19. PXRD patterns of PCN-308 after post-metalation.

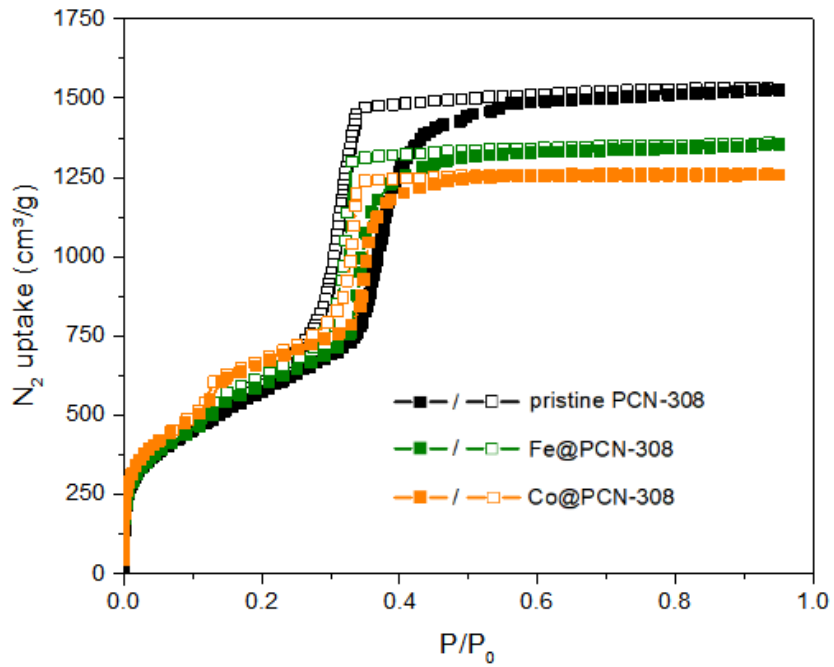
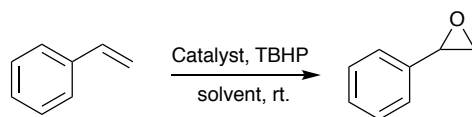


Figure II-20. N₂ isotherms of PCN-308 after post-metalation.

2.3.5 Catalytic Performance of Metalated PCN-308

With redox-active metal centers on the struts, Fe@PCN-308 was examined as a self-supporting catalyst for epoxidation of olefins. At the outset, styrene was chosen as a model substrate to optimize the reaction conditions. Screening reactions were carried out and showed that 1.0 mol% of Fe@PCN-308 could catalyse the epoxidation of styrene in excellent yield with 1.5 equiv. of tert-butyl hydroperoxide (TBHP) as oxidant and toluene as solvent at room temperature (Table II-5, entry 3). A control experiment was performed without catalyst and it gave merely 12% yield of the product, which were likely caused by the oxidation of TBHP (Table II-5, entry 1). The addition of non-metalated PCN-308 in the solution similarly generated low yield of product (12%), excluding the influence of the Lewis acidity of the metal clusters on the reaction (Table II-5, entry 8). The recyclability of Fe@PCN-308 was also tested. The MOFs separated from the reaction could be reused four more times without loss of catalytic activity. The PXRD patterns of the samples recovered from each recycle showed no essential change in the profiles from the pristine ones, suggesting the intact crystallinity of the MOFs under the catalytic conditions (Figure 21 & 22).

Table II-5. Screening experiments of styrene epoxidation.



Entry	Catalyst (mol %)	Solvent	Time (h)	%Yield
1	none	toluene	6	9
2	Fe@PCN-308 (0.5)	toluene	6	80
3	Fe@PCN-308 (1.0)	toluene	6	92
4	Fe@PCN-308 (1.5)	toluene	6	90
5	Fe@PCN-308 (1.0)	toluene	12	91
6	Fe@PCN-308 (1.0)	CH ₃ CN	6	87
7	Fe@PCN-308 (1.0)	MeOH	6	<1
8	PCN-308 (1.0)	toluene	6	12
9	Co@PCN-308 (1.0)	toluene	6	—

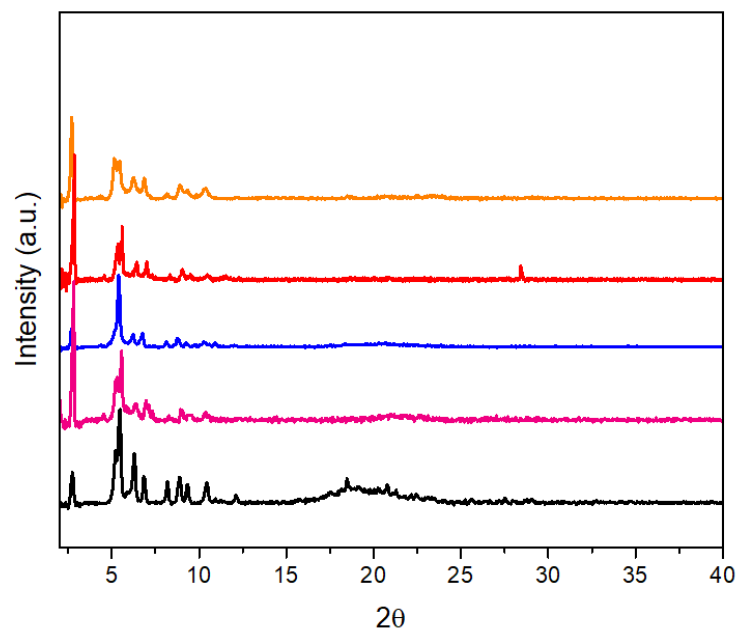


Figure II-21. PXRD patterns of recycled Fe@PCN-308 (1st run, black; 2nd run, pink; 3rd run, blue; 4th run, red; 5th run, orange).

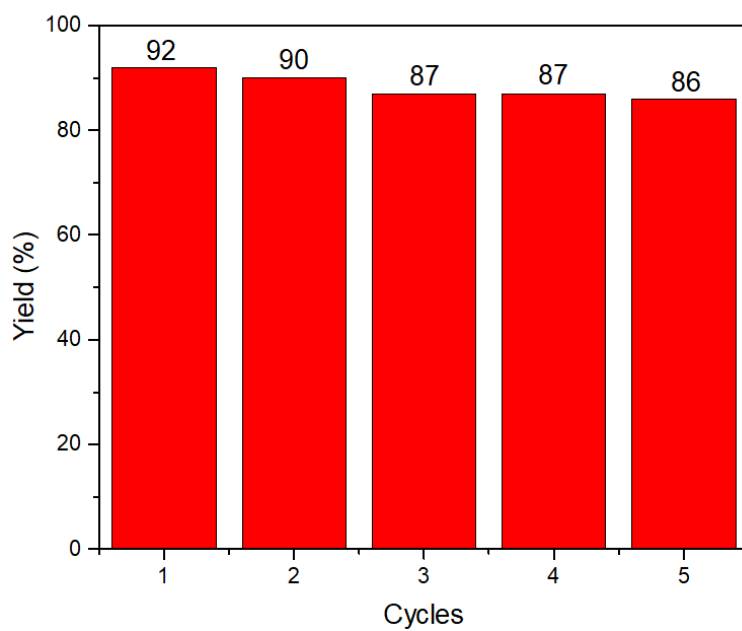


Figure II-22. Recycling catalytic performance of Fe@PCN-308 in epoxidation of styrene.

Table II-6. Summary of catalysis results of reported MOFs in epoxidation of styrene.

Entry	Catalyst	Temp.(°C)	Time (h)	Yields (%)	Ref.
1	PCN-222(Fe)@Zr- BPDC	rt.	24	87	152
2	PCN-222	rt.	24	96	152
3	[Co(Hoba) ₂ (H ₂ O) ₂]	75	6	96	153
4	Cu-MOF-2	40	6	58	154
5	Cr-MIL-101-NH ₂	35	3	92	155
6	MnFe-MOF-74	0	3	100	156
7	Fe@PCN-308	rt.	6	97	This work

The universal capability of Fe@PCN-308 was further examined with various olefins under the optimal conditions and the results were summarized in Table II-7. All the olefins were converted to the corresponding epoxides in satisfactory yields with negligible byproducts. The efficient catalytic performance was ascribed to the high loading of the reactive catalytic centers as well as the mesoporous nature of the MOF structure, which guarantees the accessibility of the catalytic centers to the substrates. However, due to the relatively small apertures of the pores in the MOF, the steric hindrance of the substrates exerted a considerable effect on the epoxidation reactions. Olefins with small molecular size gave nearly quantitative yields of the products within 6 hours; while it took more reaction time for the large ones to transfer to the corresponding epoxides to react completely. To be specific, in comparison with entry 6 and 8, the extra phenyl group in the stilbene remarkably impeded the reaction process, causing a 27 % decrease in yield

even with longer reaction time. In addition, trans-stilbene gave a lower yield than its cis-isomer due to the steric effect. On the other hand, electronic effect of the olefins synergistically influences the epoxidation reaction, which could be demonstrated by the dramatic decrease in the yield of substrate 10.

On the other hand, the cobalt-metalated PCN-308 turned out to be a superior air-stable catalyst in C-H borylation of arenes, an important reaction that produces versatile aryl boronate esters in organic synthesis.¹⁵⁷ With $B_2(\text{pin})_2$ (pin = pinacolate) as the borylating agent, a broad range of arenes were investigated for the borylation reaction. Generally, the reactions were performed in sealed vials charged with reagents under the protection of N_2 . LiOMe was added as an indispensable additive to accelerate the reaction.¹³⁶ With the addition of $B_2(\text{Pin})_2$, the color of the reaction mixtures immediately changed from orange to deep purple, diagnosing the activation of the catalyst. The reactions were terminated by exposure to the air and the resulted products were tested by GC analysis to give conversions and yields. As it was shown in the Table II-8, 5 mol % of Co@PCN-308 revealed the highest yields in neat arenes at 100 °C for 48 h. Both benzene and toluene gave monoborylated products under the standard conditions, while for the latter, the borylation happened on both meta- and para- positions, giving the corresponding products in a 70 : 30 ratio (entry 1 & 2). The heterogenous catalyst was also active in borylating bulky arenes. Regioselectivity of the reaction favored the positions with less steric hindrance, which are analogous to those of the reported homogeneous systems (entry 3 & 4).⁷⁴ Heteroarenes, indole for example, could also be efficiently transferred into the borylated product in the yield of 88 % (entry 5).

Table II-7. Epoxidation of selected olefins.

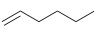

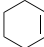

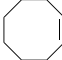
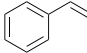
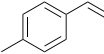
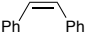
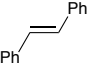
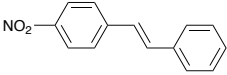
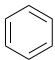
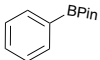
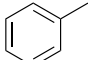
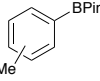
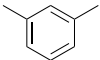
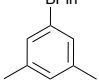
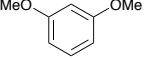
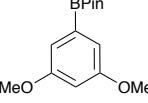
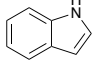
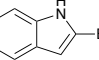
Entry	Substrate	Time (h)	%Conversions
1		6	>99
2		6	>99
3		6	>99
4		6	>99
5		6	98
6		6	97
7		6	95
8		12	70
9		12	61
10		24	49

Table II-8. Borylation of neat arenes.

Entry	Substrate	Product	%Conversion	%Yield
1			98	83
2			98	78 <i>o:m:p</i> 0:70:30
3			92	72
4			83	65
5			88	73

Control experiments with non-metalated PCN-308 as catalyst showed no activity in the borylation transformation. The borylated products could also be obtained by the homogeneous catalytic counterpart, $[(\text{CO}_2\text{Me})_3\text{tpyCo}(\text{OAc})_2]$, under the same conditions. However, the yields were much lower, demonstrating the necessity of active site isolation in the MOF struts (Table II-1). Co@PCN-308 can be easily separated and recovered from the reaction system by filtration. Its structural integrity was evaluated by the PXRD patterns, which deviated slightly from that of the

as-synthesized PCN-308. The catalyst could also be reused for at least three cycles without remarkable loss of catalytic activity (Figure 24 & 25).

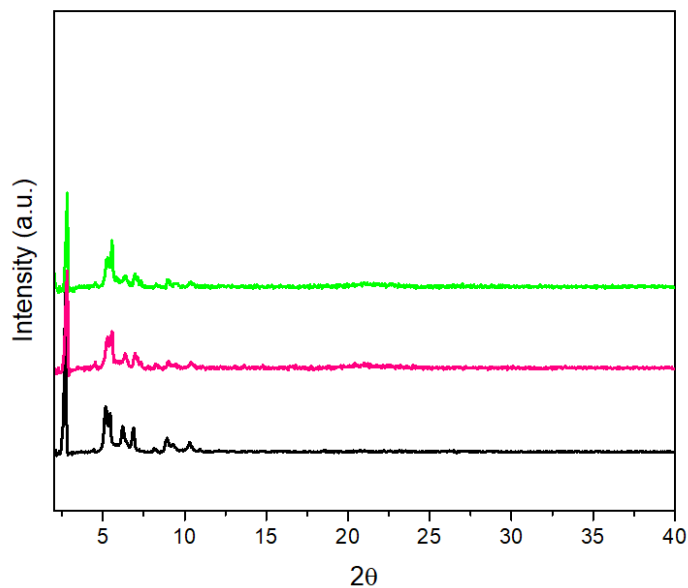


Figure II-23. PXRD patterns of recycled Fe@PCN-308 (1st run, green; 2nd run blue; 3rd run, purple).

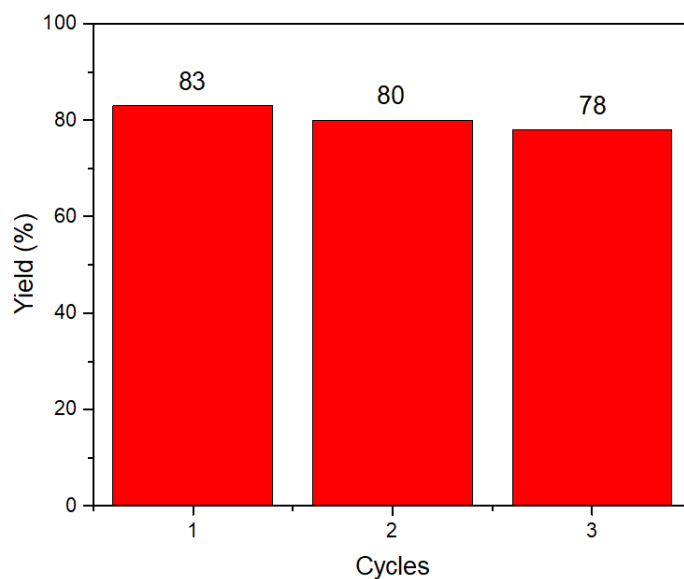
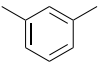
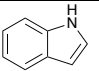
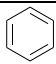
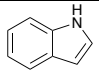
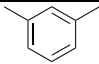
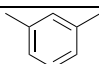


Figure II-24. Recycling catalytic performance of Co@PCN-308 in borylation of benzene.

Table II-9. Summary of catalysis results of reported MOFs in borylation of neat arenes

Entry	Substrate	Catalyst	Temp.(°C)	Time (h)	Yields (%)	Ref.
1		mBPV-MOF-Ir mPT-MOF-Ir	115	16 h 32 h	97 96	¹³⁰
2		Bpy-UiO-Ir	100	7 h	94	⁷⁵
3		P1-MOF-Ir	90	40 h	84	¹⁵⁸
4		mPT-MOF-Co	100	4.5	76	⁷⁴
5		CoCl ₂ ·TPY- MOL	100	3	95	¹⁴³
6		Co@PCN-308	100	2	92	This work

2.4 Conclusion

In summary, a tritopic terpyridine-based linker (H_3TPY) was judiciously designed and utilized to construct a mesoporous MOF, PCN-308, with predictable β -cristobalite topology. Due to the direct one-pot synthesis, the terpyridine-based chelating sites were evenly distributed on the scaffold, which could be easily accessed by post-synthetic metalation of redox-active metal ions under mild conditions. The scaffolded MOF materials, Fe@PCN-308 and Co@PCN-308, contained high loadings of catalytic centers and turned out to be efficient catalysts for alkene epoxidation and arene borylation, respectively. The work exemplified the introduction of terpyridine-based pincer complexes into 3D mesoporous MOF structure, providing a successfully approach to utilize MOF scaffold in preparing pincer-type heterogeneous catalysts.

CHAPTER III

PYRENE-BASED MOFS AS VISIBLE-LIGHT HARVESTING ROS GENERATORS

3.1 Introduction

Reactive oxygen species (ROS) are highly active molecules that are commonly formed by normal metabolism of oxygen in aerobic life.¹⁵⁹⁻¹⁶⁰ With their superior oxidative abilities, ROS are of great potential in various applications, such as industrial wastewater treatment, photochemical synthesis and photodynamic therapy (PDT).¹⁶¹⁻¹⁶⁴ So far, efforts have been devoted to explore artificial chemical systems to produce ROS in an environmentally benign condition. The biomimicking process usually requires a photosensitizer (PS) or a photosensitizing agent, which can harvest solar energy and then generates ROS via energy transfer and/or electron transfer.¹⁶⁵ In particular, organic dyes, transition metal complexes and so on have been extensively studied as photosensitizers to create ROS for organic transformations.¹⁶⁶⁻¹⁷⁰ However, most of photosensitizers suffer from aggregation and self-quenching at high concentrations, which undoubtedly hampers their performance in solar-energy conversion.¹⁷¹

Metal-organic frameworks (MOFs), also known as porous coordination polymers (PCPs), are an emerging class of crystalline porous materials that are assembled by inorganic secondary building units (SBUs) and organic linkers via coordination bonds.¹⁷²⁻¹⁷³ Owing to their intrinsic porosity and infinite tunability, MOFs have shown a vast and ever-expanding array of applications, including gas storage, separation, heterogeneous catalysis, chemical sensing, drug delivery, and proton conduction.^{15-18, 20, 120, 173-177} More recently, MOFs have been exploited as a unique platform to integrate photosensitizers for light harvesting and photocatalysts.¹⁷⁸⁻¹⁸³ In term of light-driven ROS generation, many MOF-based systems employ predesigned organic and metal-organic

chromophores as linkers to impart MOFs with photoactivities.¹⁸⁴⁻¹⁸⁶ The confinement and isolation effect of the frameworks prevent the undesired aggregation-caused quenching of the photosensitizers, reducing the non-productive decay process in the excited state. Meanwhile, the intrinsic organic-inorganic hybrid structure endows MOFs with semiconductor-like behavior upon light irradiation, allowing variant photosensitizing processes in ROS formation.¹⁸⁷⁻¹⁸⁹

Of various photochromic compounds, pyrene and its derivatives with the four-ring-fused planar electron-enriched skeleton are well-known for their unique optical and photoelectronic properties.¹⁹⁰ They have been demonstrated to possess a low energy triplet state as well as significant O₂-induced enhanced intersystem crossing (EISC), which are favorable to generate ROS through energy transfer, especially singlet oxygen (¹O₂).¹⁹¹⁻¹⁹³ Several pyrene-based MOFs have been investigated for ¹O₂ generation.¹⁹⁴⁻¹⁹⁵ However, as the absorption bands of the reported materials mainly reside in the UV region, they exhibit inferior performance under visible light. Therefore, the development of a MOF-based system that can merge the merits of pyrene to produce ¹O₂, while still take advantage of visible light, stays urgent.

With these considerations in mind, we synthesized two visible light responsive MOFs, PCN-822(Zr/Hf), consist of a judiciously designed pyrene-based ligand, 4,4',4'',4'''-((2,7-di-tert-butylpyrene-4,5,9,10-tetrayl)tetrakis(ethyne-2,1-diyl))-tetrabenzoic acid (H₄BPETB). Solvothermal reactions between the organic linker and Zr₆/Hf₆ clusters afforded PCN-822(Zr/Hf) with a (4,8)-connected **sqc** topology. Due to the well-isolated pyrene chromophores in the framework, the MOFs inherited the visible-light absorption of H₄BPETB and simultaneously, showed improved efficiency in singlet oxygen generation. PCN-822(Hf) was also used as a photosensitizer for aerobic photooxidation of amines to imines. The heavy Hf⁴⁺ clusters enhanced the intersystem crossing (ISC) in the material, promoting the generation of singlet oxygen. While

the photo-induced charge separation was also observed, facilitating the $O_2^{\bullet-}$ production. Combining the energy and charge transfer, the material exhibited excellent photocatalytic activity in transferring amines to imines.

3.2 Experimental Section

3.2.1 Materials and Instrumentation

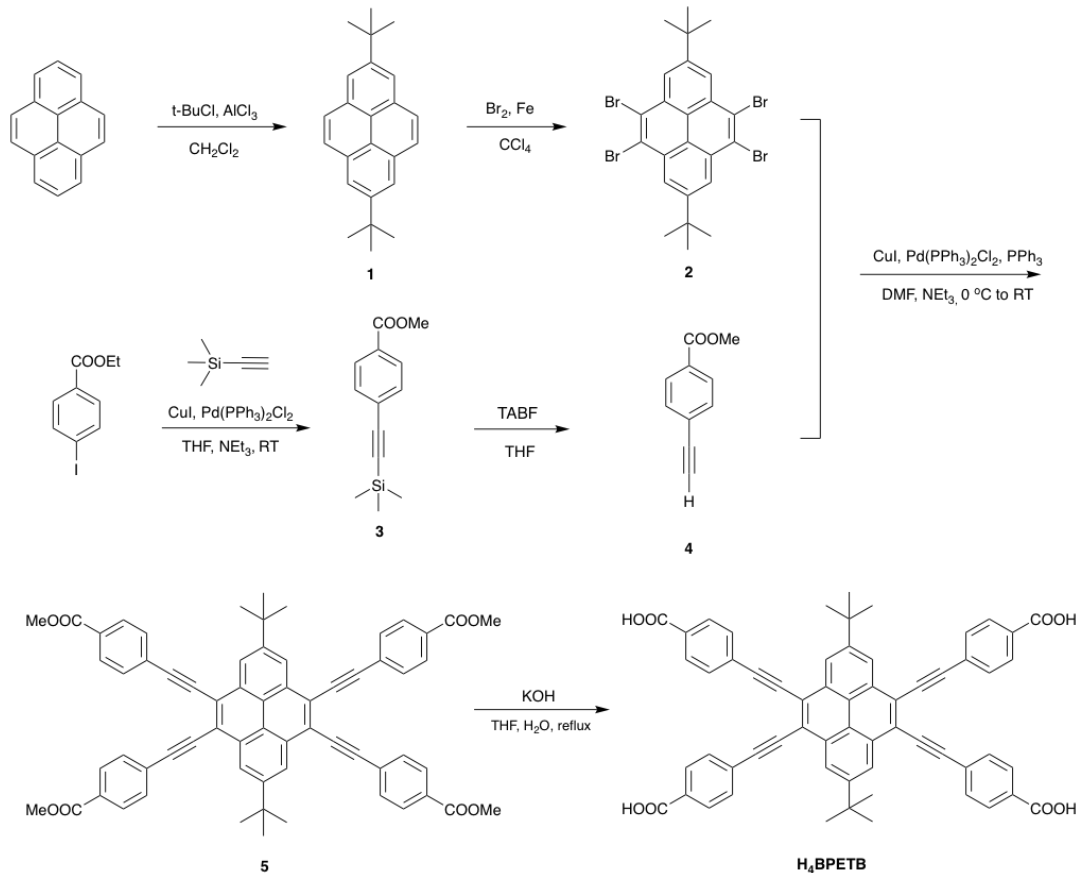
Materials

All commercially available reagents and solvents were purchased from either VWR or Sigma Aldrich. Unless otherwise noted, they were used without further purification.

Instrumentation

Powder X-ray diffraction (PXRD) was carried out on a Bruker D8-Focus Bragg-Brentano X-ray powder diffractometer equipped with a Cu microfocus tube ($\lambda = 1.54178 \text{ \AA}$) at 40 kV and 40 mA. Single crystal X-ray diffraction experiments were carried out on a Bruker D8-Venture diffractometer equipped with a Mo microfocus tube ($\lambda = 0.72768 \text{ \AA}$). Fourier transform infrared (FT-IR) spectra were recorded on an IR Affinity-1 instrument. Thermogravimetric analysis (TGA) were carried out on a Shimadzu TGA-50 thermogravimetric analyzer from temperature to 600 °C at a ramp rate of 5 °C /min in a flowing air atmosphere. Nuclear magnetic resonance (NMR) data were collected on a Mercury 500 spectrometer. The electronic absorption spectra were recorded on were measured on a Hitachi U-4100 UV-Vis-NIR spectrometer. Fluorescence spectra were collected on Horiba Fluorolog spectrofluorometer. Electron paramagnetic resonance (EPR) was measured on a X-Band Bruker EMS spectrometer with an Oxford ESR900 liquid Helium cryostat.

3.2.2 Ligand Synthesis



Scheme III-1. Synthesis of H_4BPETB .

Step 1. Synthesis of 2,7-di-tert-butylpyrene (**1**)

In a 500 mL three-necked round-bottom flask, pyrene (10.1 g, 50 mmol) and AlCl_3 (0.6 g, 4.5 mmol) were added into 200 mL anhydrous CH_2Cl_2 . Then tert-butyl chloride (10.2 g diluted in 75 mL CH_2Cl_2) was added into the solution drop by drop at $0\text{ }^\circ\text{C}$ under N_2 . The mixture was then allowed to react at room temperature for 6 h. After that, iced water with 25 mL HCl was poured into the mixture and the organic phase was washed with water three times and separated. The solvent was pumped out and the resulted solids were further purified by chromatography with

hexane as eluent to give pure white solid (14.6 g, 46.4 mmol, 93%). ^1H NMR (500 MHz, CDCl_3) δ 8.19 (s, 4H), 8.03 (s, 4H), 1.59 (s, 18H).

Step 2. Synthesis of 2,7-di-tert-butyl-4,5,9,10-tetrabromopyrene (2)

In a 500 mL round-bottom flask, **1** (4.0 g, 12.7 mmol) and iron powder (4.0 g) was added in 150 mL CCl_4 . Liquid bromine (12.4 g, 78 mmol) in 40 mL CCl_4 was then added dropwise into the mixture. The reaction mixture was then allowed to react for 4 h at room temperature. After that, 100 mL saturated aqueous $\text{Na}_2\text{S}_2\text{O}_3$ solution was poured into the system and the mixture was stirred for another couples of hours until the color turned to pale pink. The organic layer was then separated and washed with water three times. The solvent was removed under vacuum and the obtained solid was further recrystallized in benzene to afford white product (5.6 g, 8.9 mmol, 70%). ^1H NMR (500 MHz, CDCl_3) δ 8.87 (s, 4H), 1.63 (s, 18H).

Step 3. Synthesis of methyl 4-((trimethylsilyl)ethynyl)benzoate (3)

Ethyl-4-iodobenzoate (13.5 g, 50 mmol), $\text{Pd}(\text{PPh}_3)_2\text{Cl}_2$ (1.5 g, 2.1 mmol) and CuI (290 mg, 1.5 mmol) were added in a 500 mL three-necked round bottle flask. The flask was fitted on a schlenk line followed by vacuumed and refilled with N_2 three times. A mixture of $\text{Et}_3\text{N}/\text{THF}$ (v/v = 150 mL/150 mL) was bubbled with N_2 for 30 min and then transferred to the flask through a canula. Trimethylsilyl acetylene (8.5 mL, 60 mmol) was then added into the system by syringe. The reaction mixture was then stirred at room temperature under the protection of N_2 for 5 h. After that, the solvent was removed under vacuum and the crude product was purified by a short column (eluent: $\text{EtOAc}/\text{hexane} = 1/6$) to give dark yellow solid (10.5 g, 42.5 mmol, 85 %). ^1H NMR (500 MHz, CDCl_3) δ 7.95 (d, $J = 8.1$ Hz, 2H), 7.49 (d, $J = 8.0$ Hz, 2H), 3.93 (s, 3H), 0.24 (s, 9H).

Step 4. Synthesis of methyl 4-ethynylbenzoate (4)

In a 500 mL round-bottom flask, 3 (10.0 g, 40 mmol) was dissolved in 200 mL THF followed by addition of 40 mL tetrabutylammonium fluoride solution (TBAF, 1.0 M in THF). The reaction mixture was then stirred at room temperature for 15 min. The solvent was removed and the crude product was purified by a short column (eluent: EtOAc/hexane = 1/5) to give light yellow solid (6.26 g, 36 mmol, 90%). ¹H NMR (500 MHz, CDCl₃) δ 8.00 (d, *J* = 8.7 Hz, 2H), 7.56 (d, *J* = 8.5 Hz, 2H), 3.93 (s, 3H), 3.23 (s, 1H).

Step 5. Synthesis of tetramethyl 4,4',4'',4'''-((2,7-di-tert-butylpyrene-4,5,9,10-tetrayl)tetrakis(ethyne-2,1-diyl))tetrabenzoate (Me₄BPETB).

2 (400 mg, 0.64 mmol), Pd(PPh₃)₂Cl₂ (90 mg, 0.13 mmol), CuI (24.4 mg, 0.13 mmol) and PPh₃ (67.2 mg, 0.26 mmol) were added in a 250 mL three-necked round bottle flask fitted on a Schlenk line. The flask was vacuumed and refilled with N₂ three times and a mixture of DMF/THF (v/v = 60 mL/60 mL) was transferred to the flask through a canula after bubbled with N₂ for 30 min. The reaction mixture was stirred for 30 min at 0 °C under N₂ and 4 (891 mg, 5.12 mmol) was added by a syringe. The mixture was then heated up to 100 °C and allowed to react for another 48 h. After cooling to room temperature, the mixture was poured into a large amount of water and extracted with CHCl₃ three times. The organic phase was collected and washed with saturated aqueous NH₄Cl, H₂O and brine successively. The organic layer was then dried with MgSO₄ and the organic solvent was removed under vacuum. The crude product was then purified by a short column (eluent: from hexane/chloroform = 2/1 to pure chloroform). The obtained solid was further washed with methanol to afford yellow solid (400 mg, 0.456 mmol, 71 %). ¹H NMR (500

MHz, CDCl₃) δ 8.91 (s, 4H), 8.15 (d, J = 7.3 Hz, 8H), 7.83 (d, J = 7.1 Hz, 8H), 3.99 (s, 12H), 1.70 (s, 18H).

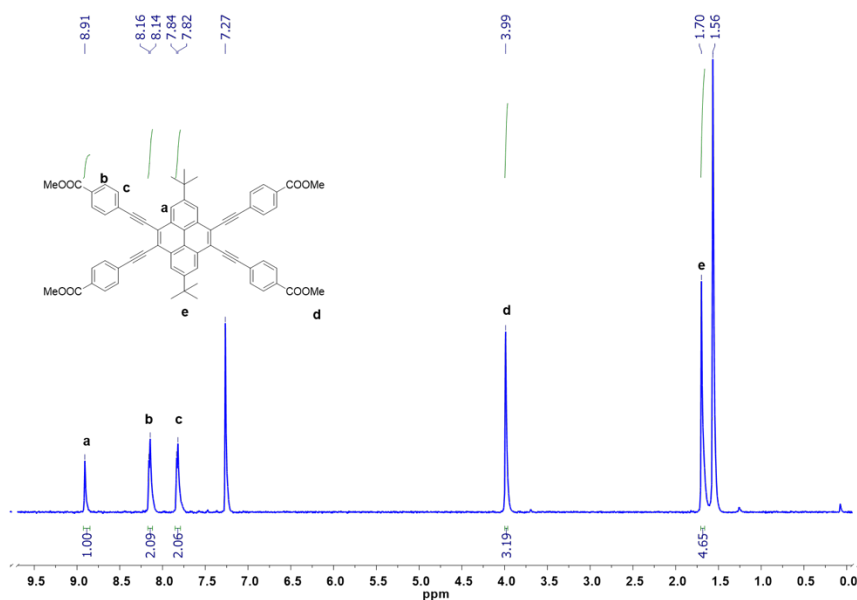


Figure III-1. ¹H NMR spectrum of H₄BPETB.

Step 6. Synthesis of 4,4',4'',4'''-((2,7-di-tert-butylpyrene-4,5,9,10-tetrayl)tetrakis(ethyne-2,1-diyl))-tetrabenzoic acid (H₄BPETB)

5 (400 g, 0.46 mmol) and potassium hydroxide (2.4 g, 43.7 mmol) were added into a mixture of THF/water (v/v = 50 mL/50mL) and was refluxed overnight. After cooling, the organic solvent was removed and the aqueous phase was acidified with 6 M hydrochloric acid to give yellow precipitate, which was then washed with water several times and dried under vacuum (354

mg, 0.4 mmol, 90%). Due to its low solubility in common deuterium-solvents, the product was used directly to synthesize MOF without further characterization.

3.2.3 Synthesis of PCN-822

PCN-822(Zr)

In a 4 mL Pyrex vial, ZrCl₄ (10 mg, 0.043 mmol), H₄BPETB (5mg, 0.006 mmol) and 290µL trifluoroacetic acid (TFA) were ultrasonically dissolved in 2 mL N, N-dimethylformamide (DMF). The mixture was then heated in a 120 °C oven for 4 days to afford yellow crystals (Yield: 3mg).

PCN-822(Hf)

In a 4 mL Pyrex vial, HfCl₄ (10 mg, 0.032), H₄BPETB (5 mg, 0.006 mmol) and 280 µL trifluoroacetic acid (TFA) were ultrasonically dissolved in 2 mL N, N-dimethylformamide (DMF). The mixture was then heated in a 120 °C oven for 4 days to afford yellow crystals (Yield: 3 mg)

3.2.4 Single Crystal X-ray Crystallography

The single-crystal was taken from the mother liquid without further treatment, transferred to oil and mounted into a loop for single crystal X-ray data collection. Diffraction was measured on a Bruker D8 Venture or D8 Quest diffractometer equipped with a Cu-K α sealed-tube X-ray source ($\lambda = 1.54184 \text{ \AA}$, graphite monochromated) at low temperature device (100 K). The data frames were recorded using the program APEX3 and processed using the program *SAINTE* routine within APEX3. The data were corrected for absorption and beam corrections based on the multi-scan technique as implemented in *SADABS*. The structures were solved by direct methods using *SHELXS* and refined by full-matrix least-squares on F^2 using *SHELXL* software.¹⁹⁶

3.2.5 Procedure of photooxidation of 1,5-Dihydroxynaphthalene (DHN)

In a 20 vial, 1,5-Dihydroxynaphthalene (DHN) (4.8 mg, 0.03 mmol) and MOF powder (-2mg) was added into 10 mL acetonitrile. The mixture was bubbled with oxygen for 20 min and then stirred at room temperature upon a xenon lamp. UV-vis absorption spectra were recorded at an interval of one hour until the absorption at 301 nm decreased to the lowest point (The consumption of DHN). A blank reaction was carried out without addition of MOF.

3.2.6 Procedure for Oxidation of Various Amines

In a 4 mL Pyrex vial was added amines (0.1 mmol) and powder PCN-822 (1 mmol %). The vial was capped with a septum stopper and 2.0 mL solution was added with a syringe. The mixture was then bubbled with O₂ for 30 min and stirred under an oxygen atmosphere (1 atm) at room temperature for another 12 h upon the irradiation of a xenon lamp. Afterwards, the solid was removed by filtration and washed with dichloromethane twice. The filtrate was collected and the organic solvent was then removed under vacuum to afford residual for ¹H NMR characterization.

3.2.7 Electronic Properties

The cyclic voltammetry measurements were done with Electrochemical Analyzer from CH Instruments, inc. Platinum electrodes were used as working and counter electrodes. Ag/AgCl electrode was used as reference. The cyclic voltammograms were recorded in 0.1 M n-Bu₄NPF₆ solution/CH₂Cl₂ under N₂ atmosphere. All solvent used was pre-dried and degassed before use.

3.3 Results and Discussion

3.3.1 Ligand Design and Structural Description of PCN-822

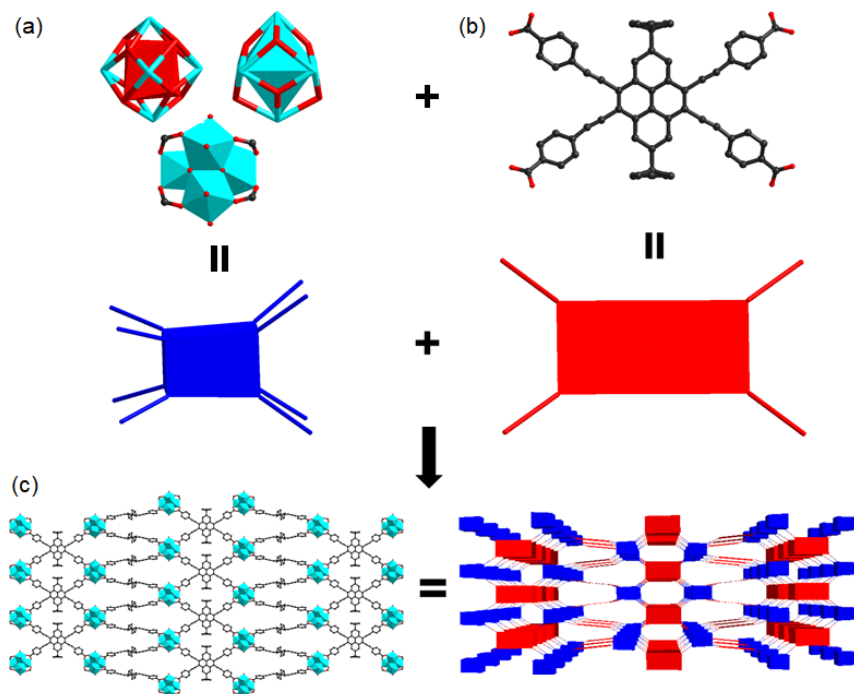


Figure III-2. Representative structure and topology of (a) the 8-connected Zr₆/Hf₆ cluster and (b) the tetratopic H₄BPETB that construct (c) PCN-822.

The pyrene-based ligand was synthesized in decent yield via modified Pd/Cu-catalyzed Sonogashira coupling reaction.¹⁹⁷ In H₄BPETB, four phenylacetylenic substituents took place at the 4,5,9,10-positions (K-region) of pyrene rather than 1,3,6,8-positions. The switched substitution was introduced with the aim of extending the π conjugation of the pyrene chromophore, red-shifting the wavelength of absorption. It has been revealed that the electrophilic substitution of pyrene prefers to occur at 1,3,6,8-positions.¹⁹⁸ To tackle the synthesis obstacle, two *t*Bu groups were used to occupy the 2- and 7- positions, leading to the K-region substitution. Yellow single crystals of PCN-822(Zr) were obtained under solvothermal reactions between zirconium(IV)

chloride and H₄BPETB with trifluoroacetic acid (TFA) as modulating agent. Similar reaction with hafnium(IV) chloride as starting material afforded single crystals of PCN-822(Hf). Powder X-ray diffraction (PXRD) were conducted and demonstrated the pure phase of both MOFs (Figure III-3). As the MOFs share the same framework structure confirmed by the single-crystal diffraction studies, the structure of PCN-822(Zr) was discussed as a representative. PCN-822 crystallizes in the tetragonal *I4₁/amd* space group. Generally, the framework is constructed by Zr₆ clusters connected by the rectangular BPETB linker. In the Zr₆(μ₃-O)₄(μ₃-OH)₄ cluster core, six Zr atoms form an idealized octahedron with the triangular faces capped by eight μ₃-oxygen atoms. The cluster is 8-connected where eight edges of the Zr₆ octahedron are bridged by eight carboxylate groups from H₄BPETB ligands, while the remaining positions are occupied by terminal hydroxy groups. It is noted that the symmetry of the cluster core is D_{2d}, as the eight μ₃-oxygen atoms on the triangular faces of the Zr₆ octahedron combine a distorted polyhedron rather than an idealized cube. In the BPETB linker, the peripheral benzene rings have 10.99° dihedral angle deviated from the pyrene central plane and each carboxylate connects with one Zr₆ clusters. Consequently, PCN-822 adopts a three-dimensional (3D) structure with a (4,8)-connected **sqc** topology. The framework contains two types of channels along either a or b-axes, while all pores are blocked along c-axis. The small channel with size of 0.6 × 1.8 nm² in quadrangle shape is surrounded by two Zr₆ clusters and two ligands, whereas the larger one with size of 0.8 × 3.2 nm² in pear-like shape is comprised of three Zr₆ clusters and three ligands (Figure III-2).

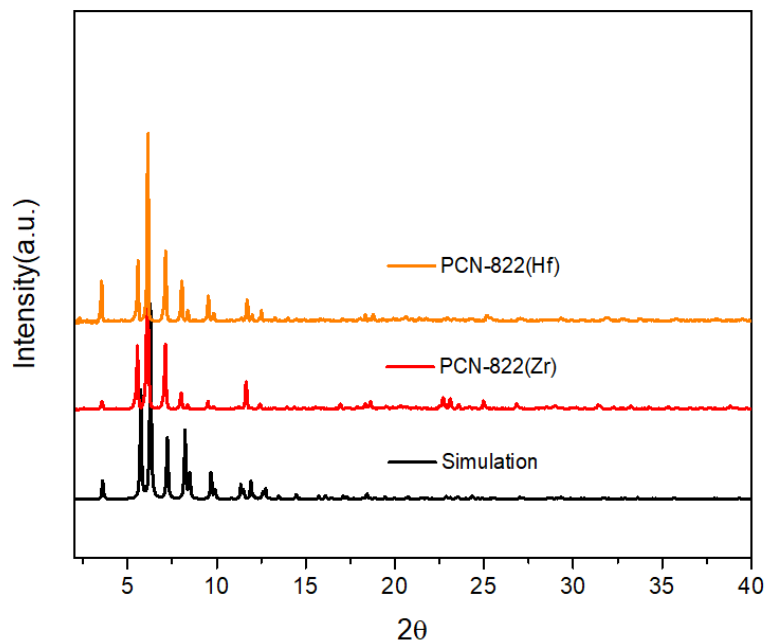


Figure III-3. PXRD patterns of as-synthesized PCN-822(Zr) in red, PCN-822(Hf) in orange and the simulated pattern in black.

The solvent accessible volume in fully evacuated PCN-822(Zr) is 56.5% calculated by Mercury with a probe of 1.8 Å. Due to the relatively large 1D channel sizes in two of the three dimensions, we failed to activate the MOFs for N₂ adsorption isotherms. Instead, the porosity of the materials was confirmed by dye adsorption in solution, showing that the materials could adsorb ~ two methyl orange (MO, ~ 1.42 nm × 0.35 nm × 0.19 nm) per formula unit (Figure III-4-6).

Table III-1. Crystal data and structure refinements for PCN-822 (Zr).

code	PCN-822(Zr)
CCDC	1908132
formula	C ₅₇ H ₂₈ O ₁₆ Zr ₃
<i>M_w</i>	1242.45
<i>T</i> / K	100(2)
Crystal system	tetragonal
Space group	<i>I</i> 4 ₁ / <i>amd</i>
<i>a</i> / Å	15.0920(12)
<i>c</i> / Å	98.494(7)
<i>V</i> / Å ³	22434(4)
<i>Z</i>	8
<i>D_c</i> / g cm ⁻³	0.736
<i>μ</i> (mm ⁻¹)	2.529
F (000)	4944
Completeness	0.988
Collected reflections	4617
Unique reflections	2083
Parameters	57
<i>R</i> _{int}	0.1176
<i>R</i> ₁ [<i>I</i> > 2σ]	0.1121
<i>wR</i> ₂ [<i>I</i> > 2σ]	0.3190
<i>R</i> ₁ (all data)	0.1655
<i>wR</i> ₂ (all data)	0.3561
GOF on <i>F</i> ²⁰	1.056

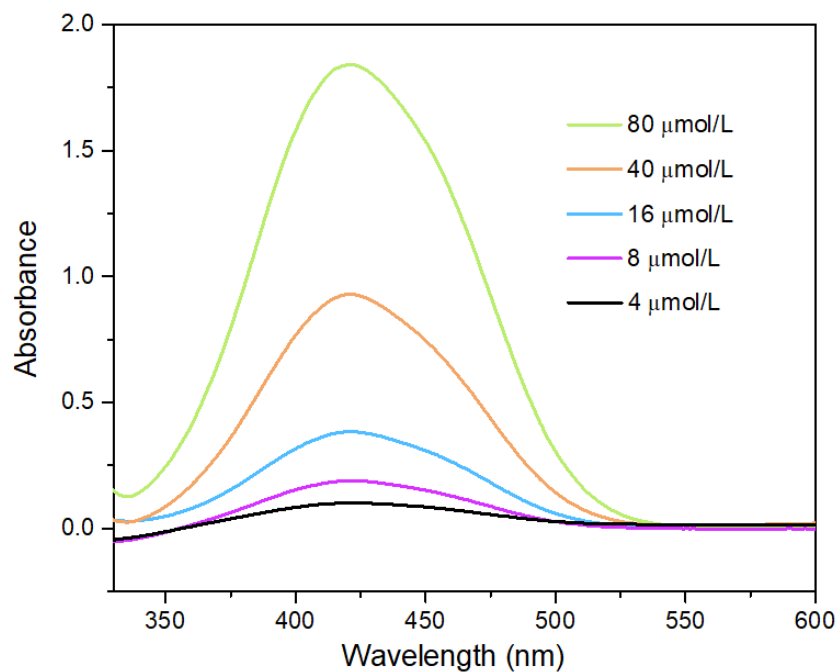


Figure III-4. UV-vis. spectra of methyl orange solutions with various concentrations.

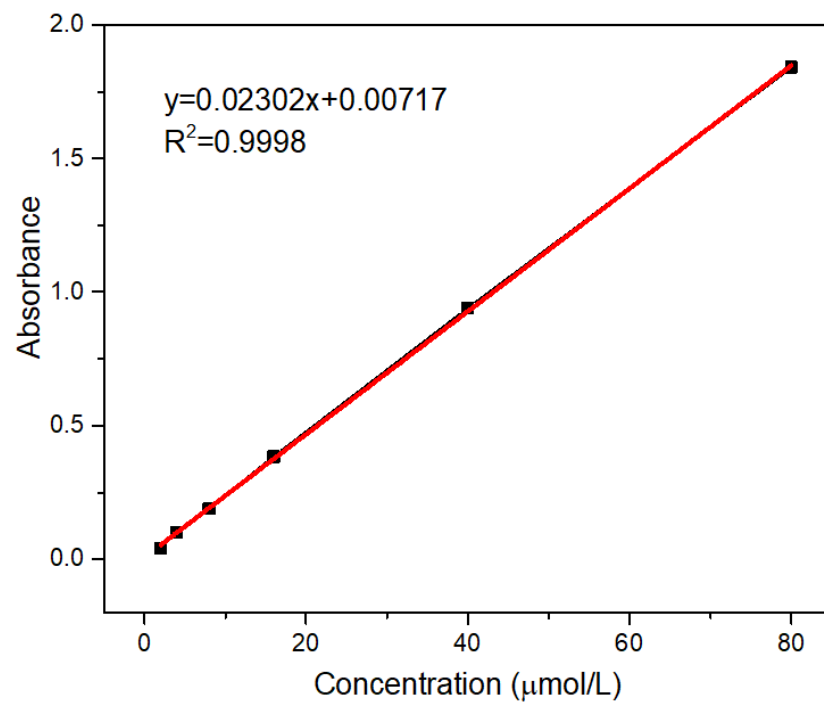


Figure III-5. Calibration curve obtained based on the UV-vis spectra.

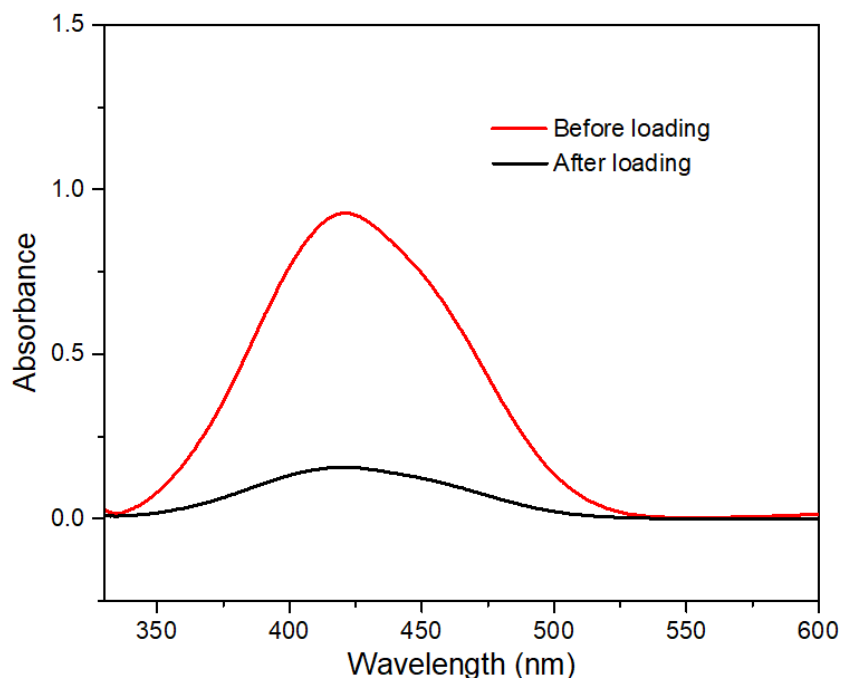


Figure III-6. The change of UV-vis spectra of methyl orange solution before and after loading PCN-822(Zr/Hf).

$$n(\text{MO}) = V \times (C_{\text{before}} - C_{\text{after}}) = (4000 - 646) \times 10^{-6} \text{ M} \times 3.00 \times 10^{-3} \text{ L}$$

$$= 10.1 \times 10^{-6} \text{ mol};$$

$$n(\text{MOF}) = 12.8 \text{ mg/M.W.} = 4.78 \times 10^{-6} \text{ mol};$$

$$n(\text{MO}) : n(\text{MOF}) \approx 2$$

3.3.2 Chemical and Thermal Stability

In spite of the large linker, both MOFs possessed excellent thermal and chemical stability. Thermal stability of PCN-822(Zr/Hf) was tested by thermogravimetric (TG) analyses under air stream. It showed that the decomposition temperature of both MOFs was around 450 °C and the weight loss before 320 °C was corresponded to the departure of isolated N, N-dimethylformamide (DMF) molecules and coordinated hydroxide groups/water molecules (Figure III-7). Water

treatment tests were also performed to demonstrate chemical stability of both MOFs. The as-activated samples were immersed into aqueous solutions with various pH values and allowed to stay overnight. The PXRD patterns of the samples after treatment were collected and showed unaltered profiles, indicating the intact crystallinity of the MOFs in the aqueous solutions with pH values ranging from 2 to 11(Figure III-8 & 9).

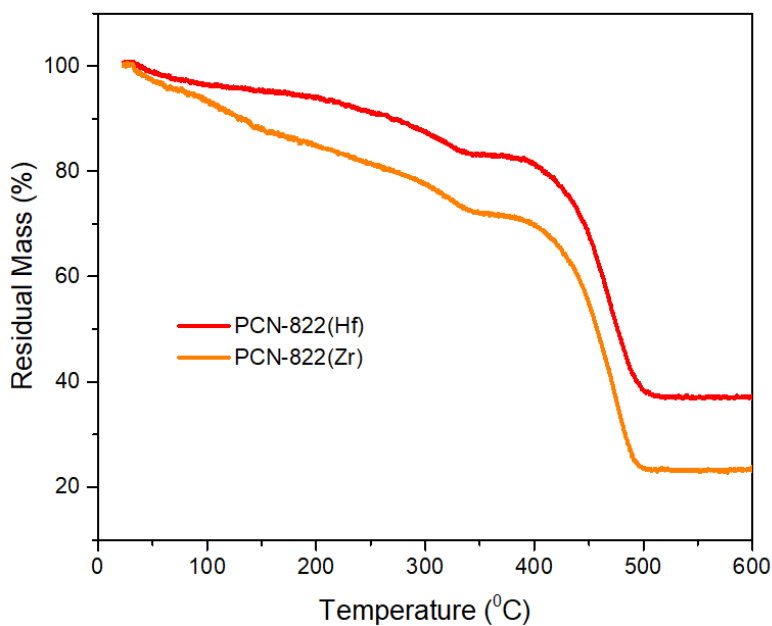


Figure III-7. Thermogravimetric (TG) analysis data of as-synthesized PCN-822(Zr/Hf).

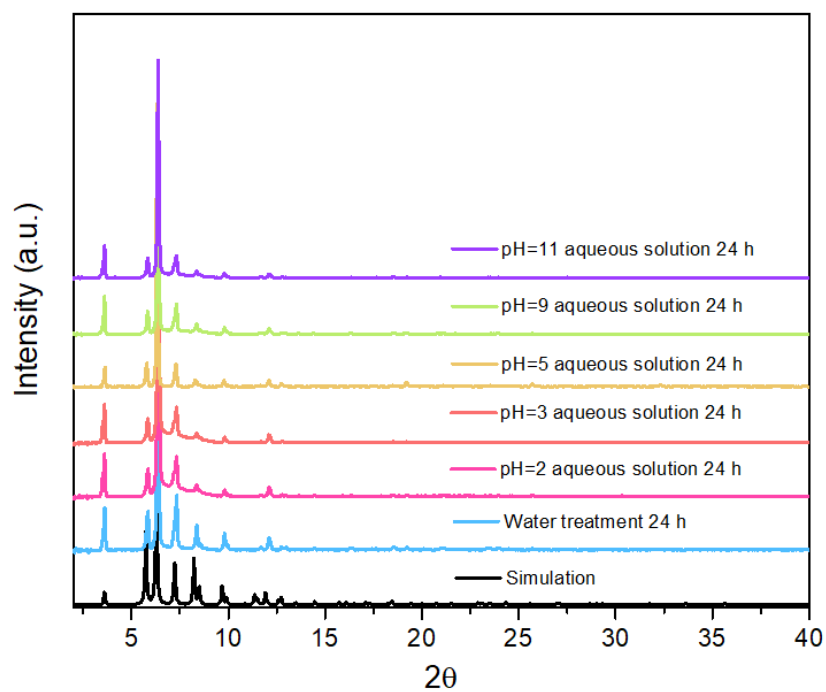


Figure III-8. PXRD patterns of PCN-822(Zr) after water treatment in aqueous solutions.

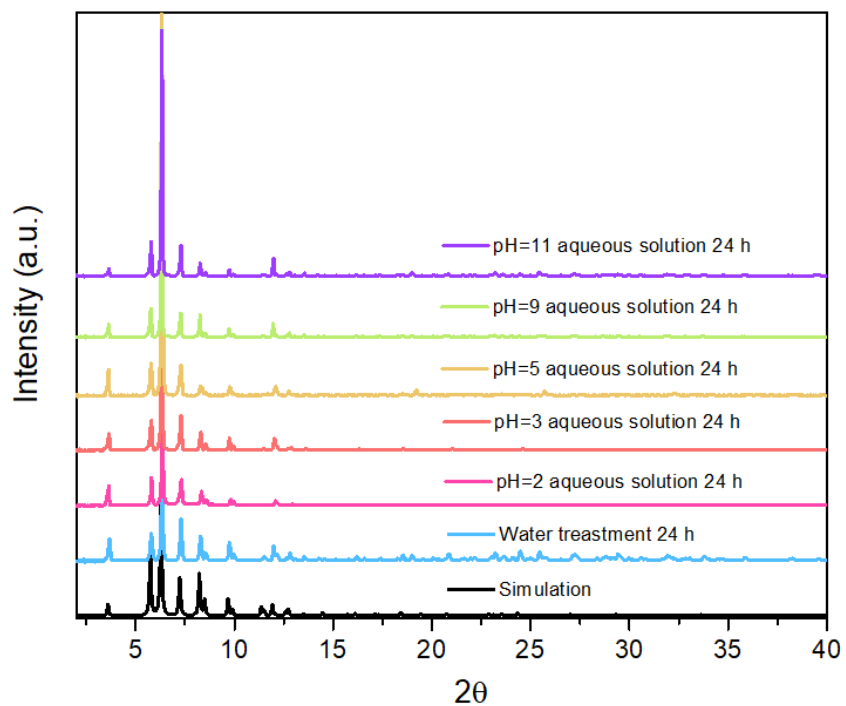


Figure III-9. PXRD patterns of PCN-822(Hf) after water treatment in aqueous solutions.

3.3.3 Photophysical Properties

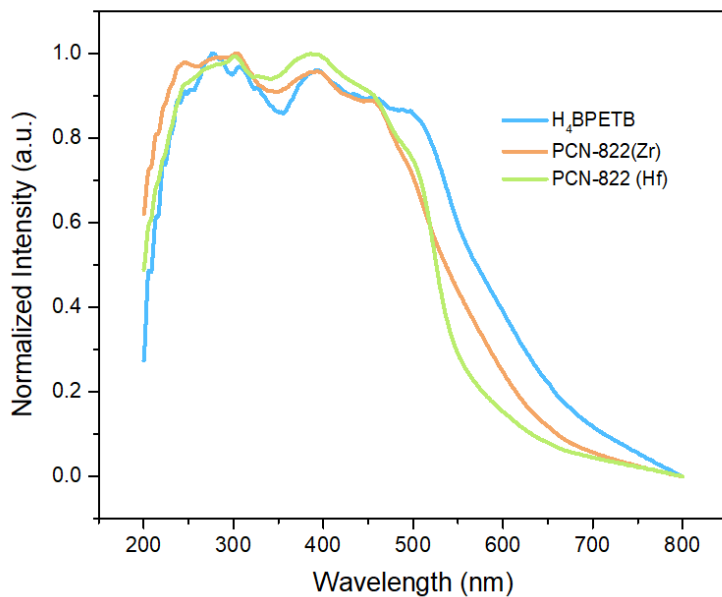


Figure III-10. Solid-state UV-vis adsorption spectra of ligand and PCN-822.

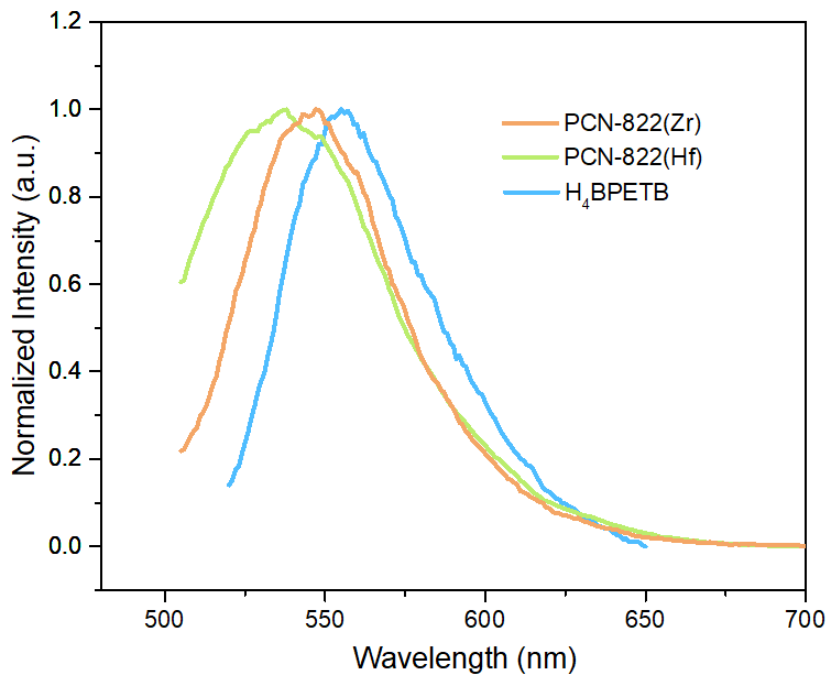


Figure III-11. Emission spectra of ligand and PCN-822(Zr/Hf).

Given that a good photosensitizer is supposed to have efficient absorption of the excitation light, especially in the range of visible light, we initially collected the solid-state absorption of PCN-822(Zr), PCN-822(Hf), H₄BPETB.¹⁹⁹ According to the absorption spectra, H₄BPETB exhibited a broad absorption ranging from 225 to 700 nm, while PCN-822 (Zr/Hf) had a slightly narrowed absorption from 225 to 650 nm (Figure III-10). Obviously, the electrons of the MOFs could be promoted to an excited state upon blue-green light irradiation, which is desirable for photocatalytic applications. Density functional theory (DFT) calculations were also performed to study the optical bandgap of ligand in free state and in the MOF. As shown in the Figure III-12, the highest occupied molecular orbital (HOMO) in free-state H₄BPETB is mostly delocalized over the central π -conjugated pyrene core, while the lowest unoccupied molecular orbital (LUMO) is formally delocalized over both the central π -conjugated pyrene core and the exterior phenylacetylenic carboxylate units. The frontier molecular orbital distributions of ligand in PCN-822 shows the similar profile compared to that in free state, confirming the inheritance of the visible-light absorption in the MOF fragments. Furthermore, the photoluminescence properties of the materials were studied based on solid-state Photoluminescent (PL) (Figure III-11). PCN-822(Zr) displayed emission peak observed at 547 nm upon excitation at 514 nm, while PCN-822(Hf) had an emission maximum at 538 nm excited at 487 nm. The similar emission features of the MOFs and small blue-shift in emission in comparison with that of ligand H₄BPETB (554 nm) demonstrated the ligand-based emission of the materials. The green fluorescence of MOFs was further confirmed by confocal scanning microscopic images (Figure III-13).

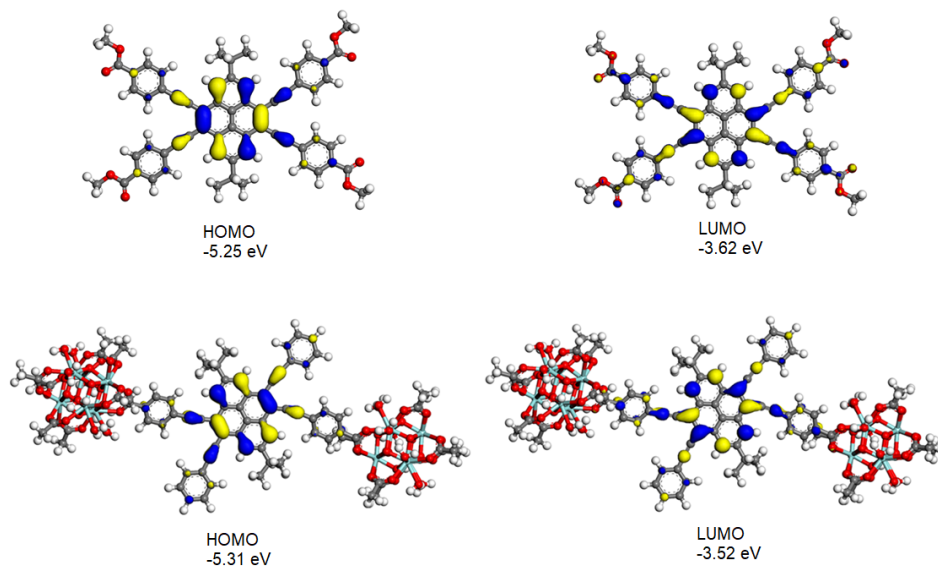


Figure III-12. The frontier molecular orbital distribution of free organic ligand (up) and in PCN-822.

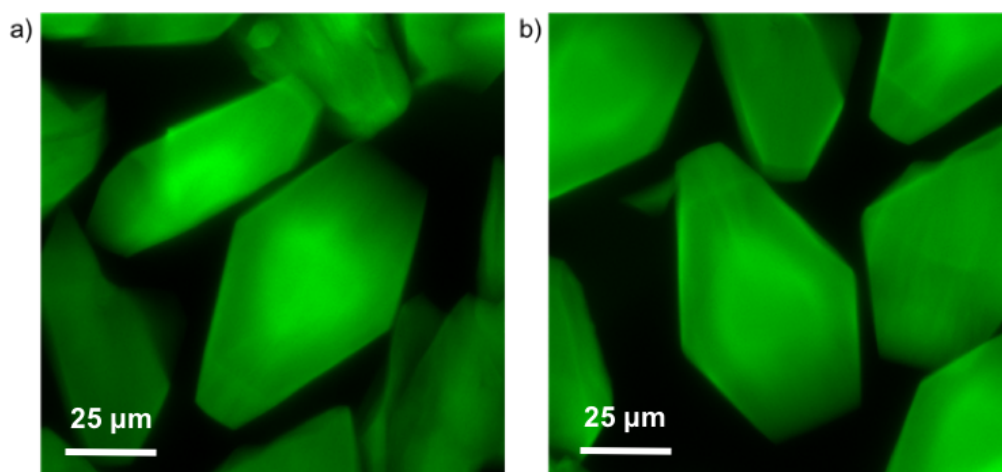


Figure III-13. Confocal scanning microscopic images of a) PCN-822(Zr) and b) PCN-822(Hf).

3.3.4 Photooxidation of 1,5-Dihydroxynaphthalene (DHN)

The ability of PCN-822(Zr/Hf) in singlet oxygen generation was evaluated by photooxidation of 1,5-dihydroxynaphthalene (DHN), where DHN acts as an efficient $^1\text{O}_2$

scavenger to produce 5-hydroxy-1,4-naphthalenedione (juglone).²⁰⁰ The reaction was carried out with 0.036 mmol of DHN in acetonitrile with 1 % PCN-822(Zr/Hf) under the irradiation of visible light and the UV-vis absorption of the mixture were recorded at an interval of one hour. As the reaction occurred, the absorption peak of DHN at 301 nm decreased, whereas the characteristic peak of juglone at 410 nm increased gradually. As shown in Figure III-14, with PCN-822(Hf) as photosensitizer, the absorption peak of DHN disappeared completely in 6 hours, indicating the consumption of the starting material. When PCN-822(Zr) was used as photosensitizer, it took longer time for the DHN absorption band to decay and the new absorption band of juglone developed more slowly compared with that of PCN-822(Zr) (Figure III-15 & 17). Therefore, PCN-822(Hf) possesses higher efficiency in $^1\text{O}_2$ generation, which might be ascribed to the heavy-metal effect of hafnium on enhancing the intersystem crossing of the materials. The reliability of the measurements was further tested by a control experiment with no addition of photosensitizer. The absorption spectrum showed slightly increase at 410 nm and negligible changes at 301 nm, revealing the stability of DHN under the reaction conditions (Figure III-16).

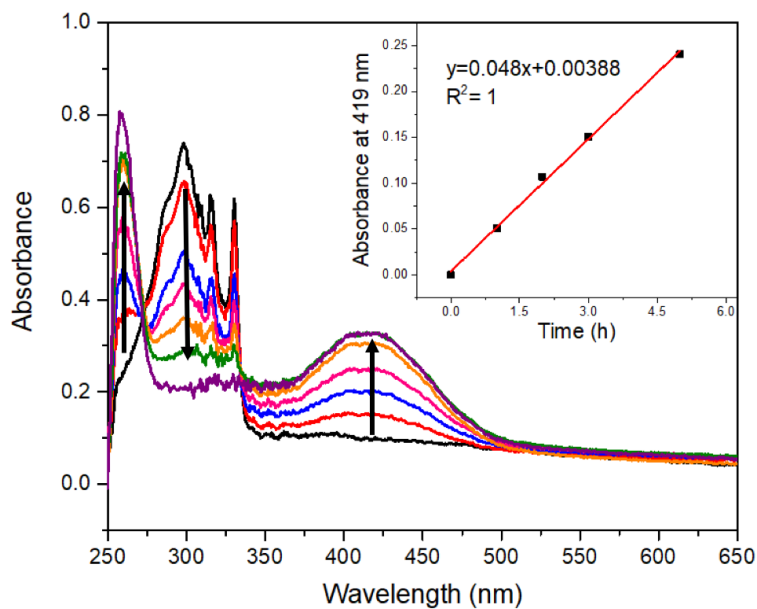
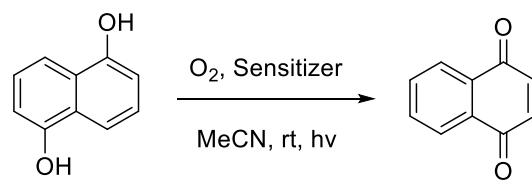


Figure III-14. Changes of UV-vis spectra for photooxidation of DHN sensitized by PCN-822(Hf).

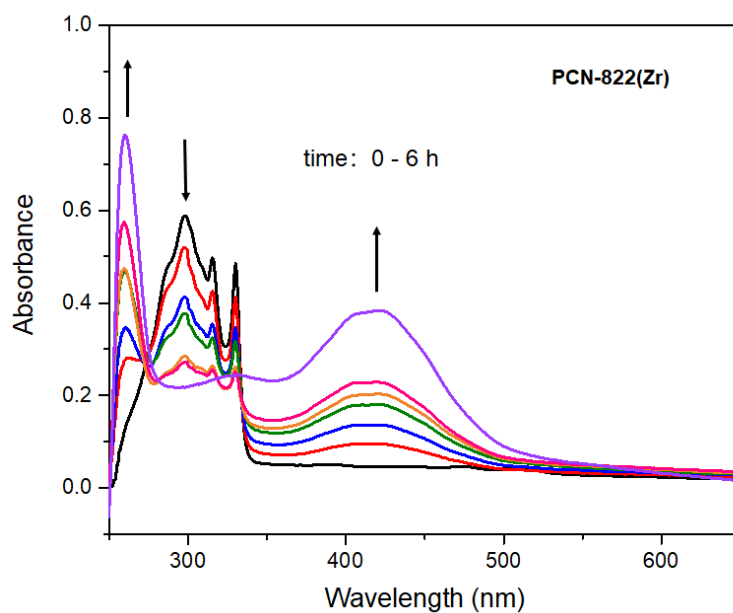


Figure III-15. Changes of UV-vis spectra for photooxidation of DHN sensitized by PCN-822(Zr).

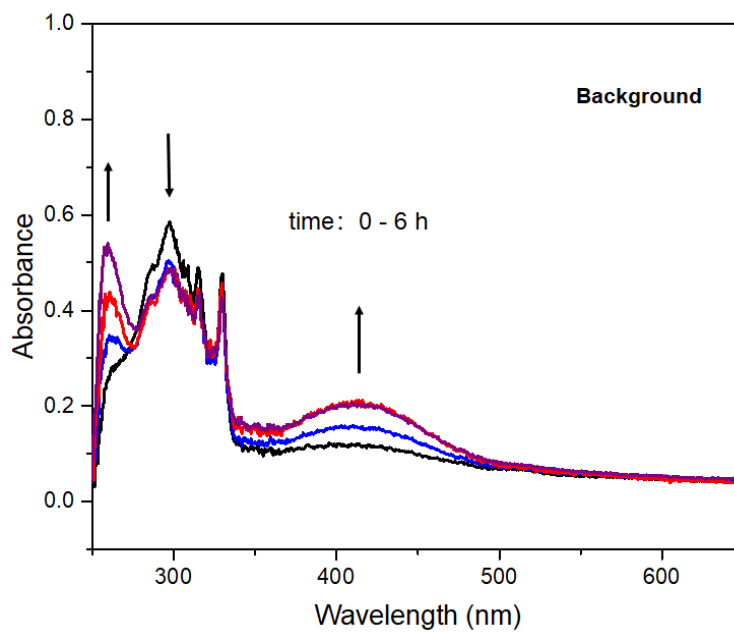


Figure III-16. Changes of UV-vis spectra for photooxidation of DHN with no sensitizer.

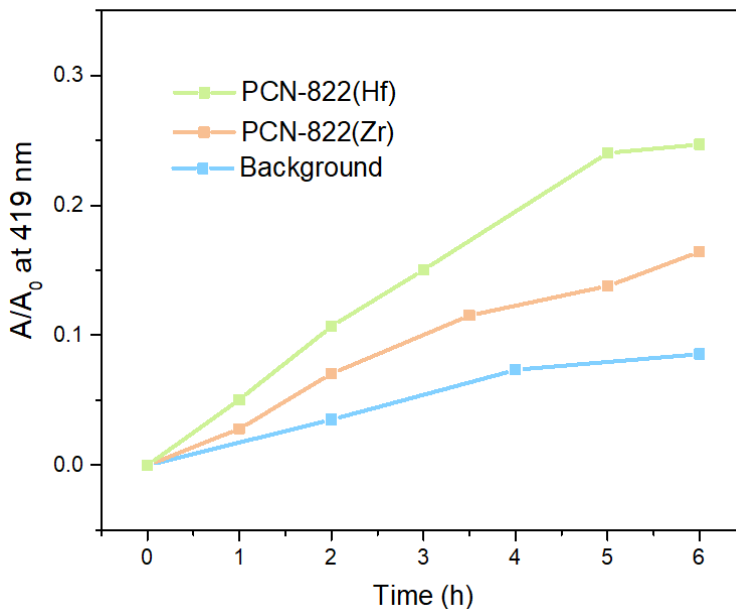


Figure III-17. Comparison of PCN-822 and ligand in juglone development.

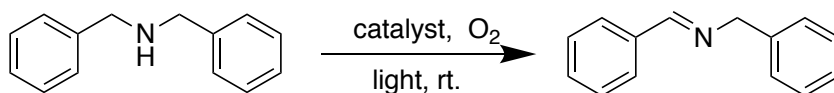
3.3.5 Oxidation of Various Amines

With the best performance in singlet oxygen generation, PCN-822(Hf) was chosen as photosensitizer for aerobic oxidation of amines to imines. Imines and derivatives are versatile intermediates in organic transformations and they are widely used in industry for the synthesis of fine chemicals and pharmaceuticals. Traditional synthetic protocols of imines generally involve unstable aldehydes, dehydrating agents as well as Lewis acid catalysts, hence, significant efforts have been dedicated to develop mild and practical methodologies for imine formation.²⁰¹⁻²⁰² Among all the methodologies, photoinduced aerobic oxidation of amines with turns out as an effective and sustainable approach from the view of green chemistry, as it can efficiently utilize sunlight, requiring relative mild and neat conditions.²⁰³⁻²⁰⁶ At the outset, dibenzylamine was chosen as a model substrate to optimize the reaction conditions. The reaction was generally

performed under O₂ atmosphere upon excitation of visible light at room temperature. As shown in the Table III-1, solvents exerted remarkable influence on oxidation of dibenzylamine, where acetonitrile was proved to be the most suitable medium compared with other types of solvents (entry 1-5). It is also noted that prolonged reaction deteriorated the formation of target product, leading to the dominating aldehyde byproducts (entry 4). As a result, with 1.0 mole % of PCN-822(Hf) photosensitizer, the starting material could be efficiently converted to the imine-based product with the highest yield in 6 h (entry 6). Control experiments were conducted without light irradiation or O₂ atmosphere (entry 7,8). As expected, no product was observed under these reaction conditions. Moreover, the necessity of photosensitizer was confirmed by entry 9 with no addition of PCN-822(Hf). Interestingly, when esterified ligand, Me₄BPETB, was used as photosensitizer, only 22.2% yield of product was achieved. The dramatic decrease in the formation of imine might be partially ascribed to the aggregation-caused quenching (ACQ) effect of the pyrene-based ligand in the solution.

PCN-822(Hf) also shows excellent chemical stability and recyclability. The MOFs separated from the reaction mixture could be reused two more times without loss of catalytic activity. The PXRD patterns of the samples recovered from each recycle showed no essential change in the profiles from the pristine ones, suggesting the intact crystallinity of the MOFs under the catalytic conditions (Figure III-18 & 19).

Table III-2. Screening experiments of oxidation of dibenzylamine^[a]



Entry	Catalyst (mol %)	Solvent	t (h)	Yield (%)
1	PCN-822(Hf) (0.5 %)	dichloromethane	6 h	15
2	PCN-822(Hf) (0.5 %)	ethyl acetate	6 h	30.3
3	PCN-822(Hf) (0.5 %)	acetonitrile	6 h	66
4	PCN-822(Hf) (0.5 %)	chloroform	6 h	< 5
5	PCN-822(Hf) (0.5 %)	THF	6 h	36.9
4	PCN-822(Hf) (0.5 %)	acetonitrile	12 h	51
6	PCN-822(Hf) (1.0 %)	acetonitrile	6 h	79
7 ^[b]	PCN-822(Hf) (1.0 %)	acetonitrile	6 h	—
8 ^[c]	PCN-822(Hf) (1.0 %)	acetonitrile	6 h	—
9	—	acetonitrile	6 h	—
10	Me4BPETB/HfCl4 (1.0%)	acetonitrile	6 h	22.2

[a] Reaction conditions: dibenzylamine (0.1 mmol), catalyst, solvent (2.0 mL), 1 atm O₂, rt., 100 mW cm⁻² Xe lamp cutoff below 420 nm. [b] Without light. [c] Under 1 atm N₂. Yields were determined by ¹H NMR with mesitylene as internal standard.

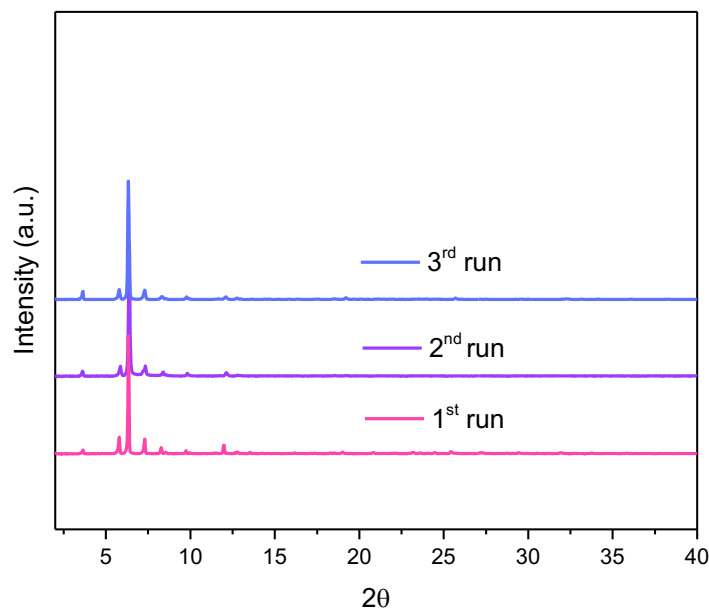


Figure III-18. PXRD patterns of recycled PCN-822 (Hf) (1st run, pink; 2nd run, violet; 3rd run, blue).

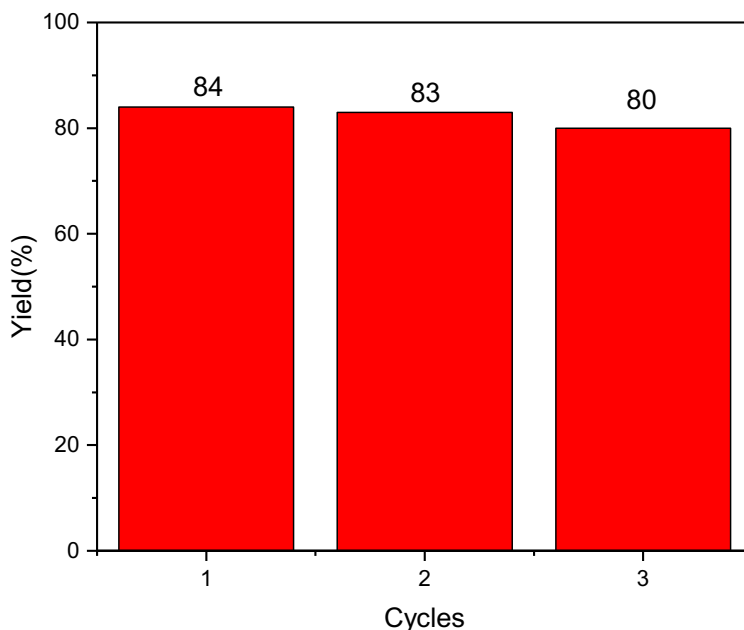


Figure III-19. Recycling performance of PCN-822 (Hf) in oxidation of dibenzylamine.

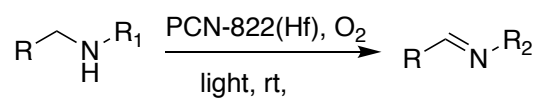
Under the optimized conditions, the oxidation of various amines was further conducted to evaluate the general capability of PCN-822(Hf). As shown in table III-2, both primary and secondary amines could be oxidized to the corresponding imines with satisfactory yields. Primary amines underwent oxidative coupling reaction photocatalyzed by PCN-822(Hf). It was noted that para-substituted benzylamines with electron-donating groups (CH_3 and OCH_3) afforded higher yields of imines by oxidative coupling than those with electron-withdrawing groups (Cl and CF_3), indicating the remarkable electronic effect on the oxidation reactions (entries 1-5). In addition, no product was observed when catalyzing aniline, which suggested that the coupling reaction experiences an abstraction of α -hydrogen of the substrates (entry 6). Compare to primary amines, secondary amines gave imines by oxidative dehydrogenation. Due to the possible oxidative

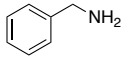
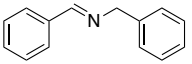
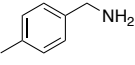
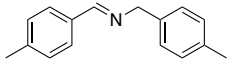
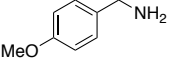
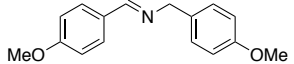
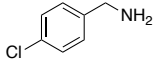
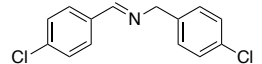
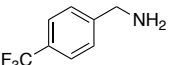
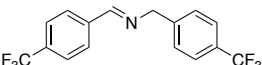
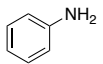
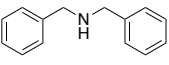
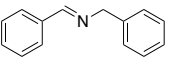
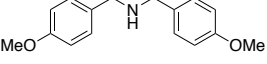
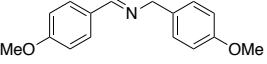
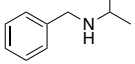
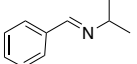
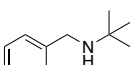
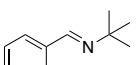
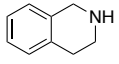
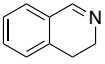
cleavage of the C=N bond, they presented relatively lower yields and selectivity in imine formation (entries 7-10). Substrates with bulky substitutes also reacted smoothly, which might be facilitated by the large channels of the MOF (entry 8 & 10). Besides aromatic amines, heterocyclic amines such as 1,2,3,4-tetrahydroisoquinoline could also be oxidized to dehydrogenated imine with decent yield and high selectivity (entry 11).

Table III-3. Comparison of aerobic dibenzylamine oxidation with selective catalysts.

Entry	Photocatalyst	Time (h)	Yields (%)	Light source	Ref.
1	WS ₂	36	63	white LED, 60 W	207
2	TiO ₂	8	91	Hg lamp ($\lambda > 300$ nm), 100 W	208
3	mpg-C ₃ N ₄	2	70	Xe lamp ($\lambda > 420$ nm), 300 W	209
4	Ru ^{II} (TDCPP)(CO)	8	>99	tungsten lamp, 300W	203
5	H ₂ TPrPc	1	>99	LED ($\lambda = 440$ nm), 3W	210
6	Ru(bpy) ₃	1	58	Xe Lamp ($\lambda > 380$ nm), 20 mW/cm ²	211
7	NH ₂ -MIL-125(Ti)	12	68	Xe lamp($\lambda > 420$ nm), 300 W	205
8	PCN-222	1	100	Xe lamp ($\lambda > 420$ nm), 100 mW/cm ²	206
9	PCN-822(Hf)	6	79	LED light ($\lambda = 450$ nm), 100 mW/cm ²	This work

Table III-4. Oxidation of various amines



Entry	Substrate	Product	Yield (%)	Sel. (%)
1			93	98
2			90	98
3			91	98
4			81	90
5			83	96
6		—	—	—
7			79	84
8			76	83
9			82	86
10			79	85
11			92	95

3.3.6 Mechanisms

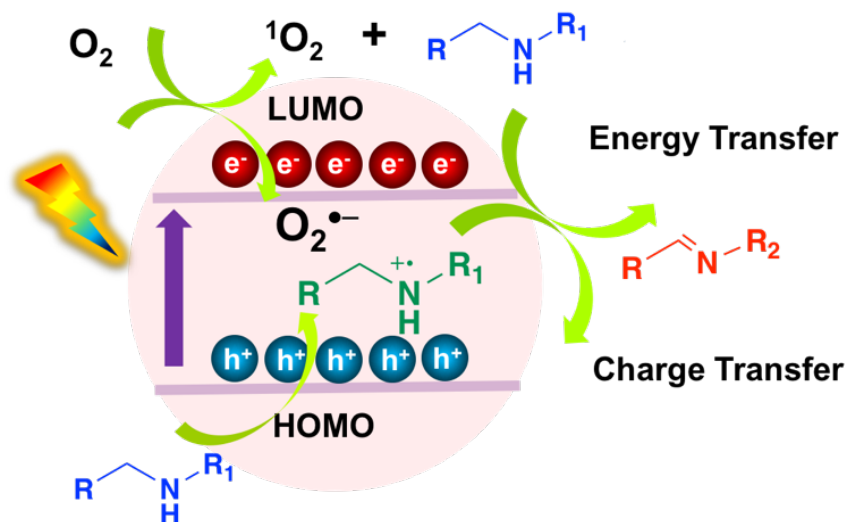


Figure III-20. Proposed mechanisms of oxidation of amines.

Although the mechanism underlying the oxidation reaction remains disputable, two possible pathways were proposed to explain the excellent photocatalytic performance of PCN-822(Hf) (Figure III-20). Firstly, as PCN-822(Hf) has been proved to be an excellent singlet oxygen generator, a mechanism was proposed where the material produces $^1\text{O}_2$ species to oxidize amine via energy transfer upon the light irradiation. The generation of the singlet oxygen was further confirmed by 2,2,6,6-tetramethylpiperidine (TEMP), a classic $^1\text{O}_2$ trapping agent, which displayed featured signals in the electron paramagnetic resonance (EPR) spectra (Figure III-21). Regarding to the semiconductor nature of MOFs, an alternative mechanism involving photoinduced electron-transfer process is also operable. It is assumed that the reaction was initiated by the excitation of PCN-822(Hf) upon visible-light irritation, which gives rise to electron (e^-) and hole (h^+) pairs separated in the highest occupied molecular orbital (HOMO) and the lowest unoccupied molecular orbital (LUMO) of the material. The photogenerated electron reduces molecular oxygen to its

activated superoxide radical species, $O_2^{\bullet-}$, while the hole oxidizes amine to a cationic amine radical. The amine radical and $O_2^{\bullet-}$ then react with each other to produce imine via proton and hydrogen transfer. For primary amine, the formed imine serves as an intermediate, which is further attacked by another amine to give the final coupled product. EPR spectra showed an enhanced signal upon light irradiation relative to that taken under darkness, which indicates the photogenerated radicals like electron-hole pair (Figure III-22). To further ascertain the photoinduced electron-transfer mechanism, the energy diagram of PCN-822(Hf) was estimated by UV-vis spectra combined with cyclic voltammetry (Figure III-23 & 24). According to cyclic voltammogram, the reduction potential of PCN-822(Hf) was -0.55V vs. SHE, corresponding to LUMO level. The relatively more negative potential theoretically enables the material to reduce molecular oxygen to $O_2^{\bullet-}$ ($E(O_2/O_2^{\bullet-}) = -0.33\text{V}$ vs. SHE). The optical band gap of PCN-822(Hf) was calculated to be 2.17 eV on the basis of Tauc plot, from which HOMO level was determined to be 1.62 V vs. SHE. As the $E_{1/2}(M^+/M)$ of amines is around $+1.47\text{ V}$ vs. SHE, the more positive HOMO level of PCN-822(Hf) should be sufficient for the amine oxidation.

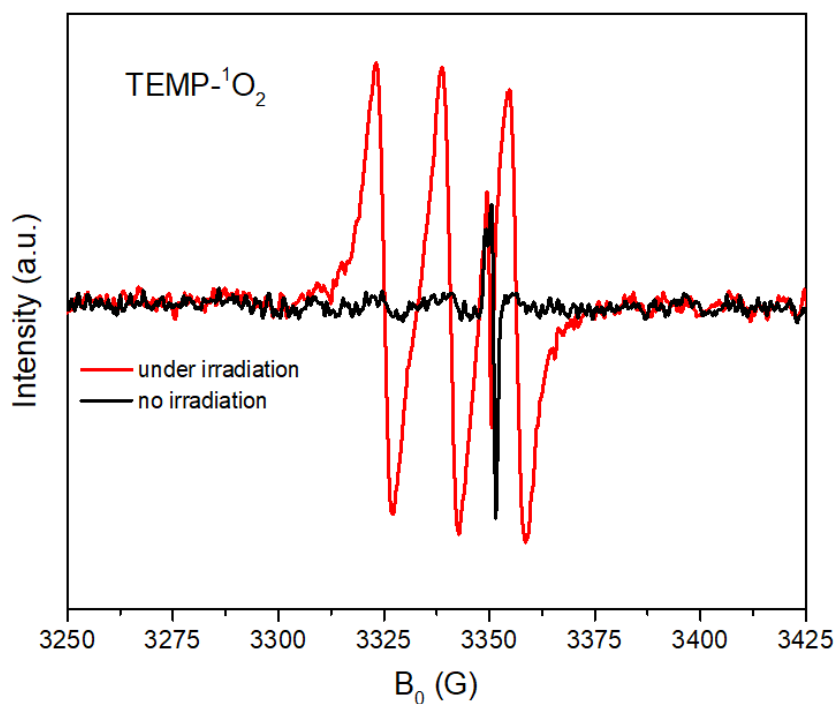


Figure III-21. EPR spectra of TEMP-¹O₂ obtained with or without light irradiation.

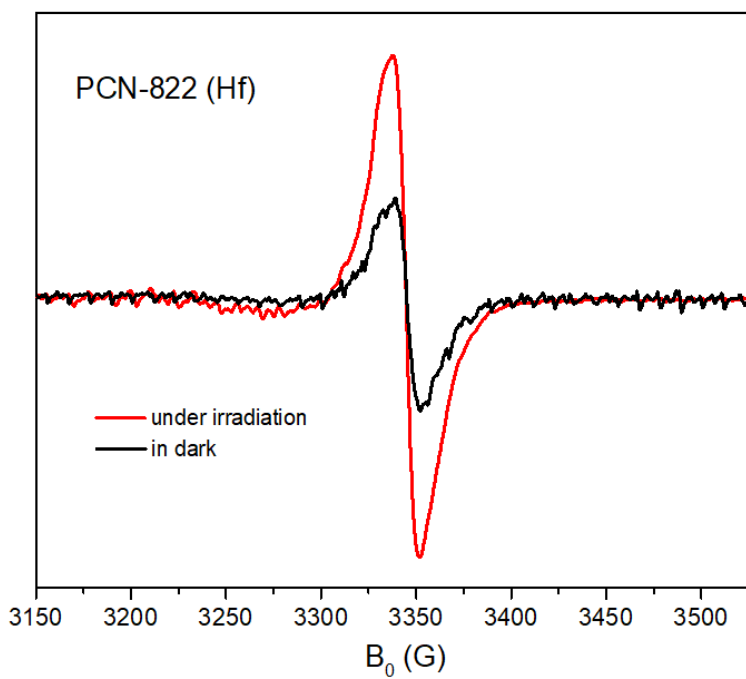


Figure III-22. EPR spectra of PCN-822(Hf) obtained in the dark and under visible light irradiation

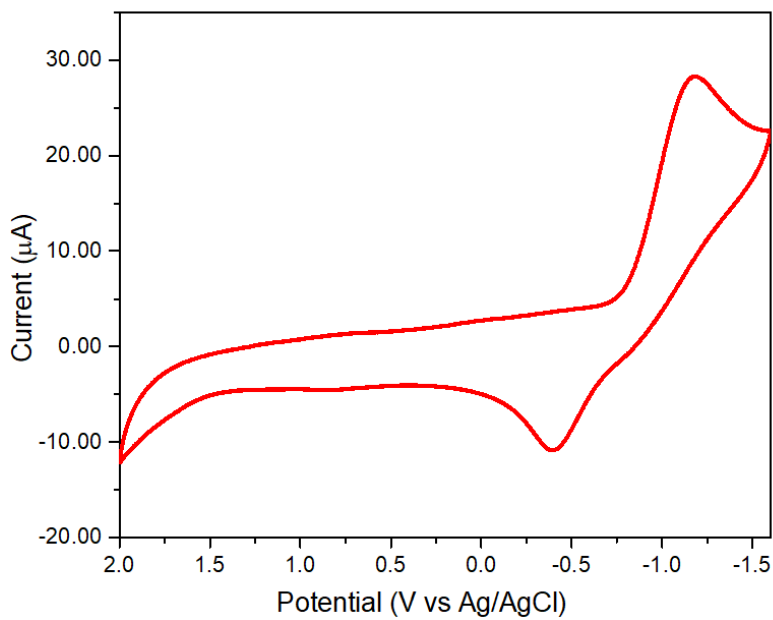


Figure III-23. Cyclic Voltammetry tests of PCN-822(Hf).

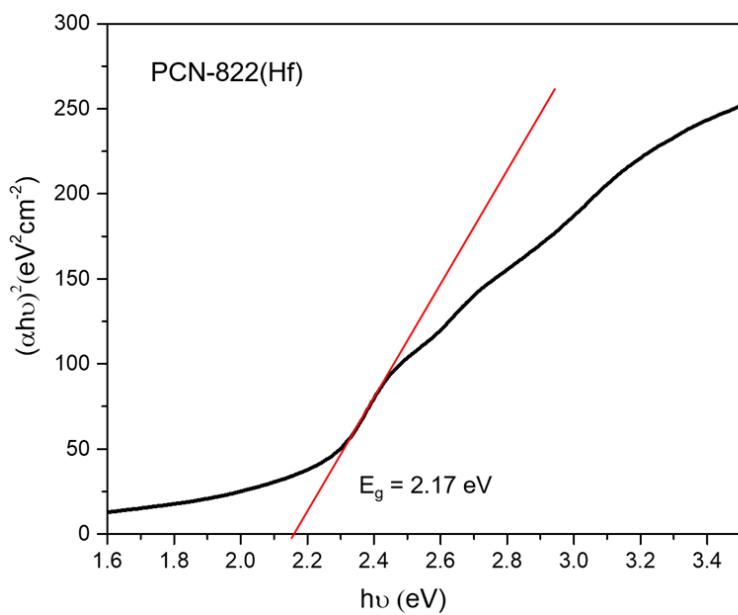


Figure III-24. Tauc plot of PCN-822(Hf). The optical band gap is calculated to be 2.17 eV.

3.4 Conclusion

In summary, a tetratopic pyrene-based ligand (H₄BPETB) was rationally designed to construct two novel porous MOFs, PCN-822(Zr/Hf), by assembly with zirconium/hafnium clusters. The MOFs have a broad adsorption of visible light up to 650 nm. The desired optical adsorption of the materials is mainly ascribed to the 4,5,9,10-positions (K-region) substitution of the pyrene-derived ligand, which leads to an extended π -conjugated moiety. Merging the merits of pyrene in singlet oxygen generation and the visible-light harvesting, PCN-822(Zr/Hf) exhibit an efficient capability in activating molecular oxygen to ¹O₂ under the excitation of visible light. Furthermore, PCN-822(Hf) is demonstrated to be highly active in oxidation of various amines to imines. Possible dual pathways are proposed for the light-driven transformation, involving the energy transfer-based ¹O₂ generation and photo-induced charge separation. The present work not only exemplifies a novel pyrene-based MOF as an inherent visible-light harvesting photosensitizer without the aid of other chromophores, but also illustrates the necessity of the structural design at the molecular level in the MOF-based photosynthesizing system.

CHAPTER IV

DIRECT SYNTHESIS OF FUNCTIONALIZED PCN-333 VIA LINKER DESIGN⁴

4.1 Introduction

Metal-Organic Frameworks (MOFs), an emergent class of porous materials, have gathered intense attention in the past two decades. The judiciously selected metal clusters and organic linkers impart MOFs with unique properties, namely, intrinsic crystallinity, porosity, structural or functional diversity, and tunability, which make them promising candidates in many applications such as gas storage, separation, catalysis, drug delivery and sensing.^{18, 116, 212-214} Among various MOFs, mesoporous MOFs with the ability to encapsulate large molecules like organometallic catalyst, nanoparticles and enzymes, have been extensively utilized in chemo/bio applications.^{6, 215} However, in spite of the benefits brought by such encapsulation, the accommodation of functional large molecules sacrifices partial pore volume, which decreases the diffusion efficiency and accessibility of the subsequent-coming species. Hence, it would be ideal to directly synthesize mesoporous MOFs with functionalized building blocks, especially organic linkers.³⁴

Iron is one of the most ubiquitous elements in life and environment. It plays indispensable role in many biological processes such as oxygen metabolism, electron transfer and synthesis of DNA and RNA.²¹⁶ Permissible limit of iron in drinking water given by the World Health Organization (WHO) is 0.3 mg/mL.²¹⁷ Both the deficiency and excess of Fe³⁺ from the normal permissible limit will break cellular homeostasis and cause serious biological disorders like

⁴ Reproduced with permission from “Direct synthesis of functionalized PCN-333 via linker design for Fe³⁺ detection in aqueous media” by Zhang, Y.; Yang, X.; Zhou, H. C., *Dalton Trans.*, **2018**, 47 (34), 11806-11811, copyright @ 2018 Royal Society of Chemistry.

microcytic hypochromic anemia and Alzheimer's disease.²¹⁸ To dates, many methods have been put forward for Fe³⁺ detection including liquid chromatography, inductively coupled plasma atomic mass spectrometry (ICP-MS) and atomic absorption spectrophotometry (AAS).²¹⁹⁻²²¹ Among them, luminescent sensing stands out because of its portability, simplicity, fast and visible response. Accordingly, various luminescent materials have been designed and synthesized in the pursuit of sensing the metal ion with high sensitivity and selectivity.^{15, 222-224} Luminescent MOFs (LMOFs) with their unique photoluminescence properties have recently bloomed out as potential chemical sensors for Fe³⁺ recognition.^{116, 225} However, most of luminescent MOFs exhibit moderate aqueous stability and rely on ion exchange mechanism for Fe³⁺ detection, which is time-consuming and sometimes leads to the collapse of MOF structures. Therefore, luminescent MOFs that display good aqueous stability as well as fast response towards Fe³⁺ ions in water system are pressingly needed.

MIL-100 series are promising candidates for Fe³⁺ detection due to their superb stability in water due to the inert bonds formed between the tritopic linkers and trimeric metal clusters.⁷ The expanded version of MIL-100, known as PCN-333(M) (M= Fe, Al, Sc), can also survive such harsh conditions.^{25, 226} Instead of large channels, PCN-333 contains large cavities with a diameter of 5.5 nm, which will not only prompt the pre-concentration of the analytes but also accelerate the diffusion of incoming species. However, the original PCN-333 shows no fluorescent response to Fe³⁺ ions due to the lack of efficient binding sites. Herein, in this work, through judicious selection of organic building blocks, we directly built a luminescent MOF of PCN-333, named as PCN-604, from aluminium trimetric clusters and pyridine-based 4,4',4''-(pyridine-2,4,6-triyl)tribenzoic acid (H₃PTB) ligands. Like PCN-333, the MOF exhibits excellent thermal and chemical stability and the ultrapores can be activated directly through regular degas process for further usage. Working

as a luminescent sensor, PCN-604 shows intense luminescence in water and has promising sensitivity and selectivity towards trace amount of Fe³⁺ ions demonstrated by the high quenching constant of $2.85 \times 10^4 \text{ M}^{-1}$ and low detection limit of 6.2 μM .

4.2 Experimental Section

4.2.1 Materials and Instrumentation

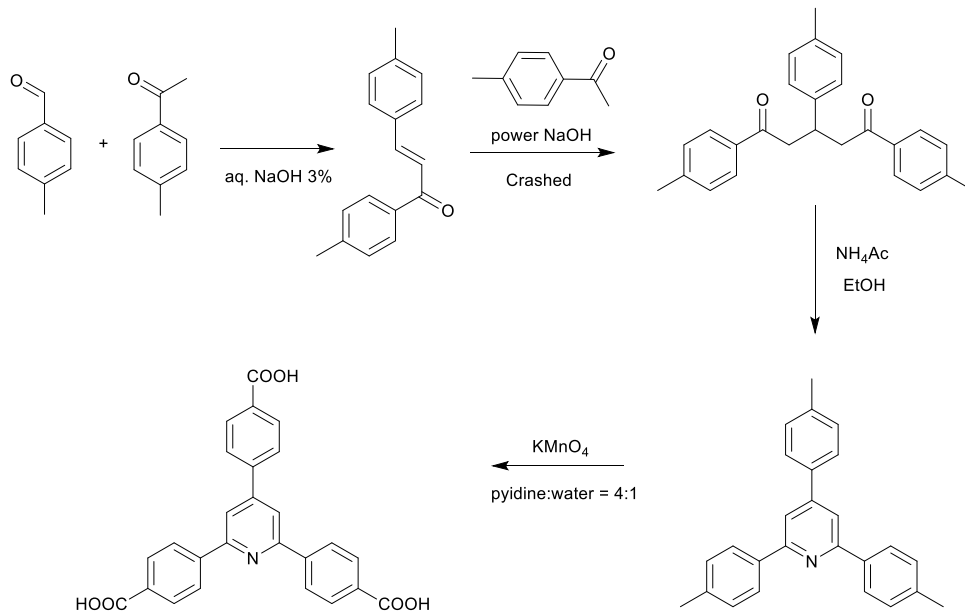
Materials

p-toluenealdehyde, 4-methylacetophenone, ammonium acetate, potassium permanganate (KMnO₄), aluminium chloride hexahydrate (AlCl₃·6H₂O), N, N-diethylformamide (DEF), tetrafluoroacetic acid (TFA) were purchased from either VWR or Sigma Aldrich. Unless otherwise noted, all commercial chemicals were used without further purification.

Instrumentation

Synchrotron powder X-ray diffraction (PXRD) was carried out with Bruker D8-Discover diffractometer equipped with a Mo sealed tube ($\lambda = 0.72768 \text{ \AA}$) on the beamline 17-BM at the Advanced Photon Source, Argonne National Laboratory. In-house powder X-ray diffraction (PXRD) was carried out on a Bruker D8-Focus Bragg-Brentano X-ray powder diffractometer equipped with a Cu sealed tube ($\lambda = 0.72768 \text{ \AA}$) at 40 KV and 40 mA. UV-Vis spectra were recorded on Shimadzu UV-2450 spectrophotometer. Fluorescence spectra were collected on Horiba Fluorolog spectrofluorometer. Thermogravimetric analyses (TGA) were carried out on a Shimadzu TGA-50 thermal analyzer from temperature to 600 °C at a ramp rate of 5 °C /min in a flowing air atmosphere. Nuclear magnetic resonance (NMR) data were collected on a Mercury 300 spectrometer. Low pressure gas adsorption measurements were performed on an ASAP 2020 with the extra-pure quality gases.

4.2.2 Ligand Synthesis



Scheme IV-1. Synthetic procedures of H₃PTB.

Step 1. Synthesis of 1,3-di-p-tolyl-propenone

In a 250 mL round-bottom flask, p-tolaldehyde (6.0 g, 50 mmol), 4-methylacetophenone (6.8 g, 51 mmol) and 3 % aqueous sodium hydroxide (150 mL) were mixed and rigorously stirred at room temperature for 30 min. The mixture was then heated up to 60 °C and allowed to react for another 12 hours. After cooling to the room temperature, the resulted light-yellow precipitate was filtered, washed thoroughly with water and air-dried for next step without further purification.

Step 2. Synthesis of 2,4,6-tri-p-tolyl-pyridine

4-methylacetophenone (4.0 g, 30 mmol), 1,3-di-p-tolyl-propenone (7.0 g, 30 mmol) and sodium hydroxide (4.8 g, 120 mmol) were crashed together with pestle and mortar for about 2

hours until the mixture turned to yellow powder. The solid was then transferred into a round-bottom flask which contains an excess of ammonium acetate (20 g) dissolved in 200 mL ethanol. The reaction mixture was heated under reflux overnight. Upon cooling to the room temperature, the precipitate was filtered, washed with water three times and dried. The crude product was further purified by column chromatography (eluent: ethyl acetate : hexane = 10 : 1) to yield white solid (4.2 g, 40 %). ¹H NMR (300 MHz, CDCl₃): δ 8.07 (d, J = 8.3 Hz, 4H), 7.79 (s, 2H), 7.61 (d, J = 8.4 Hz, 2H), 7.28 (d, J = 8.4 Hz, 6H), 2.42, (s, 9H).

Step 3. 4,4',4'' -(pyridine-2,4,6-triyl)tribenzoic acid (H₃PTB)

In a 500 mL three-necked flask, 2,4,6-tri-p-tolyl-pyridine (1.62 g, 4.7 mmol) was added to a mixing solvent (pyridine/water=200 mL/50 mL). The reaction mixture was heated up to 100 °C and 32 g KMnO₄ was added in portions with 8 g each time. After 24 hours, the dark mixture was cooled down and filtered to give a clear filtrate. The organic solvent was vacuumed up and the aqueous phase was acidified with 6M hydrochloric acid (until pH < 3). The obtained pale-yellow solid was then filtered, washed with water and acetone several times and dried to give the pure product (1.89 g, 90%). ¹H NMR (300 MHz, dmsO): δ 8.51 (d, J = 8.5 Hz, 4H), 8.44 (s, 2H), 8.25 (d, J = 8.5 Hz, 2H), 8.13 (d, J = 8.5 Hz, 6H).

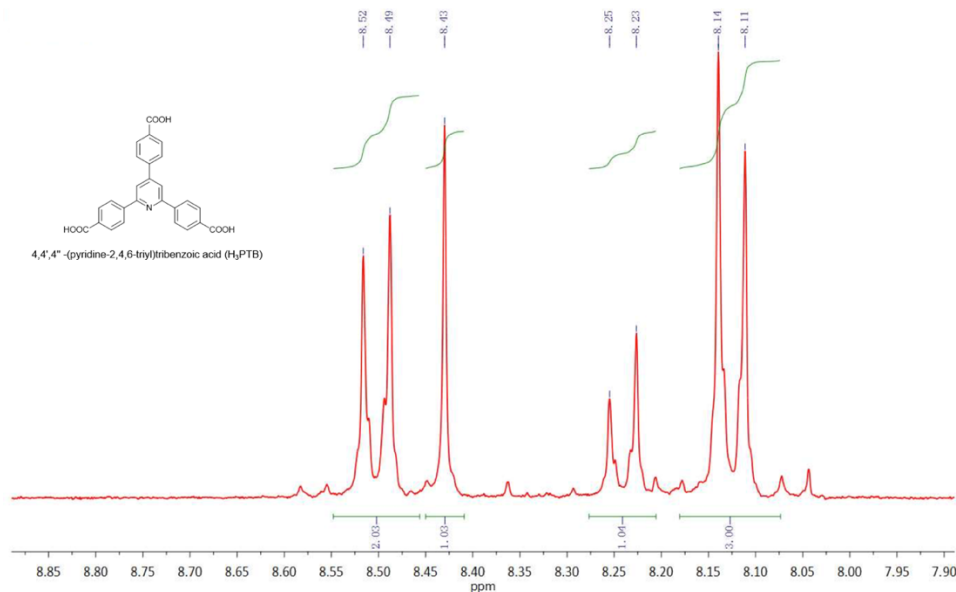


Figure IV-1. ^1H NMR spectrum of H_3PTB .

4.2.3 Synthesis of PCN-604

In a 4 mL Pyrex vial, $\text{AlCl}_3 \cdot 6\text{H}_2\text{O}$ (30 mg, 124.2 μmol), H_3PTB (10mg, 22.8 μmol) and 270 μL TFA were ultrasonically dissolved in 2 mL DEF. The mixture was then heated in a 135 $^\circ\text{C}$ oven for 2 days to afford white crystalline powder. Yield: 4 mg.

4.2.4 Activation of PCN-604

~ 50 mg as-synthesized PCN-604 samples were firstly washed with DMF (3 mL \times 3) and acetone (3 mL \times 3). The samples were again immersed in acetone to undergo solvent-exchange process with fresh acetone three times within 12 hours. Afterwards, the acetone was decanted and the mixture samples were dried under vacuum for 10 min, transferred into BET tube and then activated by the ‘outgas’ function of Micrometric ASAP 2020 system for one hour at 150 $^\circ\text{C}$ before the gas sorption measurement by the instrument.

4.2.5 Fluorescence Quenching and Titration Experiments

To study the sensing capability of PCN-604 towards metal ions, fifteen different metal ions, Na⁺, K⁺, Ag⁺, Mg²⁺, Ca²⁺, Mn²⁺, Fe²⁺, Co²⁺, Ni²⁺, Cu²⁺, Zn²⁺, Cd²⁺, Al³⁺, Cr³⁺, Fe³⁺ were chosen and tested. ~15 mg fully-grounded powder samples were soaked in 30 mL deionized water and ultrasonically treated more than 30 min to prepare well-dispersed MOF suspension. Afterwards, 1 mL of 1mM aqueous solutions of the metal ions were added respectively to the 2 mL of as-prepared MOF suspension in cuvettes. In titration experiments, Fe³⁺ aqueous solution (1mM) was added to 2 mL of MOF suspension in an incremental manner from 50 μ L to 1000 μ L. All the corresponding fluorescence spectra were recorded at room temperature. The quenching percentage was calculated with the formula: $Q = (1 - I/I_0) \times 100\%$, where I_0 and I are the fluorescence intensity of the suspension before and after addition of analytes.

4.3 Results and Discussion

4.3.1 Topology Design and Structural Description of PCN-604

In order to achieve the direct synthesis of functionalized PCN-333 structure, 4,4',4'' - (pyridine-2,4,6-triyl)tribenzoic acid (H₃PTB) was chosen and synthesized with a modified procedure based on previously reported literature (Scheme IV-1).²²⁷ Unlike other tritopic linkers functionalized with hanging substituents such as 1,3,5-benzotribenzoic acid (H₃BTB) and its derivatives, the pyridine-based linker is only decorated with one nitrogen atom on the central benzene, which not only serves as an additional binding site, but also, more importantly, releases the rotating steric hindrance when building MOFs, allowing the six oxygen atoms on the linker to stay in the same plane to adopt approximate D_{3h} symmetry, an indispensable prerequisite of forming MTN topology.^{27, 226} The synthesis of PCN-604 was guided by the kinetically tuned

dimensional augmentation (KTDA) method with AlCl_3 and H_3PTB as starting materials.²²⁸ As confirmed by the powder X-ray diffraction (PXRD) patterns, PCN-604 is isostructural to PCN-333 and shares the same cubic **MTN** topology (Figure IV-2).²⁵ The corresponding structural model of PCN-604 was simulated based on the reported PCN-333 structure by Material Studio 6.0.¹⁵¹ The space group, $Fd\bar{3}m$, was used to describe the MOF structure. PCN-604 is composed of hybrid supertetrahedra building units connected in a vertex sharing manner, leading to a mesoporous structure. The supertetrahedra consist of aluminium octahedral trimers at the four vertexes linked by the organic linkers occupied at the four faces. Like PCN-333, PCN-604 also exhibits two types of mesoporous cages. The smaller cage is built of 20 supertetrahedra sharing vertex with a pentagonal window of 25.9 Å in diameter. The larger cage is hexacaidecahedral (hexagonal-truncated trapezohedral) formed by 24 supertetrahedra, displaying both pentagonal windows and hexagonal windows of 30 Å in diameter. The large cage lies in a honeycomb arrangement in the [111] projection. The inner diameter is 11 Å for the super tetrahedral cage, 34 Å for the dodecahedral cage and 55 Å for the hexacaidecahedral cage.

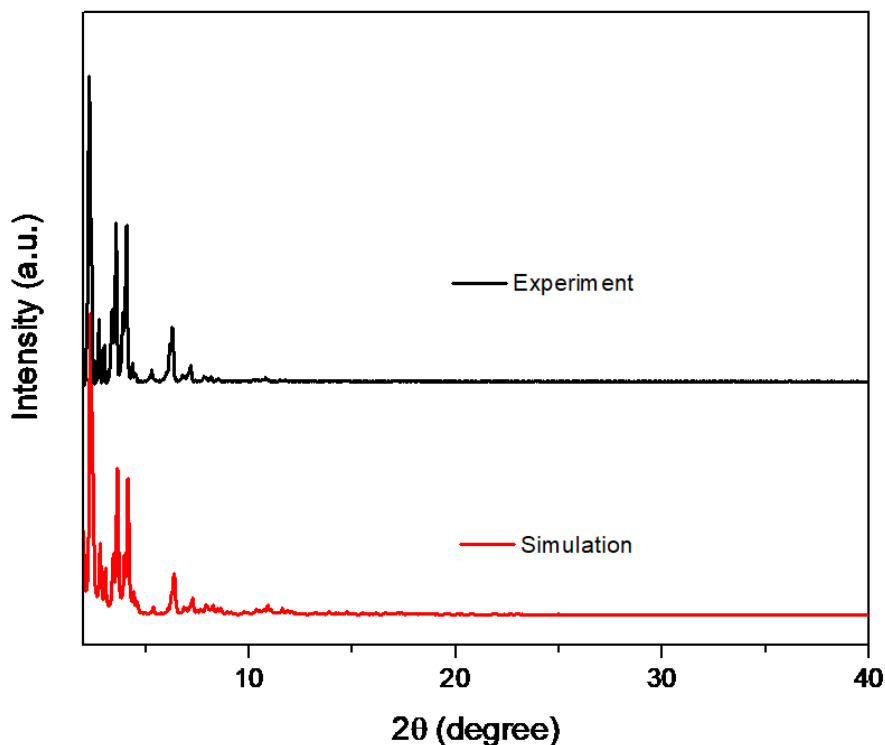


Figure IV-2. PXRD Patterns of PCN-604 based on simulation (red) and experiment (black).

4.3.2 Porosity Characterization of PCN-604

As PTB shares almost the same size with 4,4',4''-s-triazine-2,4,6- triyl-tribenzoic acid (TATB), the porosity of PCN-604 is close to that of PCN-333(Al). Instead of activation with supercritical CO₂, which is usually used to degas mesoporous MOFs, the as-synthesized PCN-604 can be activated in common way.^{25, 149} N₂ adsorption was performed at 77 K to determine the porosity of PCN-604 (Figure IV-3). The MOF shows 1952 cm³/g (STP) total N₂ uptake. The Brunauer–Emmett–Teller surface area and Langmuir surface area are 2633 m²/g and 3561 m²/g respectively. Two steep increases at P/P₀ = 0.35 and 0.5 on the N₂ adsorption isotherm correspond to the two types of mesoporous cages. The experimental pore volume is 3.2 cm³/g, slightly less than that of PCN-333 (3.85 cm³/g) (Table IV-1).

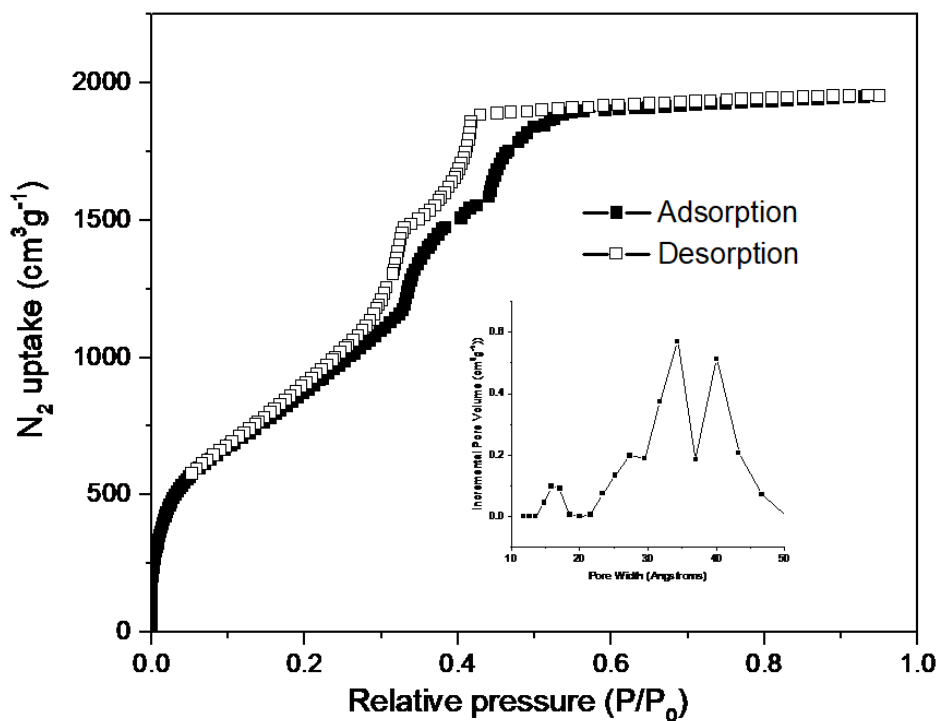


Figure IV-3. N₂ sorption isotherm of pristine PCN-604 at 77 K, atm. Insert shows the DFT pore size distribution.

Table IV-1. Porosity comparison between PCN-333 and PCN-604.

MOFs	N ₂ uptake(cm ³ /g)	Pore volume (cm ³ /g)	Surface areas (m ² /g)
PCN-333	2490	3.22	4000
PCN-604	1952	3.81	3561

4.3.3 Stability Characterization

Aqueous stability tests are also performed via water treatment. The as-activated samples are immersed into aqueous solutions with various pH values and are allowed to stay overnight.

PXRD patterns indicate that PCN-604 can survive in pure water and aqueous solutions with pH from 3 to 8 (Figure IV-4). The N₂ isotherms are also tested after water treatment. According to the N₂ isotherm, the crystallinity of PCN-604 slightly decreased after acid or base treatment, as the N₂ uptake reduced to 1698 cm³/g (Figure IV-5). Thermal stability of PCN-604 is determined by thermogravimetric analysis (TGA) (Figure IV-6). It shows that the decomposition temperature of PCN-604 is 540 °C and the three weight losses are corresponded to the departure of free solvent (up to 100 °C), coordinated solvent (230 °C) and combustion of the organic ligand (490 °C). The desired aqueous stability as well as the excellent thermal stability can be ascribed to the strong electrostatic interaction between the trivalent aluminium clusters and carboxylate linkers.

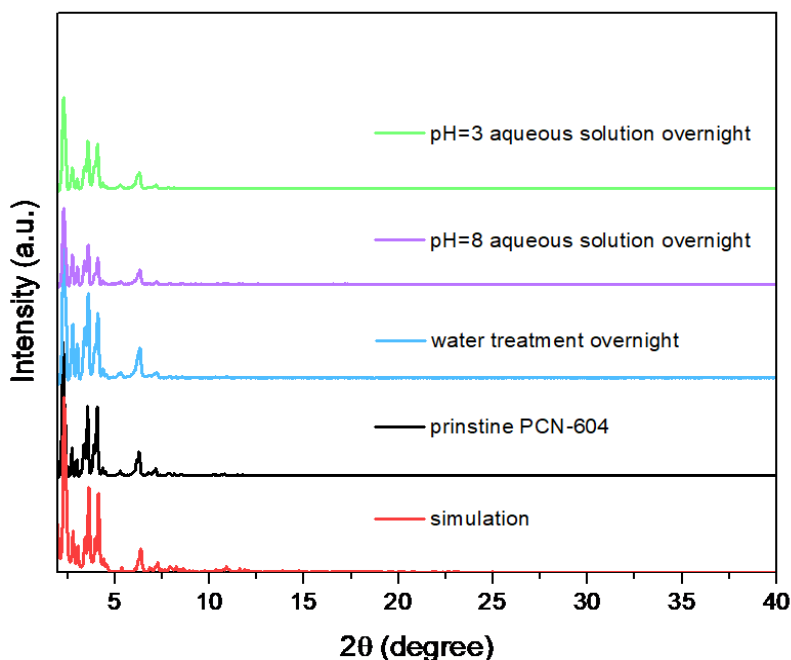


Figure IV-4. PXRD patterns of simulation PCN-604 (red), pristine PCN-604 (black), samples treated with water, pH = 8 aqueous solution (purple) and pH = 3 aqueous solution (green).

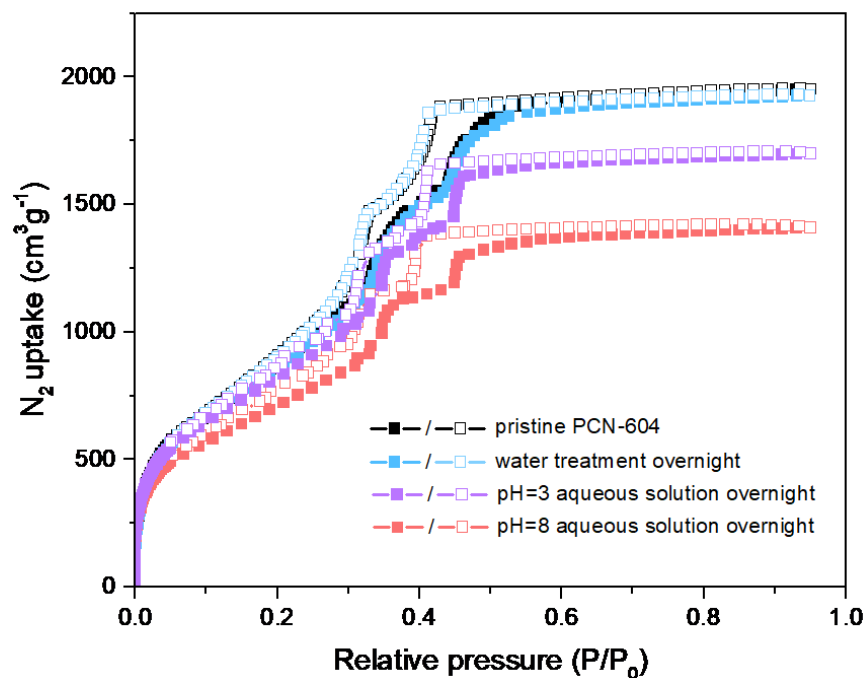


Figure IV-5. N₂ uptake isotherms of PCN-604 samples after treatment of aqueous solutions with different pH values.

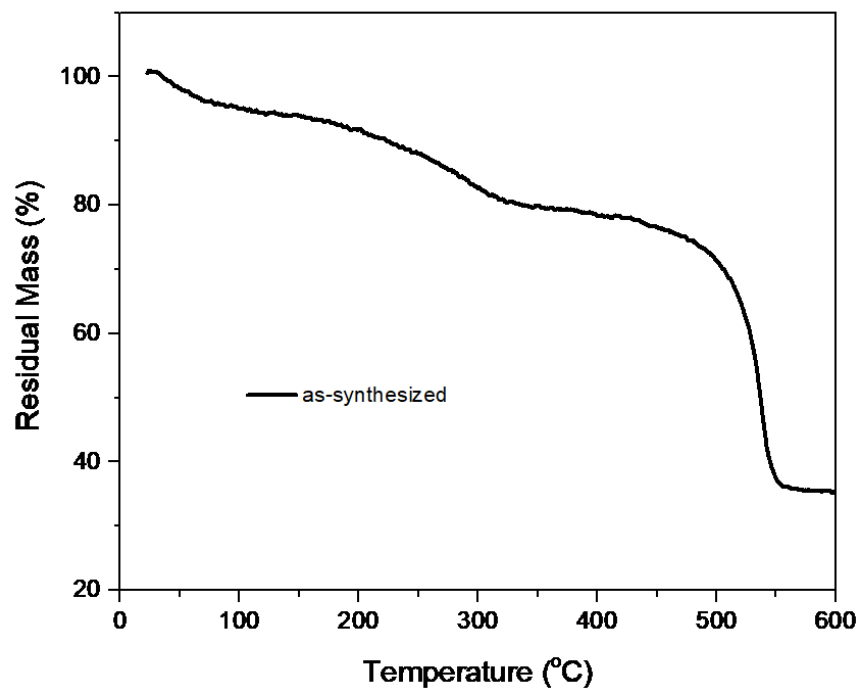


Figure IV-6. Thermogravimetric analysis of as-synthesized PCN-604.

4.3.4 Luminescence Properties

Considering that PCN-604 is built of Al^{3+} metal clusters with complete electron subshells and electron-rich π -conjugated ligands, the obtained network is supposed to be photoactive for further applications.¹⁵ The photoluminescence properties of both PCN-604 and its acid ligand H₃PTB in solid state were firstly explored at room temperature. According to the solid-state fluorescence spectra, the free acid ligand shows strong emission centered at 475 nm and 640 nm when excited at 424 nm, assigned to $\pi \rightarrow \pi^*$ and $n \rightarrow \pi^*$ transitions respectively (Figure IV-7); while PCN-604 cannot be fully excited at the same excitation wavelength, even though it displays similar emission profile compared to its acid ligand, exhibiting intense fluorescence emission with the maximum emission peak at 433 nm (Figure IV-8). The notable difference in fluorescence properties might be induced by ligand-to-metal charge transfer (LMCT) in the coordination material.²²⁹ The fluorescence properties of PCN-604 dispersed in different solvents are also investigated (Figure IV-9). The fluorescence spectra indicate trivial solvent effect of the MOF suspension in most organic solvents like acetone, DMF, THF, CH₃CN, MeOH, EtOH, CH₂Cl₂ displaying maximum emission peaks centered at 379 nm upon excitation of 350 nm. It should be pointed out that, compared with the spectra of other solvents, there is an additional shoulder peak at 423 nm in weak-polar solvent CH₂Cl₂, which might be caused by the pyridyl group.^{230 231} The shoulder emission disappears with the increasing of solvent polarity. When it comes to water, a broader emission occurs with a blue-shift of 10nm, demonstrating the existence of the hydrogen bond interactions between the H₂O molecules and organic ligands.²³²⁻²³³ Fluorescence lifetime of the MOF suspension was also measured, showing a multi-exponential decay. The amplitude-weighted average lifetime (τ_{av}) is calculated to be 5.33 ns.

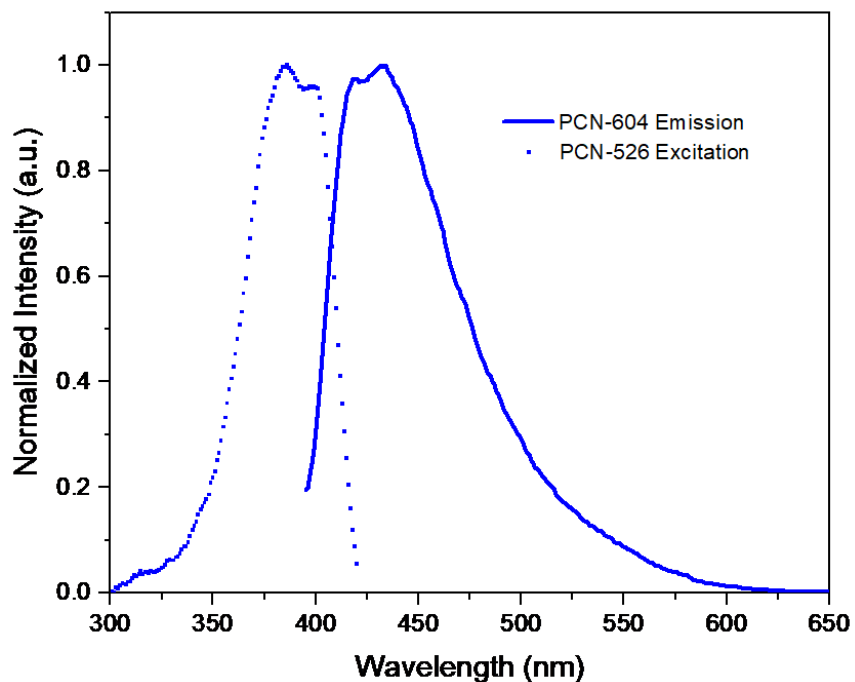


Figure IV-7. Solid-state excitation spectrum (blue dot) and emission spectrum (blue line) of PCN-604 at room temperature.

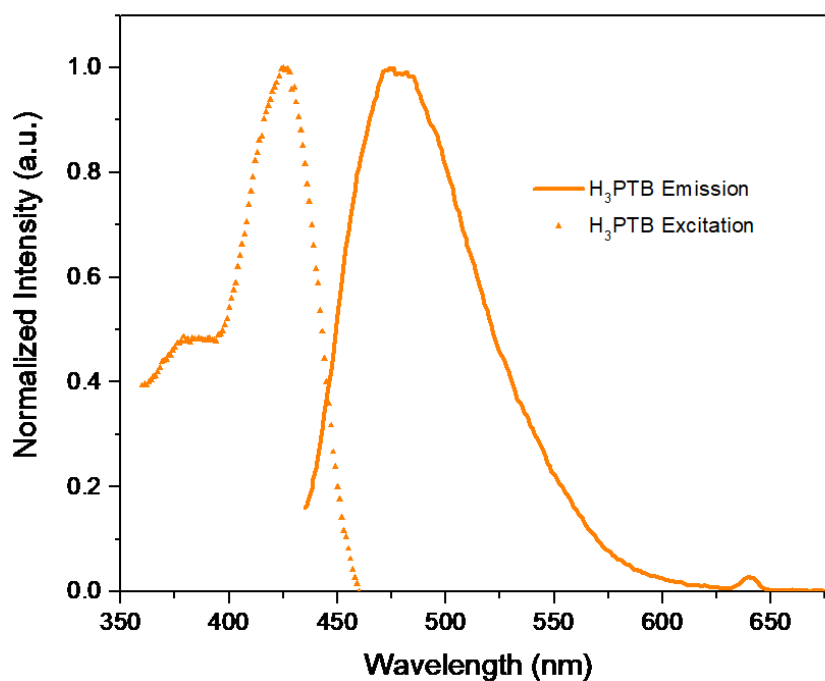


Figure IV-8. Solid-state excitation spectrum (yellow dot) and emission spectrum (yellow line) of H₃PTB at room temperature.

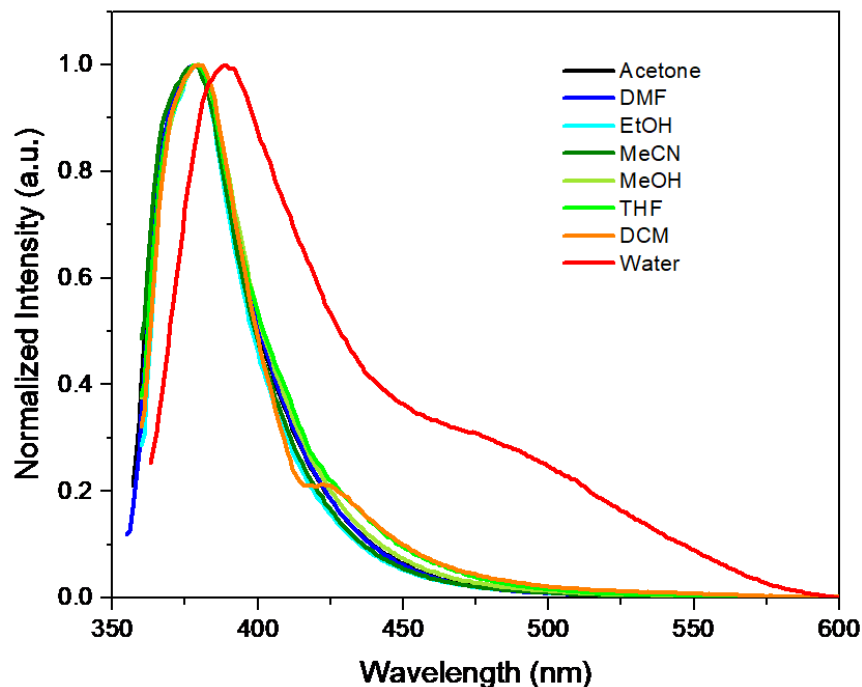


Figure IV-9. Emission spectra of PCN-604 suspensions dispersed in various solvents excited at 350 nm.

4.3.5 Sensing Measurements

Considering the desired chemical stability, fluorescence performance as well as the efficient pyridyl binding site of PCN-604, we investigated the sensing capability of the as-synthesized MOF towards various metal ions in water. 2 mg/mL aqueous suspensions of MOF powder were ultrasonically prepared and 1 mM aqueous solutions of fifteen different nitrate salts of metal cations, Na^+ , K^+ , Ag^+ , Mg^{2+} , Ca^{2+} , Mn^{2+} , Fe^{2+} , Co^{2+} , Ni^{2+} , Cu^{2+} , Zn^{2+} , Cd^{2+} , Al^{3+} , Cr^{3+} , Fe^{3+} , were added to the suspensions respectively. Fluorescence intensities of these suspensions before and after the additions of metal ions were all recorded at room temperature upon excitation at 350 nm and the quenching efficiencies were calculated and compared for qualitative studies of sensitivity. The metal ions exert different quenching effects on the fluorescence of PCN-604.

Among them, Fe^{3+} causes the highest fluorescence quenching in respect of emission intensities with the quenching efficiency of 74%; while others display either moderate or negligible quenching efficiencies (from 10% to 30%) (Figure IV-10). It is also worthy to note that the fluorescence quenching occurs within 1 min, a rapid response which might be due to intrinsic mesoporous structure of PCN-604 that allows the analyte to diffuse and interact the host network rapidly. The selectivity of PCN-604 for Fe^{3+} detection was also explored based on competitive experiments in the coexistence of other metal ions. 1 mL aqueous solution that contains various metal ions except for Fe^{3+} (1 mM for each) was introduced to 1 mL MOF suspension, leading to a decrease in fluorescence intensity by 18.6 %. The change is similar to that caused by the individual addition of these metal ions, indicating no accumulative quenching effects. Sequential addition of 1 mL aqueous solution of Fe^{3+} (1mM) to the suspension resulted in a dramatic fluorescent quenching by 64 %, which demonstrates that the sensing process is resistant to the interference of other metals. As a control experiment, the fluorescent intensities of the mixture of MOF suspension and deionized water were also tested and the presence of deionized water slightly lowered the intensity by 17.4 % due to the dilution of the original suspension (Figure IV-11).

To further validate the high sensitivity for Fe^{3+} detection, titration experiments were carried out with the concentration of Fe^{3+} ranging from 0 to 1000 μM . With the gradual addition of Fe^{3+} ion, the fluorescence intensity of the suspension was steadily quenched to the lowest point (Figure IV-12). The quenching constant (K_{sv}) was further calculated based on the Stern-Volmer (SV equation: $(I_0/I) = 1 + K_{sv}[M]$, where I_0 is the initial intensity, I is the intensities of the corresponding MOF suspensions varying with different concentrations of Fe^{3+} ($[M]$), and K_{sv} is the quenching constant (M^{-1}), which is an important indicator of sensing ability of a fluorescent sensor.²³⁰ It is shown that the SV-plot presents quiet a linear shape in the low concentration range and slightly

upper bends at high concentration level (Figure IV-13). k_{sv} value is calculated to be $8.53 \times 10^3 \text{ M}^{-1}$ based on the linear part and which is better, if not, comparable to previously reported MOF-based Fe^{3+} sensors (Table IV-2). The limit of detection (LOD) turns to be $6.2 \mu\text{M}$ calculated from the K_{sv} value and standard deviation S_b of three repeated fluorescence measurements of blank solutions ($3S_b/K_{sv}$). The large K_{sv} value and small LOD demonstrate the great feasibility of PCN-604 to serve as a fluorescent sensor for Fe^{3+} detection in aqueous system.

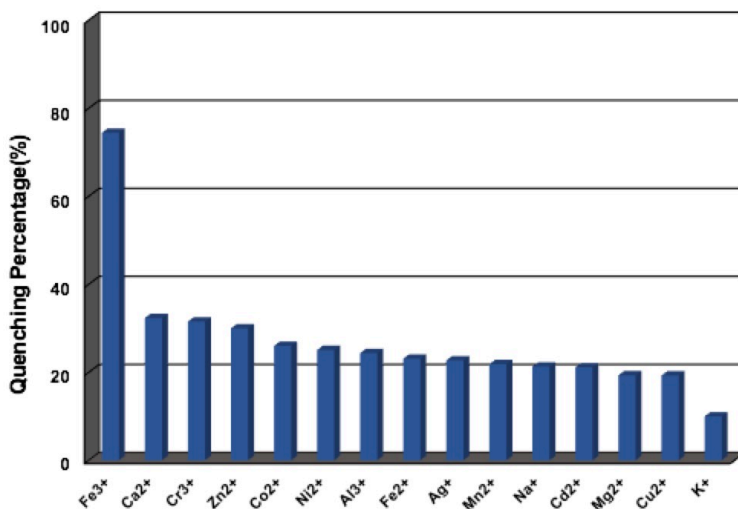


Figure IV-10. Fluorescence quenching of PCN-604 dispersed in aqueous solutions of fifteen different metal cations (1 mM). Excitation at 350 nm, room

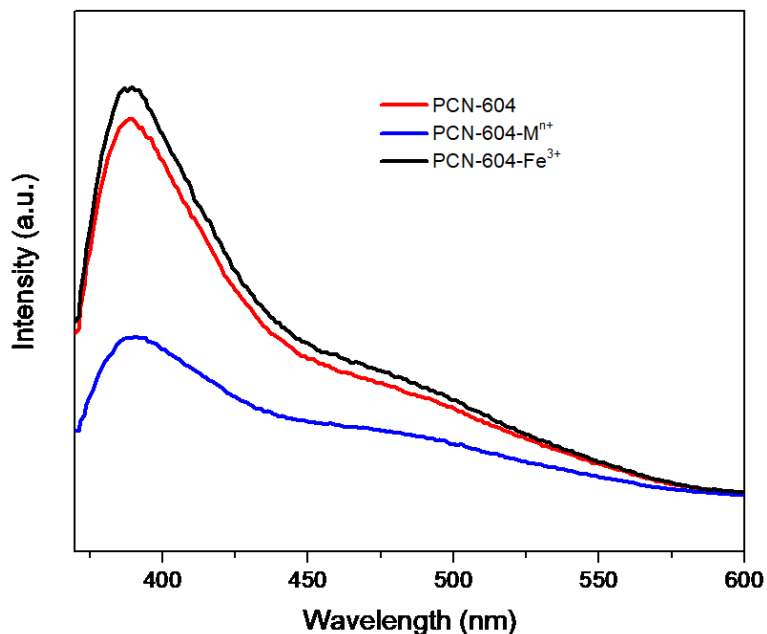


Figure IV-11. Fluorescent spectra of original PCN-604 suspension solution, upon addition of 1 mL of 14 metal ions (1 mM for each) and sequent addition of Fe³⁺(1mM).

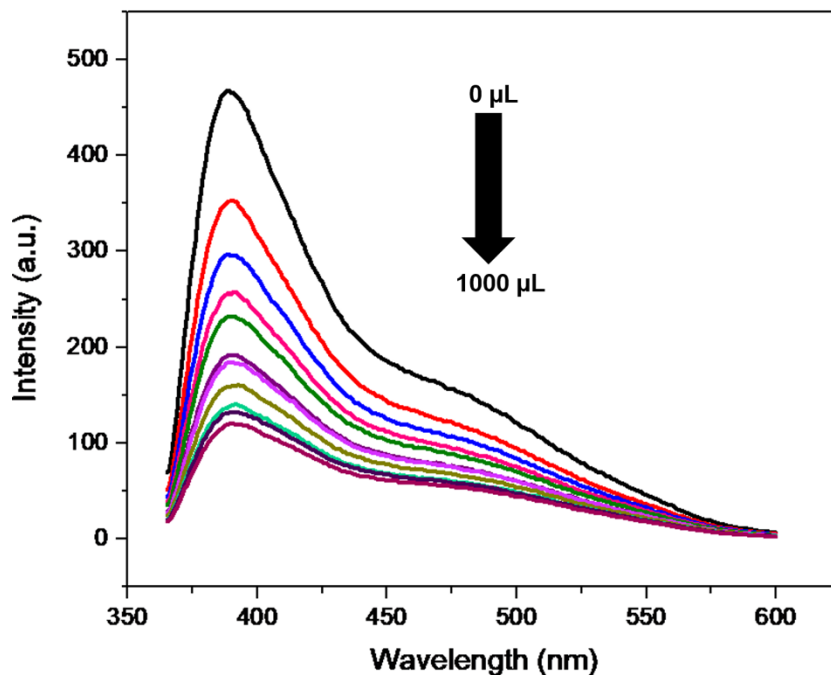


Figure IV-12. Fluorescence spectra of PCN-604 suspension in response to different concentrations of Fe³⁺. Fe³⁺ aqueous solution (1 mM) was added gradually from 20 μL to 1000 μL (20 μL each time).

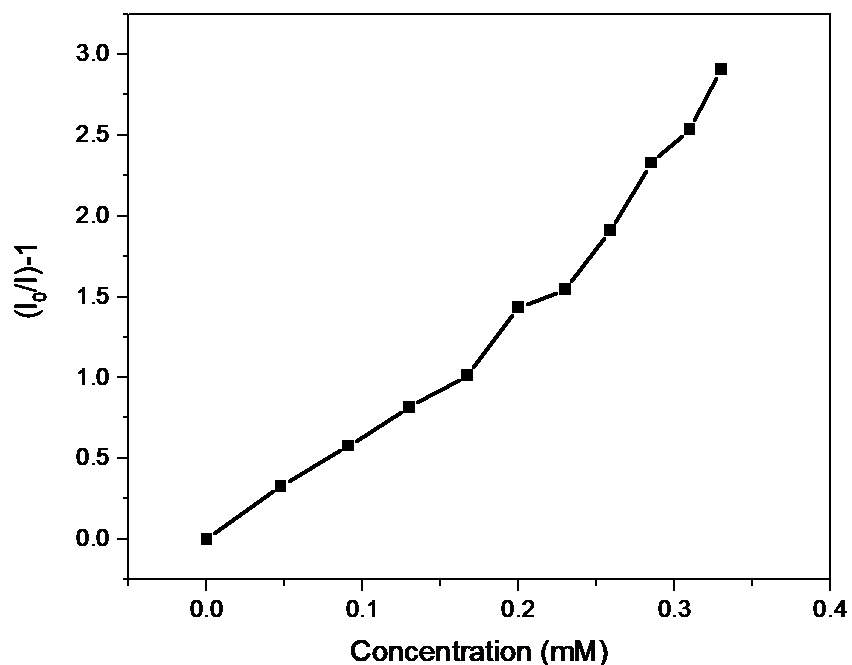


Figure IV-13. SV plot of PCN-604.

4.3.6 Sensing Mechanism

Several possible mechanisms have been well documented to explain the fluorescence quenching by Fe^{3+} ions including the collapse of the framework structure, ion exchange, host-and-guest interactions via fluorescence resonance energy transfer (FRET) or/ and photoinduced electron transfer (PET).²³⁴⁻²³⁶ The maintained crystallinity of PCN-604 after Fe^{3+} treatment is demonstrated by the PXRD patterns, which excludes the possibility of structural collapse. In addition, the rapid quenching effect (with several seconds) and the strong covalent bonds formed between the high valent Al^{3+} clusters and carboxylate groups can, to some extent, rule out the ion exchange between the externally induced Fe^{3+} and the framework, which is time-consuming and kinetic-driven. Hence, one can propose that the main mechanism for the fluorescence quenching effect is the host-guest interaction. With the unsaturated 3d orbital ($3d^5 4s^0$), the highly charged Fe^{3+} is a better electron acceptor compared to other cations; meanwhile, the organic linkers with

conjugated moieties turn out to be good electron donors. Herein, the quenching effect is likely to originate from the photoinduced electron transfer (PET). Upon excitation, the excited electrons are proposed to be transferred to the lowest unoccupied molecular orbital (LUMO) of Fe^{3+} . The process leads to nonradiative pathway and is competitive to radiative LMTC within the framework, impeding the fluorescence of the MOF.

Moreover, the N atoms on the pyridine groups of the organic linkers can donate their lone-pair electrons to the metal ion, enhancing the interactions between the targeted analytes and the host material. As a result, the fluorescence quenching is triggered. It is also reasonable that the sensing mechanism underlies the distance-dependent fluorescence resonance energy transfer (FRET). In order to prove it, the adsorption spectra of various metal ions were collected. The absorption of Fe^{3+} has the largest degree of overlapping with the emission of PCN-604, making the energy transfer feasible. The overlap for other metal ions is negligible and is in good agreement with the trend of quenching efficiency (Figure IV-14).

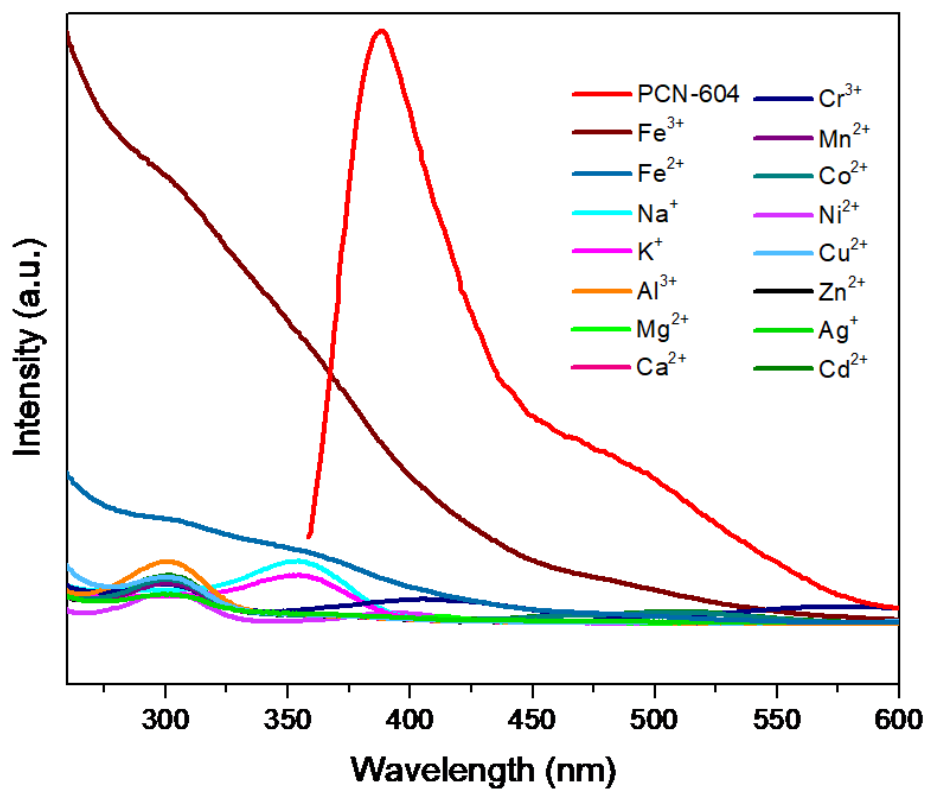


Figure IV-14. Emission spectrum of PCN-604 aqueous suspension (red) and adsorption spectra of different metal ions solutions in the concentration of 1mM.

Table IV-2. Comparison of sensing performance of PCN-604 for Fe³⁺ ion with other MOF-based materials.

Materials	Solvent	K _{sv} (M ⁻¹)	Detection limit (μM)	Ref.
BUT-14	water	2.17 × 10 ³	3.8	230
BUT-15	water	1.66 × 10 ⁴	0.8	230
Eu ³⁺ @MIL-53-COOH (Al)	water	5.12 × 10 ³	0.5	237
MIL-53 (Al)	water	—	0.9	229
Gd ₆ (L) ₃ (HL) ₂ (H ₂ O) ₁₀ (L = 5,5' -(pyridine-2,5-diyl)isophthalate)	water	7.89 × 10 ²	-	238
Cd-MDIP	water	4.13 × 10 ⁴	0.08	239
EuOHDC	water	—	1.17	240
[(CH ₃) ₂ NH ₂][Tb(bptc)]	ethanol	—	180.1	241
Eu ₂ (MFDA) ₂ (HCOO) ₂ (H ₂ O) ₆	DMF	1.58 × 10 ³	0.3	242
(Me ₂ NH ₂)[Tb(OBA) ₂](Hatz)·(H ₂ O) _{1.5}	water	3.4 × 10 ⁴	-	243
PCN-604	water	8.53 × 10 ³	6.2	this work

4.4 Conclusion

To conclude, we successfully synthesized a novel mesoporous MOF, PCN-604, from pre-designed functional organic linkers through direct synthesis method. PCN-604 is constructed from trimetric aluminium clusters and 4,4',4''-(pyridine-2,4,6-triyl)tribenzoic acid (H₃PTB). The crystallinity and porosity of the MOF are confirmed by the powder X-ray diffraction combined with N₂ isotherms. The stability of PCN-604 is evaluated through water treatments and thermogravimetric analysis (TGA), showing that the material can sustain its crystallinity in the aqueous solutions with pH in the range of 3-8 and will not decompose below 540 °C. Fluorescence properties of the MOF in both solid state and solutions are explored based on the excitation and emission spectra as well as fluorescent lifetime showing the material displays good emission in water. Notably, the fluorescence of PCN-604 can be quenched rapidly within seconds by the aqueous solution of Fe³⁺. The rapid quenching process can be ascribed to the mesoporous cavities of the network that can pre-concentrate the analytes and hinder the diffusion constrains. The quenching efficiency of Fe³⁺ is 74%, the highest one compared to those of other metal cations. Moreover, verified by the quenching testes and titration experiments, PCN-604 possesses satisfactory sensitivity and selectivity indicated by the large quenching constant and detection limit, $8.53 \times 10^3 \text{ M}^{-1}$ and 6.2 μM, respectively. To have a deep look, the good sensing performance is driven by the host-guest interactions involving fluorescence resonance energy transfer (FRET) or/ and photoinduced electron transfer (PET) and the intrinsic electron-donating pyridine groups on the linker also plays an essential rule during the sensing process.

CHAPTER V

AGGREGATION TO THE BEST: A 9-CONNECTED ZIRCONIUM MOF WITH TRIPHENYLENE-BASED HEXATOPIC LINKER

5.1 Introduction

Organic luminogens have attracted extensive interest in the past decades because of their promising applications in the fields of optical and electronic devices, organic light emitting diodes (OLEDs), photovoltaic cells, luminescent sensors, etc.²⁴⁴⁻²⁴⁵ Conventional design of organic luminophores often involves embedding highly conjugated chromophores on the structures, which indeed improves the luminescence. However, the extent of π -conjugation would increase the tendency of π - π stacking, leading to the detrimental aggregation-caused quenching (ACQ) effect in concentrated or solidified phases.²⁴⁶ To alleviate ACQ, one effective strategy is to block the undesired aggregation through attachment of alicyclics, wrapping by surfactants, blending with polymers, etc.²⁴⁷⁻²⁴⁹ These years, the appearance of luminogens featured with aggregation-induced emission (AIE or AIEE), of which the photoluminescence efficiency is higher in solid state than in solutions, makes it possible to take the intrinsic advantage of aggregation.²⁵⁰⁻²⁵² Most AIE luminogens contain freely-rotating substituents and AIE effect mechanically originates from restriction of non-radiative intramolecular rotation or vibration of these rotors. Keep this in mind, traditional ACQ compounds are likely to be AIE-active through structural modification.²⁵³⁻²⁵⁵

Metal-organic frameworks (MOFs) are a newly emerging class of porous inorganic-organic hybrid materials with high crystallinity, permanent porosity as well as structural and functional diversity.²⁵⁶⁻²⁵⁷ Serving as building blocks of MOFs, a variety of carboxylate or pyridine functionalized organic luminophores have been integrated into the coordinated networks, bringing

special photophysical properties and applications.^{15, 93, 101, 258} The AIE mechanisms underlying MOF systems have been comprehensively studied based upon several luminescent MOFs constructed by AIE luminogens, especially tetraphenylethylene (TPE) analogues.²⁵⁹⁻²⁶⁰ It has been shown that on the contrary of non-covalent closed packing of small molecules, MOFs can restrict intramolecular motions and turn on the luminescence of luminogens through metal-linker coordinating bonds in solid state, namely, matrix coordination-induced emission effect (MCIE).²⁶¹ In addition, the well-designed structures of MOFs also impart the fixed organic compounds with long intermolecular separation, which can efficiently block intermolecular quenching, leading to enhancement of luminescence efficiency.²⁶²⁻²⁶⁵

Triphenylene is an iconic disco-like compound with large tendency to undergo luminescence-quenched H-aggregates.²⁶⁶⁻²⁶⁷ To avoid the undesired π - π stacking, people turned to structural embellishment,²⁶⁸⁻²⁷⁰ meanwhile, achieved the AIE-activity of triphenylene-based derivatives.^{269, 271} Nevertheless, the structural decoration of triphenylene core often requires introduction of bulky side groups, which is synthetically consuming. Moreover, as the corresponding aggregates are usually utilized as chemical sensors, the relative low luminescent efficiency, amorphous, if not, low-ordered organization, lack of porosity as well as solvent-dependent assembly conditions extremely limit their sensing performance.²⁴⁴ With these concerns, we sought to take advantages of MOFs to achieve ‘the best aggregation’ of triphenylene derivatives in terms of luminescence performance via ligand immobilization. We successfully synthesized a novel stable Zr-based MOF built from 4,4',4'',4''',4''''-(triphenylene-2,3,6,7,10,11-hexayl)hexabenzonic acid (H₆TPHB) and 9-connected Zr₆ clusters, namely, PCN-811. In PCN-811, desired orientation of the linker is formed where triphenylene cores are separated to long distance. The six phenyl-carboxylate groups on the linkers not only serve as coordinating

sites to metal clusters but also endow the MOF with AIEE feature through RIM mechanism.²⁵⁹ As a result, the generated MOF exhibits a remarkable increase of luminescence efficiency, especially quantum yield, in comparison with the free triphenylene-based ligand. Moreover, the synthesized material exhibit record-high sensing sensitivity towards 2,4,6-trinitrophenol (TNP) in aqueous media.

5.2 Experimental Section

5.2.1 Materials and Instrumentation

Materials

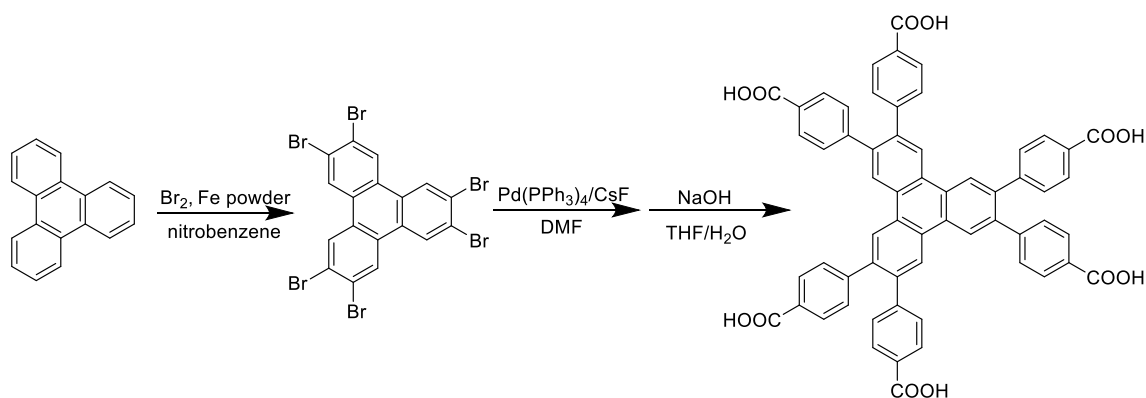
Triphenylene, bromine, N, N-dimethylformamide (DMF), zirconium(IV) chloride, 4-methoxycarbonylphenylboronic acid, tetrakis(triphenylphosphine) palladium were purchased from either VWR or Sigma Aldrich. Unless otherwise noted, all commercial chemicals were used without further purification.

Instrumentation

Synchrotron powder X-ray diffraction (PXRD) was carried out with Bruker D8-Discover diffractometer equipped with a Mo sealed tube ($\lambda = 0.72768 \text{ \AA}$) on the beamline 17-BM at the Advanced Photon Source, Argonne National Laboratory. In-house powder X-ray diffraction (PXRD) was carried out on a Bruker D8-Focus Bragg-Brentano X-ray powder diffractometer equipped with a Cu sealed tube ($\lambda = 0.72768 \text{ \AA}$) at 40 KV and 40 mA. Single crystal X-ray diffraction experiments were carried out on a Bruker D8-Venture or D8 Quest diffractometer equipped with a Mo-K α sealed-tube X-ray source ($\lambda = 0.71073 \text{ \AA}$, graphite monochromated) at low temperature device (100 K). Continuous rotation electron diffraction (RED) were collected using the software *cREDCollection* on a JEOL JEM2100 LaB₆ TEM at 200 KV. UV-Vis spectra

were recorded on Shimadzu UV-2450 spectrophotometer. Fluorescence spectra were collected on Horiba Fluorolog spectrometer. Thermogravimetric analyses (TGA) were carried out on a Shimadzu TGA-50 thermal analyzer from temperature to 600 °C at a ramp rate of 5 °C /min in a flowing air atmosphere. Nuclear magnetic resonance (NMR) data were collected on a Mercury 300 spectrometer. Low pressure gas adsorption measurements were performed on an ASAP 2020 with the extra-pure quality gases.

5.2.2 Synthesis of Linker



Scheme V-1. Synthesis of H₆TPHB.

Step 1. Synthesis of 2,3,6,7,10,11-Hexabromotriphenylene

In a 250 mL round-bottom flask, triphenylene (3.87 g, 17 mmol) and iron powder (0.387g, 7.74 mmol) was added in 155mL dry nitrobenzene and 7.74 mL bromide was added dropwise over 5 min. The mixture was stirred at room temperature overnight and then heated under reflux at 209 °C for another 2 hours. After cooling to room temperature, the precipitate was filtered and washed with diethyl ether three times. The resulting solid was then recrystallized in 1,2-dichlorobenzene to afford pale grey product (8.4 g, 12mmol, 71%). As the gained product is hardly dissolved in

regular deuterium solvents, it is directly used for next step without further characterization.

Step 2. Synthesis of Hexamethyl 4,4',4'',4''',4''''',4''''''-(triphenylene-2,3,6,7,10,11-hexayl)hexabenzoate (Me₆TPHB)

Synthesized 2,3,6,7,10,11-Hexabromotriphenylene (4 g, 5.7 mmol), 4-methoxycarbonylphenylboronic acid (7.38 g, 41.04 mmol), K₂CO₃ (5.7 g, 41.04 mmol), Pd(PPh₃)₄ (1.97 g, 1.71 mmol) were added into a 500 ml three-necked flask. The flask was fitted on the Schlenk line, vacuumed and refilled with nitrogen alternately three time. A mixing solvent (toluene/1,4-dioxane/methanol: 120mL/75mL/75mL) was bubbled with nitrogen for 30 min and then transferred to the flask through a canula. The mixture was allowed to react for 48 hours at 85 °C. After cooling to the room temperature, the reaction mixture was poured into a large amount of water, and extracted with chloroform three times. The combined organic part was dried with magnesium sulfate and the solvent was removed under vacuum. The solid residue was then purified by column chromatography (eluent from CHCl₃: hexane = 7:3 to CHCl₃: EtOAc =19:1) to afford pale yellow solid (4.5 g, 4.37 mmol, 76%). ¹H NMR (300 MHz, CDCl₃): δ 8.73 (s, 6H), 7.97 (d, *J* = 8.3 Hz, 12H), 7.38 (d, *J* = 8.4 Hz, 12H), 3.92 (s, 18H).

Step 3. 4,4',4'',4''',4''''',4''''''-(triphenylene-2,3,6,7,10,11-hexayl)hexabenzoic acid (H₆TPHB)

Me₆TPHB (4.5g, 4.37 mmol) and potassium hydroxide (2.4 g, 43.7 mmol) were added into a mixture of THF/methanol/water (v/v/v=100mL/100mL/100mL) and was refluxed overnight. After cooling, the organic solvent was removed and the aqueous phase was acidified with 6M hydrochloric acid to give pale yellow precipitate, which was then washed with water several times and dried under vacuum (3.7 g, 3.9 mmol, 90%). ¹H NMR (300 MHz, dmsO) δ 9.01 (s, 6H), 7.82 (s, 12H), 7.45 (s, 12H).

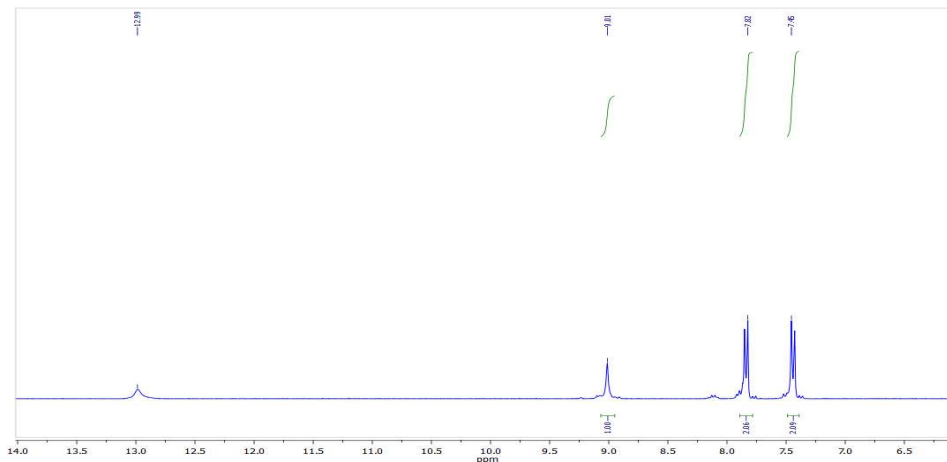


Figure V-1. ^1H NMR spectrum of H_6TPHB .

5.2.3 Synthesis of PCN-811

Powder PCN-811

In a 4 mL Pyrex vial, ZrCl_4 (11 mg, 0.047 mmol), H_6TPHB (10 mg, 0.010 mmol) and 210 μL trifluoroacetic acid (TFA) were ultrasonically dissolved in 3 mL N, N-dimethylformamide (DMF). The mixture was then heated in a 120 $^\circ\text{C}$ oven for 3 days to afford white crystalline powder (10 mg, yield based on ligand).

Single Crystal PCN-811

H_6TPHB (0.03 mmol, 24.4 mg) and $\text{ZrOCl}_2 \cdot 8\text{H}_2\text{O}$ (0.12 mmol, 39.0 mg) were ultrasonically dissolved in 8 mL of DMF in a 20 mL pyrex vial, and then 3.2 mL of formic acid was added and sealed. The reaction system was heated at 120 $^\circ\text{C}$ for 48 h in an oven.

5.2.4 Rotation Electron Diffraction (RED) and PXRD refinement

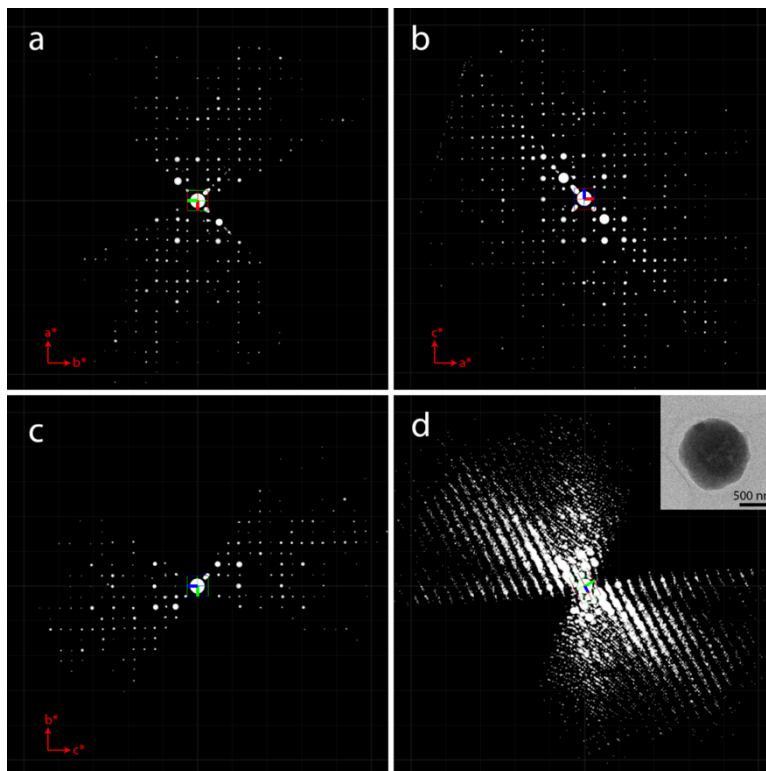


Figure V-2. 2D slices cut from the reconstructed 3D reciprocal lattice of PCN-811 show the (a) $hk0$, (b) $h0l$, and (c) $0kl$ plane. (d) Reconstructed 3D reciprocal lattice of PCN-811. Insert is the crystal from which the RED data was collected.

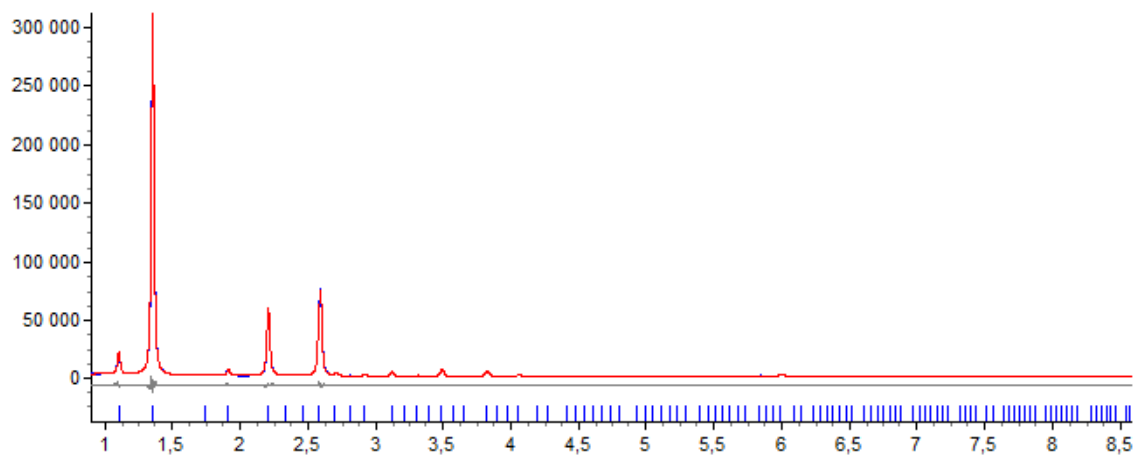


Figure V-3. Powley fit of powder X-ray diffraction for PCN-811 using space group $P4_132$. The curves are simulated (red), observed (blue), and difference profiles (gray), respectively; the bars below curves indicate peak positions.

5.2.5 N₂ Sorption Isotherm

Freshly synthesized samples (~ 50 mg) was washed with DMF two times and immersed in acetone for three days, during which the solvent part was decanted and freshly replenished with acetone three times. Afterwards, the samples were dried under vacuum, transferred into BET tube and then activated by the ‘outgas’ function of Micrometricity ASAP 2020 system for 10 hours at 100°C before the gas sorption measurement by the instrument.

5.3 Results and Discussion

5.3.1 Structural Description of PCN-811

With the aid of connecting diversity of zirconium clusters, desired orientation of the linker is formed in the framework where triphenylene cores are separated to long distance. PCN-811 crystallizes in cubic $P4_332$ space group, constructed by Zr_6 clusters and TPHB linkers. In the structure, the Zr_6 cluster adopts a C_3 symmetry. Each cluster is connected by nine linkers with three carboxylate groups coordinating in monodentate mode. Spindle-shaped supramolecular cage is formed with six TPHB linkers covering the faces and sixteen metal clusters occupying the vertices. The internal pore size is 1.6×3.4 nm. Such cages are connected with each other through sharing the faces and vertices of the cage to form a 3D framework with small open channels.²⁷²

The porosity of PCN-811 is confirmed by N₂ isotherm uptake at 77k. After solvent-exchanged with acetone several times, the white powder was further activated through the ‘degas’ function of the adsorption instrument for 5 h at 100 °C. The resulted N₂ sorption isotherm reveals a characteristic Type I behavior, indicating the microporous nature of the MOF structure. The measured Brunauer-Emmett-Teller (BET) surface area, Langmuir surface area and pore volume

are $1622.22 \text{ m}^2 \text{ g}^{-1}$, $1829.06 \text{ m}^2 \text{ g}^{-1}$ and $0.65 \text{ cm}^3/\text{g}$ respectively. The pore size distribution shows the cavity diameter is around 12 \AA (Figure V-4 & 5).

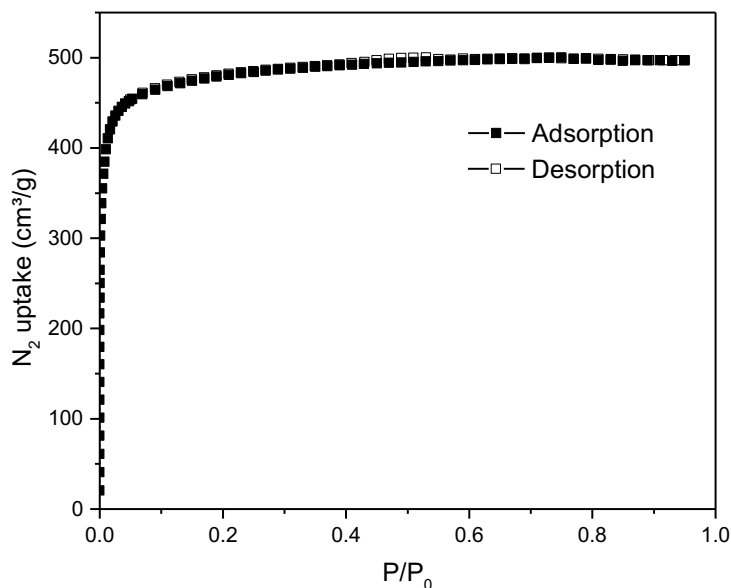


Figure V-4. N₂ sorption isotherm for PCN-811 at 77K, 1 atm.

5.3.2 Chemical and Thermal Stability Analysis of PCN-811

Powder X-ray diffraction pattern (PXRD) results demonstrate that PCN-811 stays intact in aqueous media with various pH values ranging from 2 to 12 at room temperature. N₂ isotherm measurements of the water-treated samples are also performed, which display minimal deviation from the pristine one (Figure V-6 & 7). Furthermore, the thermal gravimetric analysis (TGA) shows that PCN-811 is thermally stable up to 490°C (Figure V-8). The excellent stability can be ascribed to the hydrophobic triphenylene core on the backbones as well as the strong coordination bonds between the high oxidation state Zr^{4+} clusters and the hexatopic linker in a 12-connecting mode.

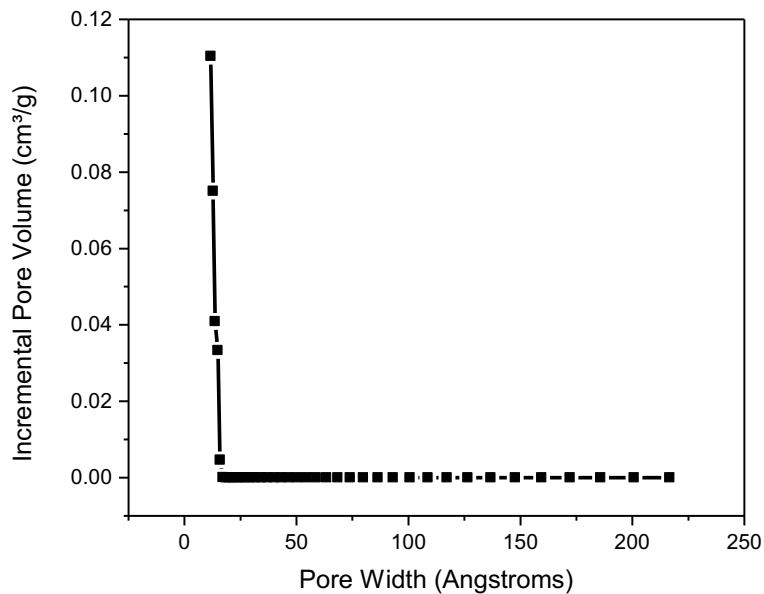


Figure V-5. DFT pore size distribution for PCN-811 derived by N₂ isotherm measured at 77 K, 1 atm.

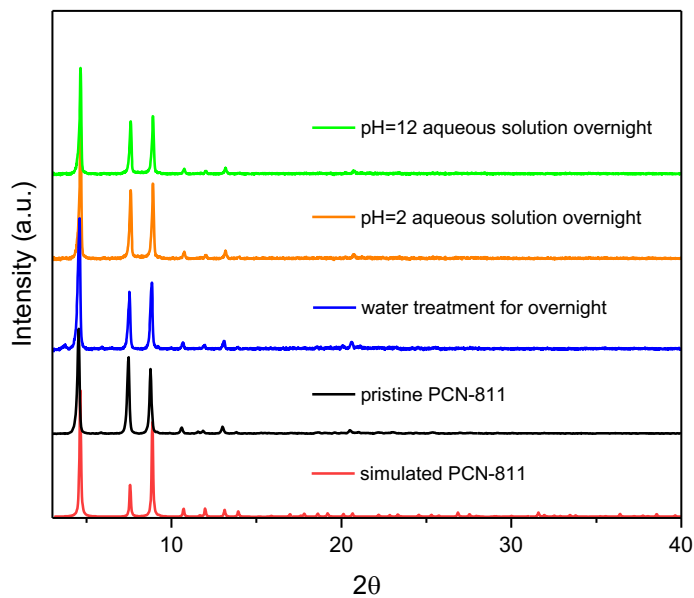


Figure V-6. PXRD patterns of PCN-822 after treatment of aqueous solutions with different pH values.

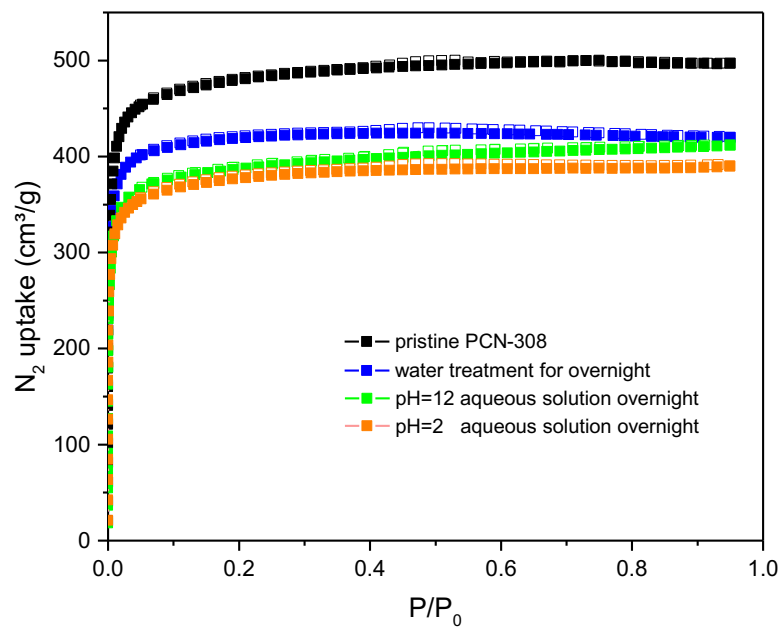


Figure V-7. N₂ isotherms after treatment of aqueous solutions.

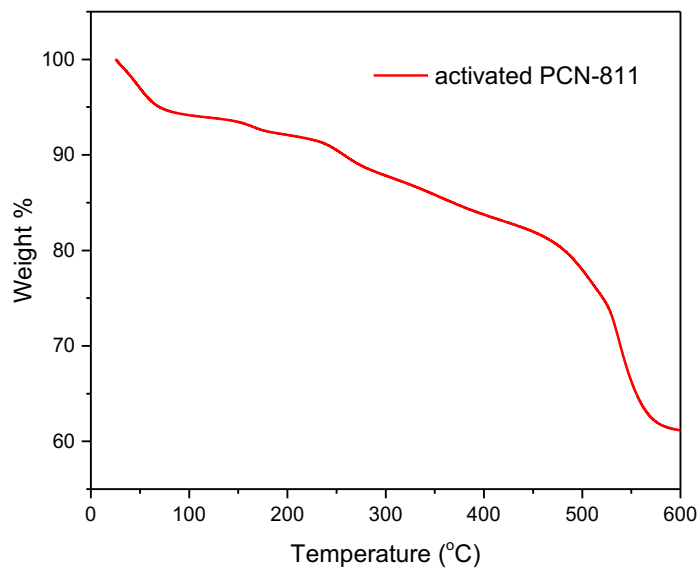


Figure V-8. Thermogravimetric analysis of activated PCN-811. 5.4 % weight loss at the beginning is due to the water molecules on the Zr₆. The decomposition temperature is around 490 °C based on calculation.

5.3.3 Photophysical Properties of PCN-811

H₆TPHB exhibits aggregation induced enhanced emission (AIEE) demonstrated by monitoring the photoluminescence (PL) spectra of the compound in the mixture THF/water solutions (10 μM) (Figure V-9). H₆TPHB shows weak emission centered at 394 nm in the pure THF solution. The PL intensity rises by 4.2-fold when the volume fraction of the water steadily increases up to 25% (absolute quantum efficiency, $\Phi = 10\%$). The enhancement marks the formation of fluorescent aggregates, which activates the restriction of intramolecular motion (RIM) process probably through intermolecular hydrogen bonds. Further addition of water to the mixture up to 99% leads to a sharp decrease in the PL intensity along with a red-shift of emission maximum to 421 nm. The dramatic change in PL might be ascribed to twisted intramolecular charge transfer (TICT). The electron-withdrawing carboxylate groups at the periphery cause a donor-acceptor system with the triphenylene core, which tends to undergo structural twisting in more polar solvents, annihilating its excited states non-radiatively.²⁷³

It has been revealed that the luminescence behaviors of the carboxylate-functioned linker are different from its free form after anchored on MOFs (Figure V-10). Upon excitation at 370 nm, H₆TPHB shows a broad emission spectrum with a maximum peak at 412 nm and a shoulder peak at 449 nm. The emission is mainly associated with the typical π - π^* transition of conjugated triphenylene cores and the additional bathochromic peak confirms the existence of intramolecular charge transfer (ICT), which often leads to the decrease in photoluminescence intensity or quantum yield.²⁷⁴ Like its organic building block, PCN-811 also emits blue light with an emission maximum at 408 nm. The small shift in emission energy (4 nm) and similar emission profile indicate the ligand-based nature of the luminescence. However, the absolute quantum yield of PCN-811 is 38%, a more than 4-fold enhancement compared to that of free H₆TPHB (9%). The great increase in

quantum yield can be contributed to the confinement effect of MOF backbones, which efficiently impedes the nonradiative molecular vibration or rotation processes.^{119, 275} Moreover, the judiciously designed framework successfully separates triphenylene cores into a long distance of 11.67 Å, which consequently blocks the energy transfer between adjacent triphenylene cores. The ICT is also inhibited in MOF system, demonstrated by the disappearance of the shoulder peak in emission spectrum.

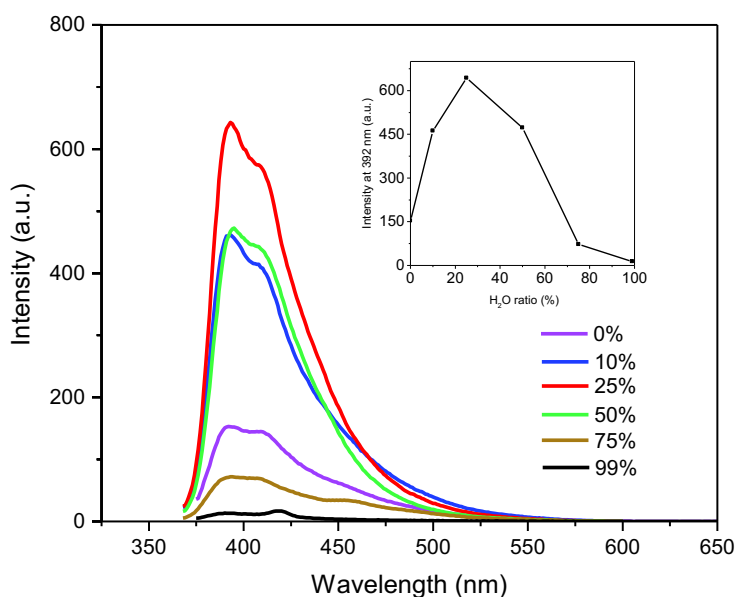


Figure V-9. Photoluminescence spectra of H₆TPHB in the mixture of THF/water solutions with different ratio.

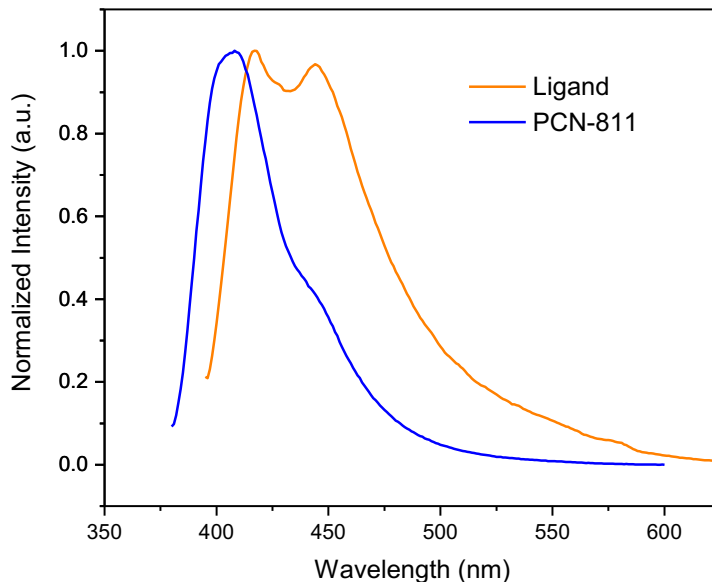


Figure V-10. Solid-state photoluminescence spectra of PCN-811 (blue) and H₆TPHB (yellow) upon excitation at 370 nm at room temperature.

5.3.4 Detection of Selected Explosives

The distinguished aqueous stability, enhanced PL as well as the electron-rich nature of triphenylene core force us to study the sensing capability of PCN-811 towards selected electron-deficient nitro-aromatic or nitro-aliphatic explosives, a major threat to civilian society and environment, especially in soil or groundwater of war zone.²⁷⁶⁻²⁷⁷ The activated MOF powders were homogeneously suspended in water ($\sim 0.11 \text{ mg mL}^{-1}$) and fluorescence quenching titrations were performed by gradually adding aqueous solutions of the corresponding analytes to the MOF suspension (1 Mm, 20 μL per time). According to the fluorescence spectra, PCN-811 displays the fastest and highest sensitivity towards 2,4,6-trinitrophenol (TNP) (Figure V-11-15). Fluorescence quenching takes place in response to trace amount of TNP with a concentration of 0.6 μM and the

quenching percentage reaches to 99.8% at the concentration of 0.085 Mm(Figure V-11). Through Stern-Volmer (SV) equation: $(I_0/I) = 1 + K_{sv}[Q]$, where K_{sv} is the quenching constant (M^{-1}), $[Q]$ is the molar concentration of the analyte, I_0 and I are the fluorescence intensities before and after addition of the analytes, we were able to quantitatively evaluate the quenching efficiency of PCN-811. The SV plot for TNP is nearly linear at lower concentration ranging from 0.6 μ M to 8 μ M, while it loses linearity and sharply bends upwards at higher concentrations (Figure V-11, insert). This might be ascribed to the existence of self-absorption or the synergistic effect of both electron and energy transfer between TNP and the MOF.²⁷⁸⁻²⁸⁰ The calculated quenching constant K_{sv} in linear range is $3.1 \times 10^6 M^{-1}$, which is one order of magnitude higher than those of previously reported MOF-based TNP sensors performing in water system. The calculated detection limit ($3S_b/K_{sv}$) is 2.3 ppb. It is worth noticing that the sensing ability of PCN-811 is greater, if not, comparable to most traditional organic polymers.

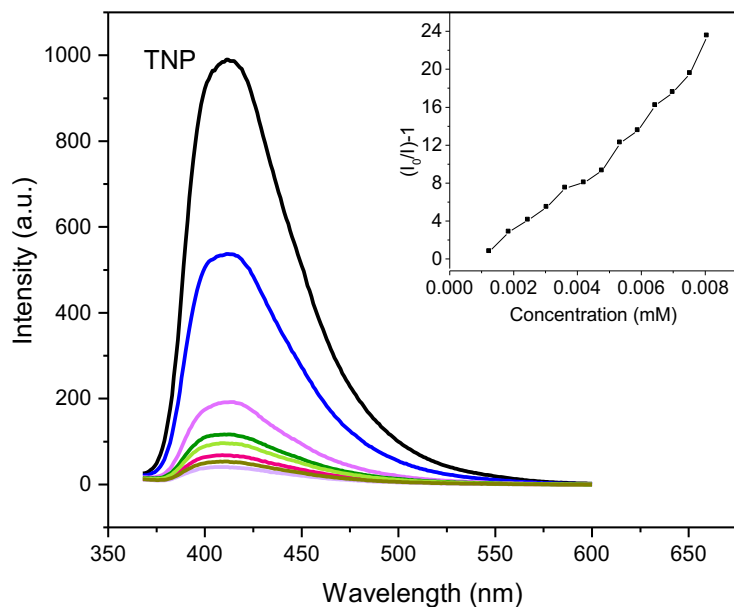


Figure V-11. Luminescence quenching spectra of PCN-811 suspension towards TNP. Insert shows Stern-Volmer plots towards TNP.

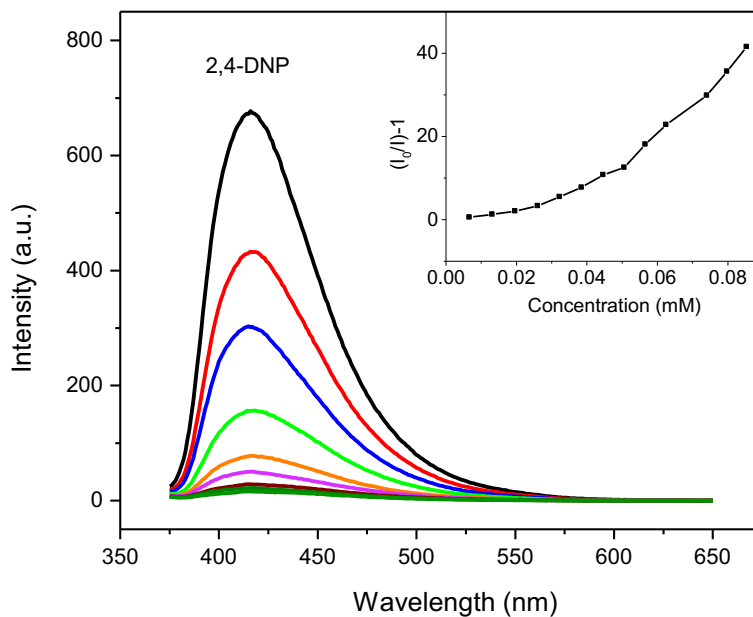


Figure V-12. Luminescence quenching spectra of PCN-811 suspension towards 2,4-DNP.

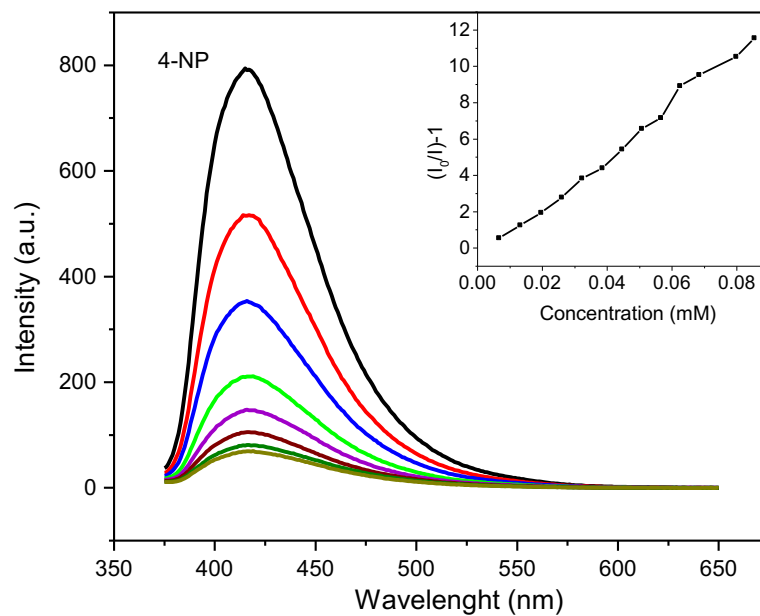


Figure V-13. Luminescence quenching spectra of PCN-811 suspension towards 4-NP.

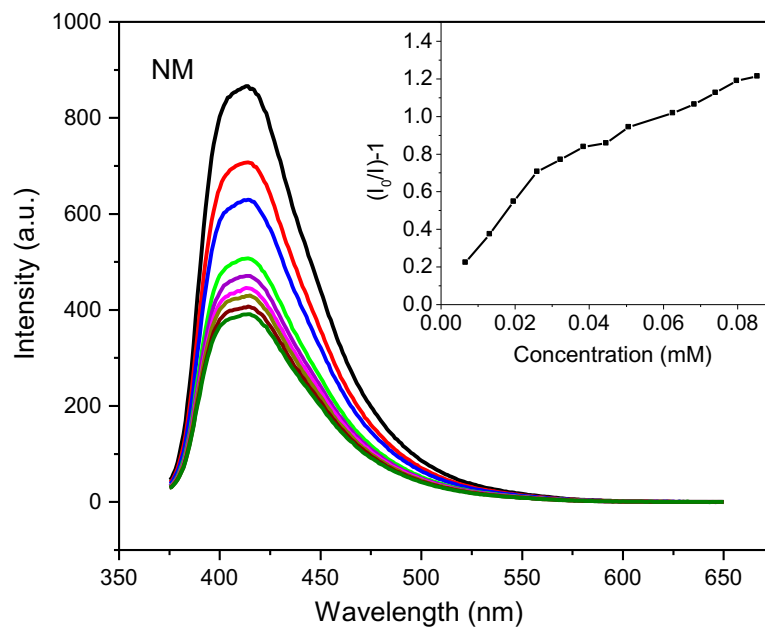


Figure V-14. Luminescence quenching spectra of PCN-811 towards NM.

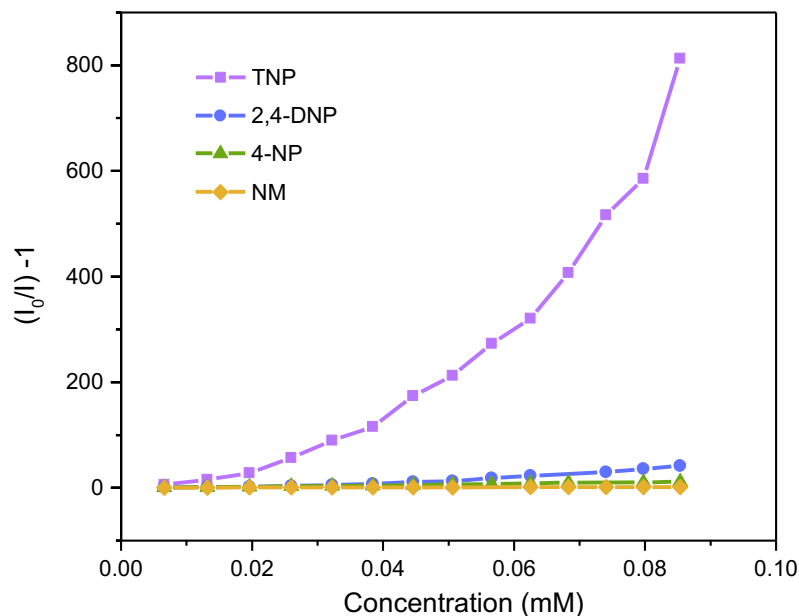


Figure V-15. Comparison of Stern-Volmer plots.

5.3.5 Mechanism

To get deep insight into the detection mechanisms, the relative orbital energy levels of the analytes were provided by DFT calculations (Table S). As it is known, the conducting bands (CB) of electron-rich MOFs usually lie at a higher level than the lowest unoccupied molecular orbitals (LUMOs) of the electron-deficient analytes, which triggers the photo-induced electron transfer; the lower the LUMOs energy level of an analyte lies, the more easily the electron can be transferred from MOFs to analytes.^{92, 281} Herein, the lowest LUMO energy of TNP can persuasively explain the highest quenching efficiency and selectivity. The non-linear relationship of the SV plot also prompts us to study other possible mechanisms in the sensing process. The absorbance spectrum of TNP shows the greatest spectral overlap with the emission spectrum of MOF, demonstrating the contribution of resonance energy transfer; While for others, the overlap is much smaller or

even negligible (Figure V-16). Additionally, the fact that PCN-811 displays a higher sensitivity towards phenolic-type analytes and the ones with higher acidity (2,4,6-TNP > 2,4-DNP > 4-NP > NM) suggests the existence of electrostatic interactions.²⁸²⁻²⁸³

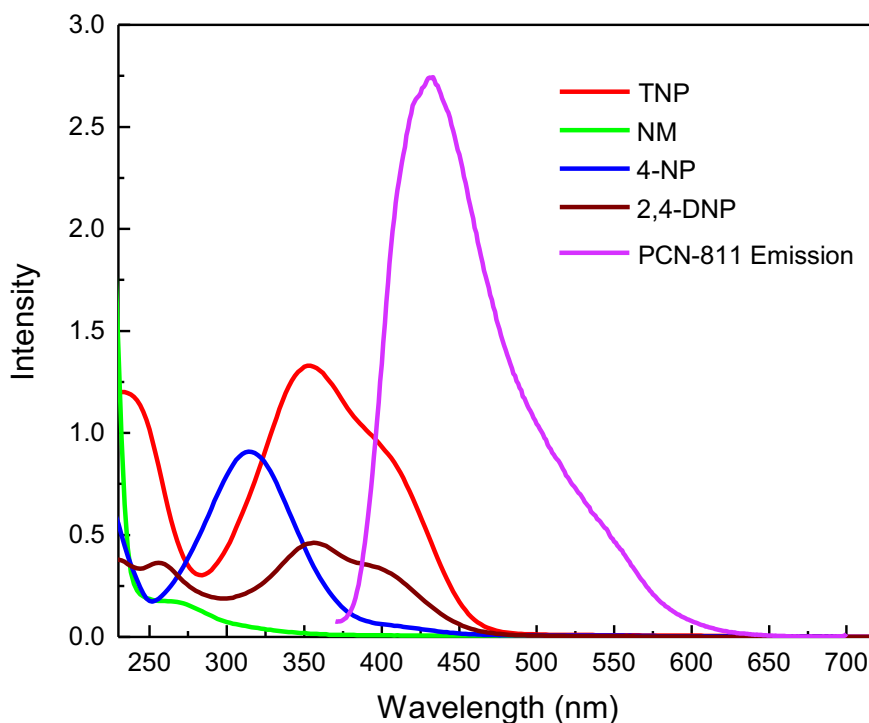


Figure V-16. The overlap between the absorbance spectra of different explosives and the emission spectrum of PCN-811.

5.4 Conclusion

In summary, we have synthesized an AIEE-active ligand, H₆TPHB, by functioning triphenylene core with six carboxylates at the periphery. Through solvothermal reaction with zirconium salt, the ligand affords a highly luminescent MOF, PCN-811, with a novel xx structure/topology. The absolute quantum yield of the generated MOF is 38%, a 4-fold enhancement in comparison with the other aggregated states of the linker. Further studies prove

that PCN-811 a promising sensor towards TNP with a record-high quenching constant K_{sv} of 3×10^7 M^{-1} and a low detection limit of 2.3 ppb in aqueous media. This work firstly integrates a triphenylene-typed AIEEgen into MOFs and achieves its superior luminescence performance with the aid of MOF matrix. It also exemplifies an approach for the highly conjugated compounds to overcome the undesired luminescence-quenched aggregation, which is an alternative to the tedious organic structural modification. With the interest of its unique photophysical properties, works on the other applications of the newly synthesized MOF, non-linear optics for example, are in progress.

CHAPTER VI

CONCLUSIONS

This dissertation described the rational synthesis of functional MOFs for the applications of heterogeneous catalysis and chemo-sensing via linker design. Based on a prototype mesoporous structure, PCN-777, a tritopic terpyridine-based linker was designed, leading to the successful preparation of a novel isostructural MOF, PCN-308, guided by topological analysis. Because of the superb coordination capability of the terpyridine chelating sites, redox-active metal ions could complex in the MOF via post-synthetic metalation under mild conditions yielding high loading rates. In addition, the large cage cavities in the network facilitate the access of the up-coming substrates to the active sites. As a result, the metalated materials, Fe@PCN-308 and Co@PCN-308, could efficiently catalyze alkene epoxidation and arene borylation reactions with decent yields.

By the implementation of similar topological guidance, another tritopic linker was derived to synthesize a mesoporous MOF based upon a structural template, PCN-333. Inheriting the virtues of PCN-333, the newly synthesized MOF not only exhibits extremely large cavities, but also retains excellent thermal and chemical stability. Besides, the MOF shows good emission in water. The fluorescent MOF was herein utilized as a sensor to detect Fe³⁺ in aqueous media. When exposed to trace amounts of Fe³⁺, the fluorescence of PCN-604 can be rapidly quenched within seconds. The fast response can be ascribed to the mesoporous cavities, which can pre-concentrate the analytes and release the diffusion constrains. Moreover, the MOF-based sensor demonstrates promising sensitivity and selectivity studied qualitatively and quantitatively. The underlying mechanisms involve the host-guest fluorescence resonance energy transfer (FRET) and/or

photoinduced electron transfer (PET). Meanwhile, the intrinsic electron-donating pyridine groups on the linker contributes to the selectivity of the sensing process.

Driven by the energy requirement of sustainable development, efforts have been devoted to explore MOF-based materials that can efficiently convert solar energy and catalyze organic transformations in environmentally benign conditions. Inspired by the abilities of pyrene in singlet oxygen generation, we designed a tetratopic pyrene-based ligand to afford a MOF system that can produce $^1\text{O}_2$ under the excitation of visible light. Direct solvothermal reactions between the organic linker and Zr_6 or Hf_6 clusters afforded PCN-822(Zr) and PCN-822(Hf) with a (4,8)-connected **sqc** topology isorecticular to PCN-225. It was found that the adsorption of the resulting MOFs resides in the visible-light range, meeting the prerequisite of visible-light harvesting. Further studies proved that both MOFs show improved efficiency in singlet oxygen generation. Additionally, when triggering the aerobic photooxidation of amines to imines, PCN-822(Hf) not only serves as a $^1\text{O}_2$ generator but also displays semiconductor-like behavior to produce $\text{O}_2^{\bullet-}$ via photo-induced charge transfer.

The synthesis of luminescent MOFs often involves applying highly conjugated organic chromophores as linkers. To study the unique photophysical properties of MOF systems, we have synthesized an AIEE-active ligand by functionalizing a triphenylene core with six carboxylates at the periphery. This novel ligand produced a novel MOF with high luminescence. In the structure, the rigidity of the framework impedes the free rotation of the phenyl-carboxylate groups, preventing undesirable nonradiative decay. Furthermore, the fluorescent triphenylene cores are separated to long distance to overcome intermolecular energy transfer. Hence, after anchoring onto the MOF scaffold, the ligand experiences a remarkable increase in luminescent efficiency compared with its free state. Because of its electron-rich nature, the luminescent MOF was then

used as a sensor for electron-deficient explosives detection in aqueous media. The proof-of-concept work demonstrates the MOF can serve as an alternative of AIEE, providing an approach for the highly conjugated compounds to overcome the undesired ACQ process.

Overall, the works mentioned above systematically demonstrate the indispensable role of linker design in tuning the structure and functionality of MOFs at the molecular level, shining light on the rational synthesis of advanced functional MOFs for targeted applications.

REFERENCES

1. Zhou, H.-C.; Long, J. R.; Yaghi, O. M., *Chem. Rev.*, **2012**, *112* (2), 673-674.
2. Eddaoudi, M.; Moler, D. B.; Li, H.; Chen, B.; Reineke, T. M.; O'keeffe, M.; Yaghi, O. M., *Acc. Chem. Res.*, **2001**, *34* (4), 319-330.
3. Kitagawa, S.; Kitaura, R.; Noro, S. i., *Angew. Chem. Int. Ed.*, **2004**, *43* (18), 2334-2375.
4. Li, H.; Eddaoudi, M.; O'Keeffe, M.; Yaghi, O. M., *Nature*, **1999**, *402* (6759), 276-279.
5. Chui, S. S.-Y.; Lo, S. M.-F.; Charmant, J. P.; Orpen, A. G.; Williams, I. D., *Science*, **1999**, *283* (5405), 1148-1150.
6. Xuan, W.; Zhu, C.; Liu, Y.; Cui, Y., *Chem. Soc. Rev.*, **2012**, *41* (5), 1677-1695.
7. Férey, G.; Mellot-Draznieks, C.; Serre, C.; Millange, F.; Dutour, J.; Surblé, S.; Margiolaki, I., *Science*, **2005**, *309* (5743), 2040-2042.
8. Cavka, J. H.; Jakobsen, S.; Olsbye, U.; Guillou, N.; Lamberti, C.; Bordiga, S.; Lillerud, K. P., *J. Am. Chem. Soc.*, **2008**, *130* (42), 13850-13851.
9. Devic, T.; Serre, C., *Chem. Soc. Rev.*, **2014**, *43* (16), 6097-6115.
10. Lee, J.; Farha, O. K.; Roberts, J.; Scheidt, K. A.; Nguyen, S. T.; Hupp, J. T., *Chem. Soc. Rev.*, **2009**, *38* (5), 1450-1459.

11. Furukawa, H.; Cordova, K. E.; O'Keeffe, M.; Yaghi, O. M., *Science*, **2013**, *341* (6149), 1230444-1230444.
12. Nath, I.; Chakraborty, J.; Verpoort, F., *Chem. Soc. Rev.*, **2016**, *45* (15), 4127-4170.
13. Kreno, L. E.; Leong, K.; Farha, O. K.; Allendorf, M.; Van Duyne, R. P.; Hupp, J. T., *Chem. Rev.*, **2012**, *112* (2), 1105-1125.
14. Li, J. R.; Sculley, J.; Zhou, H. C., *Chem. Rev.*, **2012**, *112* (2), 869-932.
15. Zhang, Y.; Yuan, S.; Day, G.; Wang, X.; Yang, X.; Zhou, H.-C., *Coord. Chem. Rev.*, **2018**, *354*, 28-45.
16. Ramaswamy, P.; Wong, N. E.; Shimizu, G. K., *Chem. Soc. Rev.*, **2014**, *43* (16), 5913-5932.
17. Espallargas, G. M.; Coronado, E., *Chem. Soc. Rev.*, **2018**, *47* (2), 533-557.
18. Lian, X.; Fang, Y.; Joseph, E.; Wang, Q.; Li, J.; Banerjee, S.; Lollar, C.; Wang, X.; Zhou, H.-C., *Chem. Soc. Rev.*, **2017**, *46* (11), 3386-3401.
19. Dolgoplova, E. A.; Rice, A. M.; Martin, C. R.; Shustova, N. B., *Chem. Soc. Rev.*, **2018**, *47* (13), 4710-4728.
20. Wang, H.; Zhu, Q.-L.; Zou, R.; Xu, Q., *Chem*, **2017**, *2* (1), 52-80.
21. Yaghi, O. M., *J. Am. Chem. Soc.*, **2016**, *138* (48), 15507-15509.

22. Yaghi, O. M.; O'keeffe, M.; Ockwig, N. W.; Chae, H. K.; Eddaoudi, M.; Kim, J., *Nature*, **2003**, *423* (6941), 705-714.
23. Bai, Y.; Dou, Y.; Xie, L.-H.; Rutledge, W.; Li, J.-R.; Zhou, H.-C., *Chem. Soc. Rev.*, **2016**, *45* (8), 2327-2367.
24. Ockwig, N. W.; Delgado-Friedrichs, O.; O'Keeffe, M.; Yaghi, O. M., *Acc. Chem. Res.*, **2005**, *38* (3), 176-182.
25. Feng, D.; Liu, T. F.; Su, J.; Bosch, M.; Wei, Z.; Wan, W.; Yuan, D.; Chen, Y. P.; Wang, X.; Wang, K.; Lian, X.; Gu, Z. Y.; Park, J.; Zou, X.; Zhou, H.-C., *Nat. Commun.*, **2015**, *6*, 5979-5987.
26. Férey, G.; Serre, C.; Mellot - Draznieks, C.; Millange, F.; Surblé, S.; Dutour, J.; Margiolaki, I., *Angew. Chem. Int. Ed.*, **2004**, *43* (46), 6296-6301.
27. Park, J.; Feng, D.; Zhou, H.-C., *J. Am. Chem. Soc.*, **2015**, *137* (4), 1663-1672.
28. Ma, J.; Tran, L. D.; Matzger, A. J., *Cryst. Growth Des.*, **2016**, *16* (7), 4148-4153.
29. O'Keeffe, M.; Yaghi, O. M., *Chem. Rev.*, **2011**, *112* (2), 675-702.
30. Feng, D.; Chung, W.-C.; Wei, Z.; Gu, Z.-Y.; Jiang, H.-L.; Chen, Y.-P.; Darensbourg, D. J.; Zhou, H.-C., *J. Am. Chem. Soc.*, **2013**, *135* (45), 17105-17110.

31. Feng, D.; Gu, Z. Y.; Li, J. R.; Jiang, H. L.; Wei, Z.; Zhou, H.-C., *Angew. Chem. Int. Ed.*, **2012**, *51* (41), 10307-10310.
32. Wong-Foy, A. G.; Matzger, A. J.; Yaghi, O. M., *J. Am. Chem. Soc.*, **2006**, *128* (11), 3494-3495.
33. Eddaoudi, M.; Kim, J.; Rosi, N.; Vodak, D.; Wachter, J.; O'keeffe, M.; Yaghi, O. M., *Science*, **2002**, *295* (5554), 469-472.
34. Lu, W.; Wei, Z.; Gu, Z.-Y.; Liu, T.-F.; Park, J.; Park, J.; Tian, J.; Zhang, M.; Zhang, Q.; Gentle III, T.; Bosch, M.; Zhou, H.-C., *Chem. Soc. Rev.*, **2014**, *43* (16), 5561-5593.
35. Deng, H.; Grunder, S.; Cordova, K. E.; Valente, C.; Furukawa, H.; Hmadeh, M.; Gándara, F.; Whalley, A. C.; Liu, Z.; Asahina, S., *Science*, **2012**, *336* (6084), 1018-1023.
36. Liu, T.-F.; Feng, D.; Chen, Y.-P.; Zou, L.; Bosch, M.; Yuan, S.; Wei, Z.; Fordham, S.; Wang, K.; Zhou, H.-C., *J. Am. Chem. Soc.*, **2014**, *137* (1), 413-419.
37. Tanabe, K. K.; Cohen, S. M., *Chem. Soc. Rev.*, **2011**, *40* (2), 498-519.
38. Li, Q.; Zhang, W.; Miljanić, O. Š.; Sue, C.-H.; Zhao, Y.-L.; Liu, L.; Knobler, C. B.; Stoddart, J. F.; Yaghi, O. M., *Science*, **2009**, *325* (5942), 855-859.
39. Jiang, H. L.; Feng, D.; Liu, T. F.; Li, J. R.; Zhou, H.-C., *J. Am. Chem. Soc.*, **2012**, *134* (36), 14690-14693.

40. Rasero-Almansa, A. M.; Corma, A.; Iglesias, M.; Sánchez, F., *Green Chem.*, **2014**, *16* (7), 3522-3527.
41. Fei, H.; Cohen, S. M., *J. Am. Chem. Soc.*, **2015**, *137* (6), 2191-2194.
42. Yuan, S.; Feng, L.; Wang, K.; Pang, J.; Bosch, M.; Lollar, C.; Sun, Y.; Qin, J.; Yang, X.; Zhang, P.; Wang, Q.; Zou, L.; Zhang, Y.; Zhang, L.; Fang, Y.; Li, J.; Zhou, H.-C., *Adv. Mater.*, **2018**, *30* (37), 1704303-1704338.
43. Abedi, S.; Morsali, A., *ACS Catal.*, **2014**, *4* (5), 1398-1403.
44. Yoon, M.; Srirambalaji, R.; Kim, K., *Chem. Rev.*, **2012**, *112* (2), 1196-231.
45. Yuan, S.; Qin, J. S.; Lollar, C. T.; Zhou, H.-C., *ACS Cent Sci*, **2018**, *4* (4), 440-450.
46. Sawano, T.; Ji, P.; McIsaac, A. R.; Lin, Z.; Abney, C. W.; Lin, W., *Chem. Sci.*, **2015**, *6* (12), 7163-7168.
47. Yuan, S.; Liu, T. F.; Feng, D.; Tian, J.; Wang, K.; Qin, J.; Zhang, Q.; Chen, Y. P.; Bosch, M.; Zou, L.; Teat, S. J.; Dalgarno, S. J.; Zhou, H.-C., *Chem. Sci.*, **2015**, *6* (7), 3926-3930.
48. Li, L.; Yang, Q.; Chen, S.; Hou, X.; Liu, B.; Lu, J.; Jiang, H.-L., *Chem. Commun.*, **2017**, *53* (72), 10026-10029.
49. Shaik, S.; Cohen, S.; Wang, Y.; Chen, H.; Kumar, D.; Thiel, W., *Chem. Rev.*, **2009**, *110* (2), 949-1017.

50. Zhao, M.; Ou, S.; Wu, C. D., *Acc. Chem. Res.*, **2014**, *47* (4), 1199-1207.
51. Chen, Y.; Ma, S., *Dalton Trans*, **2016**, *45* (24), 9744-9753.
52. Gao, W. Y.; Chrzanowski, M.; Ma, S., *Chem. Soc. Rev.*, **2014**, *43* (16), 5841-5866.
53. Chen, Y.; Hoang, T.; Ma, S., *Inorg. Chem.*, **2012**, *51* (23), 12600-12602.
54. Morris, W.; Voloskiy, B.; Demir, S.; Gandara, F.; McGrier, P. L.; Furukawa, H.; Cascio, D.; Stoddart, J. F.; Yaghi, O. M., *Inorg. Chem.*, **2012**, *51* (12), 6443-6445.
55. Feng, D.; Gu, Z. Y.; Li, J. R.; Jiang, H. L.; Wei, Z.; Zhou, H.-C., *Angew. Chem. Int. Ed. Engl.*, **2012**, *51* (41), 10307-10310.
56. Huang, N.; Yuan, S.; Drake, H.; Yang, X.; Pang, J.; Qin, J.; Li, J.; Zhang, Y.; Wang, Q.; Jiang, D.; Zhou, H.-C., *J. Am. Chem. Soc.*, **2017**, *139* (51), 18590-18597.
57. Hammarström, L., *Artificial photosynthesis and solar fuels*. ACS Publications: 2009.
58. Gust, D.; Moore, T. A.; Moore, A. L., *Acc. Chem. Res.*, **2009**, *42* (12), 1890-1898.
59. Zhang, T.; Lin, W., *Chem. Soc. Rev.*, **2014**, *43* (16), 5982-5993.
60. Wang, C.; Xie, Z.; deKrafft, K. E.; Lin, W., *J. Am. Chem. Soc.*, **2011**, *133* (34), 13445-13454.
61. Little, S. T.; Edworthy, I. S.; Arnold, P. L., *Chem. Soc. Rev.*, **2007**, *36* (11), 1732-1744.

62. Carson, F.; Martínez-Castro, E.; Marcos, R.; Miera, G. G.; Jansson, K.; Zou, X.; Martín-Matute, B., *Chem. Commun.*, **2015**, *51* (54), 10864-10867.
63. Bartoszewicz, A.; Marcos, R.; Sahoo, S.; Inge, A. K.; Zou, X.; Martín - Matute, B., *Chem. Eur. J.*, **2012**, *18* (45), 14510-14519.
64. Wei, Y. L.; Li, Y.; Chen, Y. Q.; Dong, Y.; Yao, J. J.; Han, X. Y.; Dong, Y. B., *Inorg. Chem.*, **2018**, *57* (8), 4379-4386.
65. Burgess, S. A.; Kassie, A.; Baranowski, S. A.; Fritzsching, K. J.; Schmidt-Rohr, K.; Brown, C. M.; Wade, C. R., *J. Am. Chem. Soc.*, **2016**, *138* (6), 1780-1783.
66. Pullen, S.; Fei, H.; Orthaber, A.; Cohen, S. M.; Ott, S., *J. Am. Chem. Soc.*, **2013**, *135* (45), 16997-17003.
67. Sasan, K.; Lin, Q.; Mao, C.; Feng, P., *Chem. Commun.*, **2014**, *50* (72), 10390-10393.
68. Fateeva, A.; Chater, P. A.; Ireland, C. P.; Tahir, A. A.; Khimiyak, Y. Z.; Wiper, P. V.; Darwent, J. R.; Rosseinsky, M. J., *Angew. Chem. Int. Ed. Engl.*, **2012**, *51* (30), 7440-7444.
69. Feng, D.; Gu, Z. Y.; Chen, Y. P.; Park, J.; Wei, Z.; Sun, Y.; Bosch, M.; Yuan, S.; Zhou, H.-C., *J. Am. Chem. Soc.*, **2014**, *136* (51), 17714-17717.
70. Jiang, W.; Yang, J.; Liu, Y. Y.; Song, S. Y.; Ma, J. F., *Inorg. Chem.*, **2017**, *56* (5), 3036-3043.

71. Fei, H.; Cohen, S. M., *Chem. Commun.*, **2014**, 50 (37), 4810-4812.
72. Yu, X.; Cohen, S. M., *Chem. Commun.*, **2015**, 51 (48), 9880-9883.
73. Toyao, T.; Miyahara, K.; Fujiwaki, M.; Kim, T.-H.; Dohshi, S.; Horiuchi, Y.; Matsuoka, M., *J. Phys. Chem. C*, **2015**, 119 (15), 8131-8137.
74. Zhang, T.; Manna, K.; Lin, W., *J. Am. Chem. Soc.*, **2016**, 138 (9), 3241-3249.
75. Manna, K.; Zhang, T.; Lin, W., *J. Am. Chem. Soc.*, **2014**, 136 (18), 6566-6569.
76. An, Y.; Liu, Y.; An, P.; Dong, J.; Xu, B.; Dai, Y.; Qin, X.; Zhang, X.; Whangbo, M. H.; Huang, B., *Angew. Chem. Int. Ed. Engl.*, **2017**, 56 (11), 3036-3040.
77. Rasero-Almansa, A. M.; Corma, A.; Iglesias, M.; Sánchez, F., *ChemCatChem*, **2014**, 6 (6), 1794-1800.
78. Rasero-Almansa, A. M.; Corma, A.; Iglesias, M.; Sánchez, F., *ChemCatChem*, **2013**, 5 (10), 3092-3100.
79. Kaposi, M.; Cokoja, M.; Hutterer, C. H.; Hauser, S. A.; Kaposi, T.; Klappenberger, F.; Pothig, A.; Barth, J. V.; Herrmann, W. A.; Kuhn, F. E., *Dalton Trans*, **2015**, 44 (36), 15976-15983.
80. Tang, J.; Dong, W.; Wang, G.; Yao, Y.; Cai, L.; Liu, Y.; Zhao, X.; Xu, J.; Tan, L., *RSC Adv.*, **2014**, 4 (81), 42977-42982.

81. Manna, K.; Zhang, T.; Carboni, M.; Abney, C. W.; Lin, W., *J. Am. Chem. Soc.*, **2014**, *136* (38), 13182-13185.
82. Yang, H.; Zhang, X.; Zhang, G.; Fei, H., *Chem. Commun.*, **2018**, *54* (35), 4469-4472.
83. Thacker, N. C.; Lin, Z.; Zhang, T.; Gilhula, J. C.; Abney, C. W.; Lin, W., *J. Am. Chem. Soc.*, **2016**, *138* (10), 3501-3509.
84. Fei, H.; Shin, J.; Meng, Y. S.; Adelhardt, M.; Sutter, J.; Meyer, K.; Cohen, S. M., *J. Am. Chem. Soc.*, **2014**, *136* (13), 4965-4973.
85. Falkowski, J. M.; Sawano, T.; Zhang, T.; Tsun, G.; Chen, Y.; Lockard, J. V.; Lin, W., *J. Am. Chem. Soc.*, **2014**, *136* (14), 5213-5216.
86. Noyori, R.; Takaya, H., *Acc. Chem. Res.*, **1990**, *23* (10), 345-350.
87. Sawano, T.; Thacker, N. C.; Lin, Z.; McIsaac, A. R.; Lin, W., *J. Am. Chem. Soc.*, **2015**, *137* (38), 12241-12248.
88. Blasse, G.; Grabmaier, B., Energy transfer. In *Luminescent Materials*, Springer: 1994; 91-107.
89. Atari, N., *Phys. Lett. A*, **1982**, *90* (1-2), 93-96.
90. Hasegawa, Y.; Kimura, Y.; Murakoshi, K.; Wada, Y.; Kim, J.-H.; Nakashima, N.; Yamanaka, T.; Yanagida, S., *J. Phys. Chem.*, **1996**, *100* (24), 10201-10205.

91. Bünzli, J.-C. G., *Chem. Rev.*, **2010**, *110* (5), 2729-2755.
92. Lan, A.; Li, K.; Wu, H.; Olson, D. H.; Emge, T. J.; Ki, W.; Hong, M.; Li, J., *Angew. Chem. Int. Ed.*, **2009**, *48* (13), 2334-2338.
93. Allendorf, M. D.; Bauer, C. A.; Bhakta, R. K.; Houk, R. J., *Chem. Soc. Rev.*, **2009**, *38* (5), 1330-1352.
94. Tang, Y.-Y.; Ding, C.-X.; Ng, S.-W.; Xie, Y.-S., *RSC Advances*, **2013**, *3* (39), 18134-18141.
95. Chen, W.; Wang, J.-Y.; Chen, C.; Yue, Q.; Yuan, H.-M.; Chen, J.-S.; Wang, S.-N., *Inorg. Chem.*, **2003**, *42* (4), 944-946.
96. Dai, J.-C.; Wu, X.-T.; Fu, Z.-Y.; Cui, C.-P.; Hu, S.-M.; Du, W.-X.; Wu, L.-M.; Zhang, H.-H.; Sun, R.-Q., *Inorg. Chem.*, **2002**, *41* (6), 1391-1396.
97. Tsuge, K.; Chishina, Y.; Hashiguchi, H.; Sasaki, Y.; Kato, M.; Ishizaka, S.; Kitamura, N., *Coord. Chem. Rev.*, **2016**, *306*, Part 2, 636-651.
98. Ni, J.; Wei, K.-J.; Min, Y.; Chen, Y.; Zhan, S.; Li, D.; Liu, Y., *Dalton Trans.*, **2012**, *41* (17), 5280-5293.
99. Jin, F.; Zhang, Y.; Wang, H.-Z.; Zhu, H.-Z.; Yan, Y.; Zhang, J.; Wu, J.-Y.; Tian, Y.-P.; Zhou, H.-P., *Cryst. Growth Des.*, **2013**, *13* (5), 1978-1987.

100. Cui, Y.; Chen, B.; Qian, G., *Coord. Chem. Rev.*, **2014**, 273–274, 76-86.
101. Kreno, L. E.; Leong, K.; Farha, O. K.; Allendorf, M.; Van Duyne, R. P.; Hupp, J. T., *Chem. Rev.*, **2012**, 112 (2), 1105-1125.
102. Zeng, G.; Xing, S.; Wang, X.; Yang, Y.; Ma, D.; Liang, H.; Gao, L.; Hua, J.; Li, G.; Shi, Z.; Feng, S., *Inorg. Chem.*, **2016**, 55 (3), 1089-1095.
103. Yang, L. Z.; Wang, J.; Kirillov, A. M.; Dou, W.; Xu, C.; Fang, R.; Xu, C. L.; Liu, W. S., *Crystengcomm*, **2016**, 18 (34), 6425-6436.
104. Pramanik, S.; Zheng, C.; Zhang, X.; Emge, T. J.; Li, J., *J. Am. Chem. Soc.*, **2011**, 133 (12), 4153-4155.
105. Buragohain, A.; Yousufuddin, M.; Sarma, M.; Biswas, S., *Crystal Growth & Design*, **2016**, 16 (2), 842-851.
106. Hu, Z.; Deibert, B. J.; Li, J., *Chem. Soc. Rev.*, **2014**, 43 (16), 5815-5840.
107. Yaghi, O. M.; O’Keeffe, M.; Ockwig, N. W.; Chae, H. K.; Eddaoudi, M.; Kim, J., *Nature*, **2003**, 423, 705-714.
108. Liu, T. F.; Feng, D.; Chen, Y. P.; Zou, L.; Bosch, M.; Yuan, S.; Wei, Z.; Fordham, S.; Wang, K.; Zhou, H.-C., *J. Am. Chem. Soc.*, **2015**, 137 (1), 413-419.

109. Lu, W.; Wei, Z.; Gu, Z. Y.; Liu, T. F.; Park, J.; Park, J.; Tian, J.; Zhang, M.; Zhang, Q.; III, T. G.; Boscha, M.; Zhou, H. C., *Chem. Soc. Rev.*, **2014**, *43*, 5561-5593
110. Xia, T.; Song, T.; Cui, Y.; Yang, Y.; Qian, G., *Dalton Trans.*, **2016**, *45* (46), 18689-18695.
111. Lian, X.; Yan, B., *RSC Advances*, **2016**, *6* (14), 11570-11576.
112. Cui, Y.; Yue, Y.; Qian, G.; Chen, B., *Chem. Rev.*, **2012**, *112* (2), 1126-1162.
113. Carter, K. P.; Young, A. M.; Palmer, A. E., *Chem. Rev.*, **2014**, *114* (8), 4564-4601.
114. Zhao, X. L.; Tian, D.; Gao, Q.; Sun, H. W.; Xu, J.; Bu, X. H., *Dalton Trans.*, **2016**, *45* (3), 1040-1046.
115. Xu, H.; Gao, J.; Qian, X.; Wang, J.; He, H.; Cui, Y.; Yang, Y.; Wang, Z.; Qian, G., *J. Mater. Chem. A*, **2016**, *4* (28), 10900-10905.
116. Hu, Z.; Deibert, B. J.; Li, J., *Chem. Soc. Rev.*, **2014**, *43* (16), 5815-5840.
117. Zhang, L.; Kang, Z.; Xin, X.; Sun, D., *CrystEngComm*, **2016**, *18* (2), 193-206.
118. Mukherjee, S.; Desai, A. V.; Manna, B.; Inamdar, A. I.; Ghosh, S. K., *Cryst. Growth Des.*, **2015**, *15* (9), 4627-4634.
119. Guo, Y.; Feng, X.; Han, T.; Wang, S.; Lin, Z.; Dong, Y.; Wang, B., *J. Am. Chem. Soc.*, **2014**, *136* (44), 15485-15488.

120. Rimoldi, M.; Howarth, A. J.; DeStefano, M. R.; Lin, L.; Goswami, S.; Li, P.; Hupp, J. T.; Farha, O. K., *ACS Catal.*, **2016**, *7* (2), 997-1014.
121. Zhu, L.; Liu, X. Q.; Jiang, H. L.; Sun, L. B., *Chem. Rev.*, **2017**, *117* (12), 8129-8176.
122. Yuan, S.; Feng, L.; Wang, K.; Pang, J.; Bosch, M.; Lollar, C.; Sun, Y.; Qin, J.; Yang, X.; Zhang, P.; Wang, Q.; Zou, L.; Zhang, Y.; Zhang L.; Fang Y.; Li, J.; Zhou, H.-C., *Adv. Mater.*, **2018**, *30* (37), 1704303.
123. Xia, Q.-H.; Ge, H.-Q.; Ye, C.-P.; Liu, Z.-M.; Su, K.-X., *Chem. Rev.*, **2005**, *105* (5), 1603-1662.
124. Rimoldi, M.; Nakamura, A.; Vermeulen, N. A.; Henkelis, J. J.; Blackburn, A. K.; Hupp, J. T.; Stoddart, J. F.; Farha, O. K., *Chem. Sci.*, **2016**, *7* (8), 4980-4984.
125. Zhang, L.; Chen, J.; Fan, T.; Shen, K.; Jiang, M.; Li, Y., *Chem. Commun.*, **2018**, *54* (33), 4188-4191.
126. Qin, J. S.; Yuan, S.; Lollar, C.; Pang, J.; Alsalme, A.; Zhou, H.-C., *Chem. Commun.*, **2018**, *54* (34), 4231-4249.
127. Wang, X.; Lu, W.; Gu, Z.-Y.; Wei, Z.; Zhou, H.-C., *Chem. Commun.*, **2016**, *52* (9), 1926-1929.
128. Togni, A.; Venanzi, L. M., *Angew. Chem. Int. Ed.*, **1994**, *33* (5), 497-526.

129. Zhang, Y.; Yang, X.; Zhou, H.-C., *Polyhedron*, **2018**, *154*, 189-201.
130. Manna, K.; Zhang, T.; Greene, F. X.; Lin, W., *J. Am. Chem. Soc.*, **2015**, *137* (7), 2665-2673.
131. Zhu, C.; Xia, Q.; Chen, X.; Liu, Y.; Du, X.; Cui, Y., *ACS Catal.*, **2016**, *6* (11), 7590-7596.
132. Wang, Y.; Cui, H.; Wei, Z. W.; Wang, H. P.; Zhang, L.; Su, C. Y., *Chem. Sci.*, **2017**, *8* (1), 775-780.
133. Wang, C.; Wang, J. L.; Lin, W., *J. Am. Chem. Soc.*, **2012**, *134* (48), 19895-19908.
134. Park, K. C.; Cho, J.; Lee, C. Y., *RSC Advances*, **2016**, *6* (79), 75478-75481.
135. Liu, P.; Zhou, C.-Y.; Xiang, S.; Che, C.-M., *Chem. Commun.*, **2010**, *46* (16), 2739-2741.
136. Léonard, N. G.; Bezdek, M. J.; Chirik, P. J., *Organometallics*, **2016**, *36* (1), 142-150.
137. Winter, A.; Newkome, G. R.; Schubert, U. S., *ChemCatChem*, **2011**, *3* (9), 1384-1406.
138. Peris, E.; Crabtree, R. H., *Chem. Soc. Rev.*, **2018**, *47* (6), 1959-1968.
139. Zheng, M.; Tan, H.; Xie, Z.; Zhang, L.; Jing, X.; Sun, Z., *ACS Appl. Mater. Interfaces*, **2013**, *5* (3), 1078-1083.
140. Zhang, J.; Yang, W.; Wu, X.-Y.; Zhang, L.; Lu, C.-Z., *Cryst. Growth Des.*, **2015**, *16* (1), 475-482.

141. Wang, W.; Xiao, Z.; Lin, H.; Wang, R.; Zhang, L.; Sun, D., *RSC Adv.*, **2016**, *6* (20), 16575-16580.
142. Gai, Y. L.; Jiang, F. L.; Chen, L.; Bu, Y.; Wu, M. Y.; Zhou, K.; Pan, J.; Hong, M. C., *Dalton Tran.*, **2013**, *42* (27), 9954-65.
143. Lin, Z.; Thacker, N. C.; Sawano, T.; Drake, T.; Ji, P.; Lan, G.; Cao, L.; Liu, S.; Wang, C.; Lin, W., *Chem. Sci.*, **2018**, *9* (1), 143-151.
144. Cao, L.; Lin, Z.; Peng, F.; Wang, W.; Huang, R.; Wang, C.; Yan, J.; Liang, J.; Zhang, Z.; Zhang, T.; Long, L.; Sun, J.; Lin, W., *Angew. Chem. Int. Ed.*, **2016**, *55* (16), 4962-4966.
145. Cliffe, M. J.; Castillo-Martinez, E.; Wu, Y.; Lee, J.; Forse, A. C.; Firth, F. C. N.; Moghadam, P. Z.; Fairen-Jimenez, D.; Gaultois, M. W.; Hill, J. A.; Magdysyuk, O. V.; Slater, B.; Goodwin, A. L.; Grey, C. P., *J. Am. Chem. Soc.*, **2017**, *139* (15), 5397-5404.
146. Zhao, M.; Lu, Q.; Ma, Q.; Zhang, H., *Small Methods*, **2017**, *1* (1-2), 1600030.
147. Ma, B.; Xu, J.; Qi, H.; Sun, J.; Chai, J.; Jia, J.; Jing, S.; Fan, Y.; Wang, L., *J. Solid State Chem.*, **2018**, *258*, 42-48.
148. Liu, B.; Wong-Foy, A. G.; Matzger, A. J., *Chem. Commun.*, **2013**, *49* (14), 1419-1421.
149. Feng, D.; Wang, K.; Su, J.; Liu, T. F.; Park, J.; Wei, Z.; Bosch, M.; Yakovenko, A.; Zou, X.; Zhou, H.-C., *Angew. Chem. Int. Ed. Engl.*, **2015**, *54* (1), 149-154.

150. Liu, H.; Xu, C.; Li, D.; Jiang, H.-L., *Angew. Chem. Int. Ed.*, **2018**, *57* (19), 5379-5383.
151. Accelrys, I., *Accelrys Software Inc*, **2010**.
152. Yang, X.; Yuan, S.; Zou, L.; Drake, H.; Zhang, Y.; Qin, J.; Alsalmeh, A.; Zhou, H.-C., *Angew. Chem. Int. Ed. Engl.*, **2018**, *57* (15), 3927-3932.
153. Zhang, J.; Biradar, A. V.; Pramanik, S.; Emge, T. J.; Asefa, T.; Li, J., *Chem. Commun.*, **2012**, *48* (52), 6541-6543.
154. Qi, Y.; Luan, Y.; Yu, J.; Peng, X.; Wang, G., *Chem. Eur. J.*, **2015**, *21* (4), 1589-1597.
155. Wang, J.; Yang, M.; Dong, W.; Jin, Z.; Tang, J.; Fan, S.; Lu, Y.; Wang, G., *Catal. Sci. Technol.*, **2016**, *6* (1), 161-168.
156. Yuan, K.; Song, T.; Wang, D.; Zou, Y.; Li, J.; Zhang, X.; Tang, Z.; Hu, W., *Nanoscale*, **2018**, *10* (4), 1591-1597.
157. Obligacion, J. V.; Semproni, S. P.; Chirik, P. J., *J. Am. Chem. Soc.*, **2014**, *136* (11), 4133-4136.
158. Sawano, T.; Lin, Z.; Boures, D.; An, B.; Wang, C.; Lin, W., *J. Am. Chem. Soc.*, **2016**, *138* (31), 9783-9786.
159. Dickinson, B. C.; Chang, C. J., *Nat. Chem. Biol.*, **2011**, *7* (8), 504-511.
160. Apel, K.; Hirt, H., *Annu. Rev. Plant Biol.*, **2004**, *55*, 373-399.

161. Zhou, Z.; Song, J.; Nie, L.; Chen, X., *Chem. Soc. Rev.*, **2016**, *45* (23), 6597-6626.
162. Huang, W.; Ma, B. C.; Lu, H.; Li, R.; Wang, L.; Landfester, K.; Zhang, K. A. I., *ACS Catal.*, **2017**, *7* (8), 5438-5442.
163. Enrico, B.; Tiziana, D. G.; Osvaldo, L.; Andrea, L., *J. Org. Chem.*, **2007**, *72* (25), 9582-9589.
164. Tanielian, C.; Wolff, C.; Esch, M., *J. phys. chem*, **1996**, *100* (16), 6555-6560.
165. Derosa, M. C.; Crutchley, R. J., *Coord. Chem. Rev.*, **2002**, *233* (02), 351-371.
166. Zhang, W.; Li, B.; Ma, H.; Zhang, L.; Guan, Y.; Zhang, Y.; Zhang, X.; Jing, P.; Yue, S., *ACS Appl. Mater. Interfaces*, **2016**, *8* (33), 21465-21471.
167. Ding, X.; Han, B. H., *Angew. Chem. Int. Ed.*, **2015**, *54* (22), 6536-6539.
168. Kumar, R.; Gleissner, E. H.; Tiu, E. G.; Yamakoshi, Y., *Org. Lett.*, **2016**, *18* (2), 184-187.
169. Prier, C. K.; Rankic, D. A.; MacMillan, D. W. C., *Chem. Rev.*, **2013**, *113* (7), 5322-5363.
170. To, W.-P.; Tong, G. S.-M.; Lu, W.; Ma, C.; Liu, J.; Chow, A. L.-F.; Che, C.-M., *Angew. Chem.*, **2012**, *124* (11), 2708-2711.
171. Pibiri, I.; Buscemi, S.; Palumbo Piccionello, A.; Pace, A., *ChemPhotoChem*, **2018**, *2* (7), 535-547.

172. Li, H.; Eddaoudi, M.; O'Keeffe, M.; Yaghi, O. M., *Nature*, **1999**, *402* (6759), 276-279.
173. Li, J. R.; Sculley, J.; Zhou, H.-C., *Chem. Rev.*, **2012**, *112* (2), 869-932.
174. Rosi, N. L.; Juergen, E.; Mohamed, E.; Vodak, D. T.; Jaheon, K.; Michael, O. K.; Yaghi, O. M., *Science*, **2003**, *300* (5622), 1127-1129.
175. Mason, J. A.; Julia, O.; Taylor, M. K.; Hudson, M. R.; Julien, R.; Bachman, J. E.; Gonzalez, M. I.; Antonio, C.; Antonietta, G.; Brown, C. M., *Nature*, **2015**, *527* (7578), 357-361.
176. Huang, Y. B.; Liang, J.; Wang, X. S.; Cao, R., *Chem. Soc. Rev.*, **2017**, *46* (1), 126-157.
177. Wang, H.; Lustig, W. P.; Li, J., *Chem. Soc. Rev.*, **2018**, *47* (13), 4729-4756.
178. Zhang, T.; Lin, W., *Chem. Soc. Rev.*, **2014**, *43* (16), 5982-5993.
179. Yuan, S.; Qin, J. S.; Xu, H. Q.; Su, J.; Rossi, D.; Chen, Y.; Zhang, L.; Lollar, C.; Wang, Q.; Jiang, H. L.; Son, D. H.; Xu, H.; Huang, Z.; Zou, X.; Zhou, H.-C., *ACS Cent. Sci.*, **2018**, *4* (1), 105-111.
180. Chen, D.; Xing, H.; Wang, C.; Su, Z., *J. Mater. Chem. A* **2016**, *4* (7), 2657-2662.
181. Johnson, J. A.; Luo, J.; Zhang, X.; Chen, Y.-S.; Morton, M. D.; Echeverría, E.; Torres, F. E.; Zhang, J., *ACS Catal.*, **2015**, *5* (9), 5283-5291.
182. Liu, H.; Xu, C.; Li, D.; Jiang, H. L., *Angew. Chem. Int. Ed.*, **2018**, *57* (19), 5379-5383.

183. Dhakshinamoorthy, A.; Asiri, A. M.; García, H., *Angew. Chem. Int. Ed.*, **2016**, *55* (18), 5414-5445.
184. Liu, Y.; Howarth, A. J.; Hupp, J. T.; Farha, O. K., *Angew. Chem.*, **2015**, *127* (31), 9129-9133.
185. Park, J.; Jiang, Q.; Feng, D.; Zhou, H.-C., *Angew. Chem.*, **2016**, *128* (25), 7304-7309.
186. Lu, K.; He, C.; Guo, N.; Chan, C.; Ni, K.; Weichselbaum, R. R.; Lin, W., *J. Am. Chem. Soc.*, **2016**, *138* (38), 12502-12510.
187. Lu, K.; He, C.; Lin, W., *J. Am. Chem. Soc.*, **2014**, *136* (48), 16712-16715.
188. Park, J.; Feng, D.; Yuan, S.; Zhou, H.-C., *Angew. Chem.*, **2015**, *127* (2), 440-445.
189. Buru, C. T.; Majewski, M. B.; Howarth, A. J.; Lavroff, R. H.; Kung, C. W.; Peters, A. W.; Goswami, S.; Farha, O. K., *ACS Appl. Mater. Interfaces*, **2018**, *10* (28), 23802-23806.
190. Howarth, A. J.; Majewski, M. B.; Wolf, M. O., *Coord. Chem. Rev.*, **2015**, 282-283, 139-149.
191. George Truscott, T.; Edward, J., *J. Chem. Soc., Faraday Trans.*, **1990**, *86* (18), 3075-3080.
192. Hissler, M.; Harriman, A.; Khatyr, A.; Ziessel, R., *Chem. Eur. J.*, **1999**, *5* (11), 3366-3381.
193. Okamoto, M.; Tanaka, F., *J. Phys. Chem. A*, **2002**, *106* (15), 3982-3990.

194. Liu, Y.; Buru, C. T.; Howarth, A. J.; Mahle, J. J.; Buchanan, J. H.; DeCoste, J. B.; Hupp, J. T.; Farha, O. K., *J. Mater. Chem. A*, **2016**, *4* (36), 13809-13813.
195. Atilgan, A.; Islamoglu, T.; Howarth, A. J.; Hupp, J. T.; Farha, O. K., *ACS Appl. Mater. Interfaces*, **2017**, *9* (29), 24555-24560.
196. Sheldrick, G. M., *Acta Crystallogr. Sect. A: Found. Crystallogr.*, **2008**, *64* (1), 112-122.
197. Hu, J.-y.; Era, M.; Elsegood, M. R. J.; Yamato, T., *Eur. J. Org. Chem.*, **2010**, *2010* (1), 72-79.
198. Wu, Z.-H.; Huang, Z.-T.; Guo, R.-X.; Sun, C.-L.; Chen, L.-C.; Sun, B.; Shi, Z.-F.; Shao, X.; Li, H.; Zhang, H.-L., *Angew. Chem.*, **2017**, *129* (42), 13211-13215.
199. Zhao, J.; Wu, W.; Sun, J.; Guo, S., *Chem. Soc. Rev.*, **2013**, *42* (12), 5323-51.
200. Sun, J.; Zhao, J.; Guo, H.; Wu, W., *Chem. Commun.*, **2012**, *48* (35), 4169-71.
201. Chen, B.; Wang, L.; Gao, S., *ACS Catal.*, **2015**, *5* (10), 5851-5876.
202. Nicolaou, K. C.; Mathison, C. J. N.; Montagnon, T., *Angew. Chem. Int. Ed.*, **2003**, *42* (34), 4077-4082.
203. Jiang, G.; Chen, J.; Huang, J.-S.; Che, C.-M., *Org. Lett.*, **2009**, *11* (20), 4568-4571.
204. Su, F.; Mathew, S. C.; Möhlmann, L.; Antonietti, M.; Wang, X.; Blechert, S., *Angew. Chem.*, **2011**, *123* (3), 683-686.

205. Sun, D.; Ye, L.; Li, Z., *Appl. Catal., B*, **2015**, *164*, 428-432.
206. Xu, C.; Liu, H.; Li, D.; Su, J. H.; Jiang, H. L., *Chem. Sci.*, **2018**, *9* (12), 3152-3158.
207. Raza, F.; Park, J. H.; Lee, H.-R.; Kim, H.-I.; Jeon, S.-J.; Kim, J.-H., *ACS Catal.*, **2016**, *6* (5), 2754-2759.
208. Lang, X.; Ji, H.; Chen, C.; Ma, W.; Zhao, J., *Angew. Chem. Int. Ed. Engl.*, **2011**, *50* (17), 3934-3937.
209. Su, F.; Mathew, S. C.; Mohlmann, L.; Antonietti, M.; Wang, X.; Blechert, S., *Angew. Chem. Int. Ed.*, **2011**, *50* (3), 657-660.
210. Berlicka, A.; Konig, B., *Photochem Photobiol Sci*, **2010**, *9* (10), 1359-1366.
211. Huang, L.; Zhao, J.; Guo, S.; Zhang, C.; Ma, J., *J. Org. Chem.*, **2013**, *78* (11), 5627-5637.
212. Sumida, K.; Rogow, D. L.; Mason, J. A.; McDonald, T. M.; Bloch, E. D.; Herm, Z. R.; Bae, T.-H.; Long, J. R., *Chem. Rev.*, **2011**, *112* (2), 724-781.
213. Li, J.-R.; Sculley, J.; Zhou, H.-C., *Chem. Rev.*, **2011**, *112* (2), 869-932.
214. Yoon, M.; Srirambalaji, R.; Kim, K., *Chem. Rev.*, **2011**, *112* (2), 1196-1231.
215. Lian, X.; Chen, Y.-P.; Liu, T.-F.; Zhou, H.-C., *Chem. Sci.*, **2016**, *7* (12), 6969-6973.
216. Lynch, S. R., *Nutr. Rev.*, **1997**, *55* (4), 102-110.

217. Organization, W. H., *Guidelines for drinking-water quality: recommendations*. World Health Organization: 2004; Vol. 1.
218. Andrews, N. C., *N. Engl. J. Med.*, **1999**, *341* (26), 1986-1995.
219. Séby, F.; Charles, S.; Gagean, M.; Garraud, H.; Donard, O., *J. Anal. At. Spectrom.*, **2003**, *18* (11), 1386-1390.
220. Yuan, D.; Fu, D.; Wang, R.; Yuan, J., *Spectrochim. Acta. Part A*, **2008**, *71* (1), 276-279.
221. Sun, Z.; Liang, P., *Microchim. Acta*, **2008**, *162* (1-2), 121-125.
222. Gao, W.; Liu, F.; Zhang, B.-Y.; Zhang, X.-M.; Liu, J.-P.; Gao, E.-Q.; Gao, Q.-Y., *Dalton Trans.*, **2017**, *46* (40), 13878-13887.
223. Dao, X.; Ni, Y., *Dalton Trans.*, **2017**, *46* (16), 5373-5383.
224. Qian, Z.; Ma, J.; Shan, X.; Feng, H.; Shao, L.; Chen, J., *Chem. Eur. J.*, **2014**, *20* (8), 2254-2263.
225. Lustig, W. P.; Mukherjee, S.; Rudd, N. D.; Desai, A. V.; Li, J.; Ghosh, S. K., *Chem. Soc. Rev.*, **2017**, *46* (11), 3242-3285.
226. Horcajada, P.; Chevreau, H.; Heurtaux, D.; Benyettou, F.; Salles, F.; Devic, T.; Garcia-Marquez, A.; Yu, C.; Lavrard, H.; Dutson, C. L.; Magnier, E.; Maurin, G.; Elkaim, E.; Serre, C., *Chem. Commun.*, **2014**, *50* (52), 6872-6874.

227. Yao, Q.; Bermejo Gómez, A.; Su, J.; Pascanu, V.; Yun, Y.; Zheng, H.; Chen, H.; Liu, L.; Abdelhamid, H. N.; Martín-Matute, B.; Zou, X., *Chem. Mater.*, **2015**, *27* (15), 5332-5339.
228. Feng, D.; Wang, K.; Wei, Z.; Chen, Y.-P.; Simon, C. M.; Arvapally, R. K.; Martin, R. L.; Bosch, M.; Liu, T.-F.; Fordham, S.; Yuan D.; Omary M. A.; Haranczk M.; Smit, B.; Zhou, H.-C., *Nat. Commun.*, **2014**, *5*, 5723-5731.
229. Yang, C. X.; Ren, H. B.; Yan, X. P., *Anal. Chem.*, **2013**, *85* (15), 7441-7446.
230. Wang, B.; Yang, Q.; Guo, C.; Sun, Y.; Xie, L. H.; Li, J. R., *ACS Appl. Mater. Interfaces*, **2017**, *9* (11), 10286-10295.
231. Zhang, Y.; Murphy, C. B.; Jones, W. E., *Macromolecules*, **2002**, *35* (3), 630-636.
232. Luo, X.; Zhang, X.; Duan, Y.; Wang, X.; Zhao, J., *Dalton Trans.*, **2017**, *46* (19), 6303-6311.
233. Mostakim, S.; Biswas, S., *CrystEngComm*, **2016**, *18* (17), 3104-3113.
234. Jin, J. C.; Pang, L. Y.; Yang, G. P.; Hou, L.; Wang, Y. Y., *Dalton Trans.*, **2015**, *44* (39), 17222-17228.
235. Li, H.; He, Y.; Li, Q.; Li, S.; Yi, Z.; Xu, Z.; Wang, Y., *RSC Adv.*, **2017**, *7* (79), 50035-50039.

236. Lv, R.; Chen, Z.; Fu, X.; Yang, B.; Li, H.; Su, J.; Gu, W.; Liu, X., *J. Solid State Chem.*, **2018**, *259*, 67-72.
237. Zhou, Y.; Chen, H.-H.; Yan, B., *J. Mater. Chem. A*, **2014**, *2* (33), 13691-13697.
238. Tan, Q.-H.; Wang, Y.-Q.; Guo, X.-Y.; Liu, H.-T.; Liu, Z.-L., *RSC Adv.*, **2016**, *6* (66), 61725-61731.
239. Li, Y.; Chang, Z.; Huang, F.; Wu, P.; Chu, H.; Wang, J., *Dalton Trans.*, **2018**, *47* (28), 9267-9273.
240. Xu, H.; Dong, Y.; Wu, Y.; Ren, W.; Zhao, T.; Wang, S.; Gao, J., *J. Solid State Chem.*, **2018**, *258*, 441-446.
241. Zhao, X.-L.; Tian, D.; Gao, Q.; Sun, H.-W.; Xu, J.; Bu, X.-H., *Dalton Trans.*, **2016**, *45* (3), 1040-1046.
242. Zhou, X.-H.; Li, L.; Li, H.-H.; Li, A.; Yang, T.; Huang, W., *Dalton Trans.*, **2013**, *42* (34), 12403-12409.
243. Chen, D.-M.; Zhang, N.-N.; Liu, C.-S.; Du, M., *J. Mater. Chem. C*, **2017**, *5* (9), 2311-2317.
244. Shanmugaraju, S.; Mukherjee, P. S., *Chem Commun (Camb)*, **2015**, *51* (89), 16014-16032.
245. Shirota, Y.; Kageyama, H., *Chem. Rev.*, **2007**, *107* (4), 953-1010.

246. v. Büнау, G., *Berichte der Bunsengesellschaft für physikalische Chemie*, **1970**, 74 (12), 1294-1295.
247. Monteserín, M.; Burrows, H. D.; Valente, A. J. M.; Pais, A. A. C. C.; Di Paolo, R. E.; Maçanita, A. L.; Tapia, M. J., *Langmuir*, **2017**, 33 (46), 13350-13363.
248. Nguyen, B. T.; Gautrot, J. E.; Ji, C.; Brunner, P.-L.; Nguyen, M. T.; Zhu, X. X., *Langmuir*, **2006**, 22 (10), 4799-4803.
249. Hecht, S.; Fréchet, J. M. J., *Angew. Chem. Int. Ed.*, **2001**, 40 (1), 74-91.
250. Mei, J.; Leung, N. L. C.; Kwok, R. T. K.; Lam, J. W. Y.; Tang, B. Z., *Chem. Rev.*, **2015**, 115 (21), 11718-11940.
251. Mei, J.; Hong, Y.; Lam, J. W. Y.; Qin, A.; Tang, Y.; Tang, B. Z., *Adv. Mater.*, **2014**, 26 (31), 5429-5479.
252. Hong, Y.; Lam, J. W.; Tang, B. Z., *Chem. Soc. Rev.*, **2011**, 40 (11), 5361-5388.
253. Zhang, X.; Lu, X.; Zhen, Y.; Liu, J.; Dong, H.; Zhao, G.; He, P.; Wang, Z.; Jiang, L.; Hu, W., *J. Mater. Chem. C*, **2014**, 2 (26), 5083-5086.
254. Sasaki, S.; Suzuki, S.; Igawa, K.; Morokuma, K.; Konishi, G.-i., *J. Org. Chem.*, **2017**, 82 (13), 6865-6873.

255. Li, J.; Yang, W.; Zhou, W.; Li, C.; Cheng, Z.; Li, M.; Xie, L.; Li, Y., *RSC Adv.*, **2016**, *6* (42), 35833-35841.
256. Kitagawa, S., *Chem. Soc. Rev.*, **2014**, *43* (16), 5415-5418.
257. Zhou, H.-C.; Long, J. R.; Yaghi, O. M., *Chem. Rev.*, **2012**, *112* (2), 673-674.
258. Hu, Z.; Deibert, B. J.; Li, J., *Chem. Soc. Rev.*, **2014**, *43* (16), 5815-5840.
259. Ma, L.; Feng, X.; Wang, S.; Wang, B., *Mater. Chem. Front.*, **2017**, *1* (12), 2474-2486.
260. Gui, B.; Yu, N.; Meng, Y.; Hu, F.; Wang, C., *J. Polym. Sci., Part A: Polym. Chem.*, **2017**, *55* (11), 1809-1817.
261. Shustova, N. B.; McCarthy, B. D.; Dinca, M., *J. Am. Chem. Soc.*, **2011**, *133* (50), 20126-20129.
262. Zhang, Q.; Su, J.; Feng, D.; Wei, Z.; Zou, X.; Zhou, H. C., *J. Am. Chem. Soc.*, **2015**, *137* (32), 10064-10067.
263. Wei, Z.; Gu, Z. Y.; Arvapally, R. K.; Chen, Y. P.; McDougald, R. N., Jr.; Ivy, J. F.; Yakovenko, A. A.; Feng, D.; Omary, M. A.; Zhou, H. C., *J. Am. Chem. Soc.*, **2014**, *136* (23), 8269-8276.
264. Hu, Z.; Huang, G.; Lustig, W. P.; Wang, F.; Wang, H.; Teat, S. J.; Banerjee, D.; Zhang, D.; Li, J., *Chem. Commun.*, **2015**, *51* (15), 3045-3048.

265. Tao, C. L.; Chen, B.; Liu, X. G.; Zhou, L. J.; Zhu, X. L.; Cao, J.; Gu, Z. G.; Zhao, Z.; Shen, L.; Tang, B. Z., *Chem. Commun.*, **2017**, 53 (72), 9975-9978.
266. Di Donato, E.; Vanzo, D.; Semeraro, M.; Credi, A.; Negri, F., *J. Phys. Chem. A*, **2009**, 113 (23), 6504-6510.
267. Pal, S. K.; Setia, S.; Avinash, B. S.; Kumar, S., *Liq. Cryst.*, **2013**, 40 (12), 1769-1816.
268. Bhalla, V.; Arora, H.; Singh, H.; Kumar, M., *Dalton Trans.*, **2013**, 42 (4), 969-974.
269. Arora, H.; Bhalla, V.; Kumar, M., *RSC Adv.*, **2015**, 5 (41), 32637-32642.
270. Arora, H.; Pramanik, S.; Kumar, M.; Bhalla, V., *New J. Chem.*, **2016**, 40 (4), 3187-3193.
271. Chen, L.; Xu, S.; McBranch, D.; Whitten, D., *J. Am. Chem. Soc.*, **2000**, 122 (38), 9302-9303.
272. Zhang, Y. Z.; He, T.; Kong, X. J.; Lv, X. L.; Wu, X. Q.; Li, J. R., *ACS Appl. Mater. Interfaces*, **2018**, 10 (33), 27868-27874.
273. Grabowski, Z. R.; Rotkiewicz, K.; Rettig, W., *Chem. Rev.*, **2003**, 103 (10), 3899-4032.
274. Slama-Schwok, A.; Blanchard-Desce, M.; Lehn, J. M., *J. Phys. Chem.*, **1990**, 94 (10), 3894-3902.
275. Zhang, M.; Feng, G.; Song, Z.; Zhou, Y. P.; Chao, H. Y.; Yuan, D.; Tan, T. T.; Guo, Z.; Hu, Z.; Tang, B. Z.; Liu, B.; Zhao, D., *J. Am. Chem. Soc.*, **2014**, 136 (20), 7241-7244.

276. Deng, Y.; Chen, N.; Li, Q.; Wu, X.; Huang, X.; Lin, Z.; Zhao, Y., *Cryst. Growth Des.*, **2017**, *17* (6), 3170-3177.
277. Wu, Z. H.; Huang, Z. T.; Guo, R. X.; Sun, C. L.; Chen, L. C.; Sun, B.; Shi, Z. F.; Shao, X.; Li, H.; Zhang, H. L., *Angew. Chem. Int. Ed.*, **2017**, *56* (42), 13031-13035.
278. Nagarkar, S. S.; Desai, A. V.; Ghosh, S. K., *Chem. Commun.*, **2014**, *50* (64), 8915-8918.
279. Nagarkar, S. S.; Joarder, B.; Chaudhari, A. K.; Mukherjee, S.; Ghosh, S. K., *Angew. Chem. Int. Ed.*, **2013**, *52* (10), 2881-2885.
280. Wang, B.; Lv, X.-L.; Feng, D.; Xie, L.-H.; Zhang, J.; Li, M.; Xie, Y.; Li, J.-R.; Zhou, H.-C., *J. Am. Chem. Soc.*, **2016**, *138* (19), 6204-6216.
281. Pramanik, S.; Zheng, C.; Zhang, X.; Emge, T. J.; Li, J., *J. Am. Chem. Soc.*, **2011**, *133* (12), 4153-4155.
282. Yang, N.-N.; Sun, W.; Xi, F.-G.; Sui, Q.; Chen, L.-J.; Gao, E.-Q., *Chem. Commun.*, **2017**, *53* (10), 1747-1750.
283. Gutierrez, M.; Navarro, R.; Sanchez, F.; Douhal, A., *Phys. Chem. Chem. Phys.*, **2017**, *19* (25), 16337-16347.